nature aging

Article

https://doi.org/10.1038/s43587-026-01108-z

Reduced ULK1 links impaired autophagy and mitophagy to Alzheimer's disease pathology

Received: 7 March 2024

Accepted: 11 March 2026

Published online: 14 May 2026

Check for updates

Jun-Ping Pan[1,2,3,33], Ping-Jie Wang[1,4,33], Jianying Zhang[3,5,33], Anne-Brita Knapskog[6,33], Leiv Otto Watne[6,7,8,33], He-Ling Wang[3], Maria Jose Lagartos-Donate[3], Sofie Lautrup[3], Li-Peng Mao[1,9], Qian Wang[4,10], Zhi-Peng Ling[1], Shi-qi Zhang[3], Tomás Schmauck-Medina[3], Ruixue Ai[3], Trine Holt Edwin[6], Tianjiao Zhang[11], Ingvild Saltvedt[12,13], Rannveig Sakshaug Eldholm[12,13], Annabel Smith[14], Kateřina Veverová[15], Domenica Caponio[3], Asgeir Kobro-Flatmoen[16], Huanhuan Pang[17], Zijian Wang[1], Haoyun Wang[1], Li-juan Gao[1], Nathalie Bodd Halaas[6,18], Garry Wong[11], Martin Vyhnalek[15], Oscar Junhong Luo[9], William A. McEwan[14], Jon Storm-Mathisen[19,20], Li Gan[21], Zeping Hu[17], Henrik Zetterberg[22,23,24,25,26,27], Menno P. Witter[16], Dag Aarsland[28,29], Geir Selbæk[6,30,31], Guobing Chen[1,2,32] ✉ & Evandro Fei Fang[1,3,4,10,20] ✉

ULK1 (Atg1) initiates macroautophagy and mitophagy, which support neuronal growth and survival, yet how this pathway is disrupted in aging and Alzheimer's disease (AD) remains unclear. Here we report reduced ULK1 in serum and cerebrospinal fluid during aging in cognitively unimpaired participants from the COGNORM study ($n = 75$) and in patients with AD from the NorCog Memory Clinic Cohort ($n = 316$). In AD mice, ULK1 overexpression stimulates autophagic flux, reduces AD pathology and delays cognitive decline alongside increased phagocytic degradation of amyloid-β, reduced tauopathy and improved mitochondrial quality. Mechanistically, ULK1 upregulation increases autophagy and PINK1-, FUNDC1- and AMBRA1-associated mitophagy; higher autophagy and mitophagy increase cellular NAD^+, which in turn deacetylates acetylated-Tau174 via the NAD^+–SIRT1 axis, leading to reduced tauopathy. Using in vitro tau seeding assays and a *Caenorhabditis elegans* tau model, we validate the efficacy of ULK1 activators in inhibiting tauopathy. We propose that age-related decline in ULK1 leads to autophagy and mitophagy impairment and increases the progression of AD and identify ULK1 as a potential therapeutic target.

Alzheimer's disease (AD) is a slowly progressing neurodegenerative disease that ultimately causes severe cognitive dysfunction and loss of physical independence[1–5]. Prior to onset of clinical disease, patients with AD typically undergo a long asymptomatic phase during which amyloid-β (Aβ) peptides and hyperphosphorylated tau (p-tau)-containing neurofibrillary tangles accumulate in neurons, and Aβ plaques deposit in the brain parenchyma[2,6,7]. It is postulated that accumulated damage in the aging and AD brain is caused by increased production and defective clearance of certain proteins, the latter caused by compromised homeostatic pathways such as the ubiquitin–proteasome system, the unfolded protein response and glymphatic systems and especially autophagy[8–10]. Autophagy is a highly conserved catabolic process that maintains cellular homeostasis through systematic sequestration and lysosomal degradation of defective or redundant intracellular components, including damaged proteins and organelles (such as dysfunctional mitochondria),

A full list of affiliations appears at the end of the paper. ✉e-mail: guobingchen@jnu.edu.cn; e.f.fang@medisin.uio.no

thereby promoting cellular homeostasis, survival and development[8]. Because autophagy can refer to distinct pathways, we here focus on macroautophagy (hereafter, autophagy). Mounting evidence indicates a role for defective autophagy during the aging process and in AD[8,9], but the underlying molecular mechanisms describing how and why autophagy is defective during aging, and especially in AD, are not fully understood. Most critically, there is a lack of experimental data from large human populations. A subtype of autophagy, mitophagy is a process that specifically recognizes and degrades damaged mitochondria, which is essential for neural differentiation, growth, function and resilience[11,12]. Mitochondrial dysfunction is a hallmark of aging and neurodegenerative diseases and contributes to impaired proteostasis, protein aggregation, energy dysregulation, inflammation and neuronal death[13,14]. Thus, compromised mitophagy, leading to accumulation of damaged mitochondria, is an apparent risk factor for AD[11,15].

The links between AD pathologies and compromised autophagy and mitophagy are intertwined. In mouse models harboring familial AD mutations, autophagy (including mitophagy) is inhibited, likely due to reduced expression of autophagic proteins and faulty autolysosome acidification[11,16], which compromises autophagy, leading to the buildup of intraneuronal Aβ and extracellular Aβ plaques[16]. Furthermore, in tau models, several types of autophagic pathways are impaired, including impaired mitophagy[11,17] and chaperon-mediated autophagy[18], and restoring autophagy reduces p-tau/aggregated tau and improves memory[11,18]. Aβ and p-tau further damage mitochondrial dynamics and adenosine triphosphate (ATP) production, which can further increase accumulation of Aβ and p-tau, forming a vicious circle[15,19]. Mitophagy may be especially protective: its failure can trigger cGAS-STING inflammation via mitochondrial DNA release and impair energy-demanding glial Aβ phagocytosis[11,20–22]. Similarly, autophagy and mitophagy restoration counteracts both Aβ and tau pathologies in animal and induced pluripotent stem-cell models of AD[11,18,23,24].

Mechanistic knowledge around why aberrant autophagy occurs in AD, especially in an aging perspective and in the human population, is sparse. Studies suggest that aberrant expression (or variants due to single-nucleotide polymorphisms) of autophagy proteins, such as PS1[25], Beclin1[24], BCL2-associated athanogene 3[26] and ATG16L[27], contributes to AD. However, associated roles for the key autophagy protein ULK1 in patients with AD were not clear. ULK1 is a key protein in autophagy initiation as it forms the ULK1 complex (with FIP200, ATG13 and ATG101) to transport upstream signals from AMP-activated protein kinase (AMPK) and mTOR to initiate autophagy; the ULK1 complex acts as a node to stimulate cell signaling pathways, including activation of the class III phosphatidylinositol 3-kinase complex (containing the neuroprotective Beclin1) and recruitment of downstream Atg proteins in building the autophagosome[28]. Unlike many other autophagy machinery proteins, ULK1 also positively regulates mitophagy: for example, (1) within the classical PINK1-Parkin-dependent mitophagy pathway, ULK1 is recruited as a downstream protein for mitophagic elimination of damaged mitochondria[29]; (2) ULK1 recruits Parkin to depolarized mitochondria and enhances the interaction between Ambra1 and Beclin1[30]; and (3) ULK1 phosphorylates FUNDC1, enhancing FUNDC1 binding to LC3 to lead mitophagy[31]. Although we recently reported reduced ULK1 in post-mortem hippocampi from a small number of patients with AD[11], how ULK1 changes during the progression of AD and in aging was not known; a spatiotemporal change of ULK1 in the AD brain was not explored. Additionally, whether ULK1 reduction is a culprit or a bystander in AD was not known. Here, by using human samples (cerebrospinal fluid (CSF), blood and post-mortem brain tissue) and a series of laboratory models, we show reduced ULK1 during aging, particularly in AD. ULK1 reduction likely correlates with progression of AD and shows itself to be a druggable target for AD as genetic and pharmacological upregulation of ULK1-associated autophagy and mitophagy abrogates AD pathologies and memory loss in different AD animal models.

Results

ULK1 decreases with age and is lower in patients with AD

As ULK1 is a key protein involved in autophagy and mitophagy, we asked how the levels of ULK1 protein change during aging and in AD. We addressed these questions by using serum and CSF samples from a clinically well-characterized cohort containing 391 individuals (316 AD; 75 cognitively unimpaired (CU)). Of the 316 patients, 56 had mild cognitive impairment (AD-MCI), and the remaining 260 were AD-dementia patients. Among the 75 CU controls, 22 individuals had 4-year follow-up data. Although the average age of the CU group was slightly higher than that of the AD-dementia, there was no age difference between CU and AD-MCI; further, there were differences in other parameters such as sex, education (years), *APOE*ε4 positivity (%) and Mini Mental State Examination (MMSE) scores: although MMSE separated all three groups, shorter education and *APOE*ε4 genotype were more prevalent in the AD group (Table 1, top). Among AD-dementia, AD-MCI and CU, there were statistical differences in standard CSF biomarkers, including $A\beta_{1\text{-}42}$ (A), total tau (N) and p-tau_{181} (T), with the AD-dementia group showing the lowest $A\beta_{1\text{-}42}$ but highest total tau and p-tau_{181} (Table 1, lower panel). Our data for patient characteristics and CSF AD biomarkers are in line with data from published large population cohorts[32,33], highlighting the representativeness of our cohort.

To investigate whether age impacts ULK1 levels, we examined changes in ULK1 over 4 years in serum and CSF samples from the CU group. Compared to baseline, ULK1 levels were 41.35% lower in serum and 19.18% lower in CSF at 4-year follow-up within the CU group (Fig. 1a,b). In line with reduced ULK1 in serum and CSF during aging, there was a trend of total hippocampal ULK1 reduction during aging (Fig. 1c and Extended Data Fig. 1a). We then looked at changes in hippocampal neurons more specifically and quantified neuronal ULK1 using two methods: (1) including $ULK1^+$ neurons/total neurons and (2) relative ULK1 signal intensity per neuron; indeed, both these parameters were lower in old CU compared to middle-aged CU individuals (Fig. 1d–f). Pathological and medical information of the brain tissue donors are presented in Supplementary Table 1.

We then investigated changes of ULK1 in AD-MCI and AD-dementia. In serum samples, there was a disease-phase-dependent reduction of ULK1 (Fig. 1g). For CSF ULK1, although there was no statistical difference between AD-MCI and CU or AD-MCI and AD-dementia, there was a reduction from CU to AD-dementia (Fig. 1h). The Spearman's correlation coefficient between CSF ULK1 and serum ULK1 was significant, although weak, in the AD group, whereas there was no significant correlation in the CU control group. We then performed correlation analyses between serum and CSF ULK1 and AD core biomarkers: there was no correlation between serum and CSF ULK1 levels and $A\beta_{1\text{-}42}$, but CSF ULK1 was strongly correlated with both p-tau_{181} and total tau (Supplementary Table 2). First, in the CSF samples, there were higher ULK1 levels in the CU group with pathological levels of p-tau_{181} (T+) compared to the T+ patient (AD-MCI + AD-dementia) group; this difference was even more dramatic in serum samples between T+ CU group and T+ patient group (Supplementary Table 3). Second, in CSF samples from the CU control group, individuals with high T+ showed high ULK1 levels, correlating potentially higher autophagy, high tauopathy and maintenance of cognition (Supplementary Table 4). More detailed information showing multiple linear regression analyses between CSF ULK1 and different parameters for the patient group and CU controls, respectively, are presented in Supplementary Tables 5 and 6. These data suggest that ULK1 reduces with age in serum and CSF from CU individuals and is further reduced from CU to AD. Note that the average age of the CU group was slightly higher than the AD-dementia group, so further validations of age-dependent reduction of ULK1 are needed using strict age-matching and large clinical trials.

As ULK1 was reduced in serum and CSF samples of patients with AD and was correlated to tauopathy in these samples, we asked how

https://doi.org/10.1038/s43587-026-01108-z

Table 1 | Demographics and characteristics of CU controls and patients with AD

Variables	AD-MCI (*n*=56)	AD-dementia (*n*=260)	CU		*P* values	
			P values	(*n*=75)	CU versus AD	CU versus MCI
Patient characteristics						
Age, years (s.d.)	70.7 (5.9)	70.2 (6.4)	0.54[c]	72.2 (6.4)	0.02[c]	0.18[c]
Female, *n* (%)	29 (51.8)	153 (58.8)	0.33[d]	29 (38.7)	0.002[d]	0.14[d]
Education, years (s.d.)	13.6 (3.6)	12.1 (3.7)	0.009[c]	14.2 (3.5)	<0.001[c]	0.37[c]
*APOE*ε4 positive[a], *n* (%)	42 (77.8)	167 (73.2)	0.49[d]	29 (39.7)	<0.001[d]	<0.001[d]
MMSE, score (s.d.)	27.1 (2.9)	22.5(4.2)	<0.001[c]	29.2 (0.9)	<0.001[c]	<0.001[c]
AD core biomarkers						
$A\beta_{1\text{-}42}$, pg ml^{-1} (s.d.)	634.9 (209.4)	571.1 (173.4)	0.02[c]	711.9 (228.0)	[b]	[b]
Total tau, pg ml^{-1} (s.d.)	575.2 (294.7)	724.2 (384.0)	0.007[c]	376.7 (151.4)	[b]	[b]
p-tau_{181}, pg ml^{-1} (s.d.)	80.5 (37.4)	94.6 (43.5)	0.02[c]	60.4 (19.9)	[b]	[b]

n=391. *P*<0.05 was considered statistically significant. *APOE*, apolipoprotein E. [a]Missing genotype data in 36 participants. [b]Comparison not possible due to interlaboratory variability. The AD core CSF biomarkers were analyzed at Akershus University Hospital (Ahus), and the CSF AD core biomarkers were analyzed at Sahlgrenska University Hospital (Mölndal, Sweden), although the same kits and protocols were used. [c]*t*-test applied. [d]Chi-squared test applied.

ULK1 changed in the human AD brain. We thus checked *ULK1*mRNA levels in a public single-nucleus transcriptomic database[34] and protein levels in post-mortem human brain samples. In microglia, ULK1 was likely increased from Braak stages 0–2 and 3–4 but was reduced in Braak stages 5–6 (though no statistical difference); there were trends toward ULK1 reduction in oligodendrocyte progenitor cells, inhibitory neurons and oligodendrocytes between Braak stages 0–2 and either of the two advanced stages. However, ULK1 was significantly reduced in excitatory neurons and astrocytes in Braak stages 5–6 compared to Braak stages 0–2 (Fig. 1i). Similarly, genes encoding other components of the ULK1 complex, including *ATG101*, *FIP200* and *ATG13*, also showed significant downregulation in excitatory neurons with the progression of tauopathy (Extended Data Fig. 1b–d), further supporting our hypothesis of compromised ULK1 signaling pathway in AD. We then checked ULK1 protein levels in neurons from various sites in the CU control and patients' with AD brains. We aimed to capture any spatiotemporal change of ULK1 in the AD brain and thus selected three key brain regions in view of know spatiotemporal patterns of deposition of neurofibrillary tangles (entorhinal cortex (EC), hippocampus (HIP) and prefrontal cortex (PFC))[15] covering control and Braak staging 5–6. We costained for ULK1 and a neuronal marker MAP2. In the HIP, there was a 10.57% reduction in $ULK1^+$ neurons/total neurons as well as 15.44% decrease in ULK1 expression level per neuron from old control to AD (Fig. 1j,k and Extended Data Fig. 1e). We found a similar pattern of reduced neuronal ULK1 in the EC of AD brains when compared to CU individuals (Extended Data Fig. 1f–h). In the PFC, although there was no difference in $ULK1^+$ neurons/total neurons, the expression levels of ULK1 in each neuron were lower in AD versus CU (Extended Data Fig. 1i–k). Regarding the spatial relationship between ULK1 and Aβ or tauopathy, our immunofluorescence (IF) data in AD hippocampi showed colocalizations of ULK1 and Aβ or ULK1 and ac-tau_{174} (Extended Data Fig. 1l,m). In summary, these data suggest cell-type-specific and spatiotemporal-specific changes (in many cases, a reduction) of ULK1, at mRNA and protein levels, with increasing AD tauopathy.

Given reduced ULK1 in biofluids and brain tissue, we wondered whether ULK1 plays a protective role against AD progression. We thus used the Clinical Dementia Rating Sum of Boxes (CDR-SB), which we have used previously[35], to assess AD progression over the years in individuals with low, medium and high ULK1 levels. A significant interaction existed between time and CSF ULK1, where higher baseline CSF ULK1 was associated with slower progression to AD (lower CDR-SB score) over time after adjusting for age, education, sex, disease type (MCI or dementia) and baseline level of CSF $A\beta_{1\text{-}42}$ and CSF p-tau_{181} (Fig. 1l). This human data motivated subsequent animal studies to test whether ULK1 is protective in AD.

ULK1 overexpression is neuroprotective in mice

To test this hypothesis, we used a chicken beta-actin promoter (CAG) promoter and generated a ubiquitously ULK1-overexpressing mouse model (named $Ulk1^{OV}$, detailed in Extended Data Fig. 2a,b and Methods). We used a ubiquitous model because ULK1 functions in different cell types and we first wanted to understand any additive/synergistic effect of ULK1 overexpression in different cells in brain health; targeted and in vitro models were used later. We checked the expression of ULK1 in multiple brain cells, different brain regions and other main tissues commonly studied in aging (liver, lung, heart, muscle and kidney) (Extended Data Fig. 2). ULK1 was overexpressed in all the tested types of cells and in different organs/tissues compared to wild type (WT) (Extended Data Fig. 2c–i). Notably, in young $Ulk1^{OV}$ mice under ad libitum condition, the basial level of autophagy seemed to not increase (LC3BII) compared to WT mice. To further investigate how ULK1 was overexpressed in various brain cell types, we established cell cultures of primary neurons, astrocytes and microglia that were isolated from embryonic day-16 WT and $ULK1^{OV}$ mice (Extended Data Fig. 2c–f). IF of cells on culture day 7 using antibodies against the neuronal marker beta III tubulin (Tuj1), the astrocyte marker glial fibrillary acidic protein (GFAP) and the microglia marker ionized calcium-binding adapter molecule 1 (IBA1), indicated a high purity for each of the cell types we isolated (Extended Data Fig. 2c–h), facilitating the following phenotypic and mechanistic studies.

We then asked whether ULK1 overexpression could increase neuronal resilience using primary cortical neurons exposed to excitatory and metabolic challenges (as established elsewhere[36]) and oligomeric $A\beta_{1\text{-}42}$ ($oA\beta_{1\text{-}42}$) (Fig. 2 and Extended Data Fig. 2j,k). Primary cortical neurons from both WT and $Ulk1^{OV}$ mice were treated with kainic acid (KA) and N-methyl-D-aspartate (NMDA), as well as two mitochondrial toxicants—3-nitropropionic acid (3-NPA) and rotenone—at various concentrations for 24 h. In WT neurons, all toxicants caused a dose-dependent increase of neuronal apoptotic death, accompanied by neurite fragmentation and loss; $Ulk1^{OV}$ neurons were more resistant to toxicant-induced cell death (Fig. 2a–e and Extended Data Fig. 2k). This neuronal resilience against toxicants was further consolidated by terminal deoxynucleotidyl transferase-mediated dUTP nick-end labeling (TUNEL) assay-based apoptotic cell data showing a lower TUNEL-positive cell population in the $Ulk1^{OV}$ group compared to WT (Fig. 2f,g). As ULK1 inhibited neuronal toxicity from AD-specific $oA\beta_{1\text{-}42}$ (Fig. 2e), we explored this phenomenon further by focusing on effects on neuronal morphology

https://doi.org/10.1038/s43587-026-01108-z

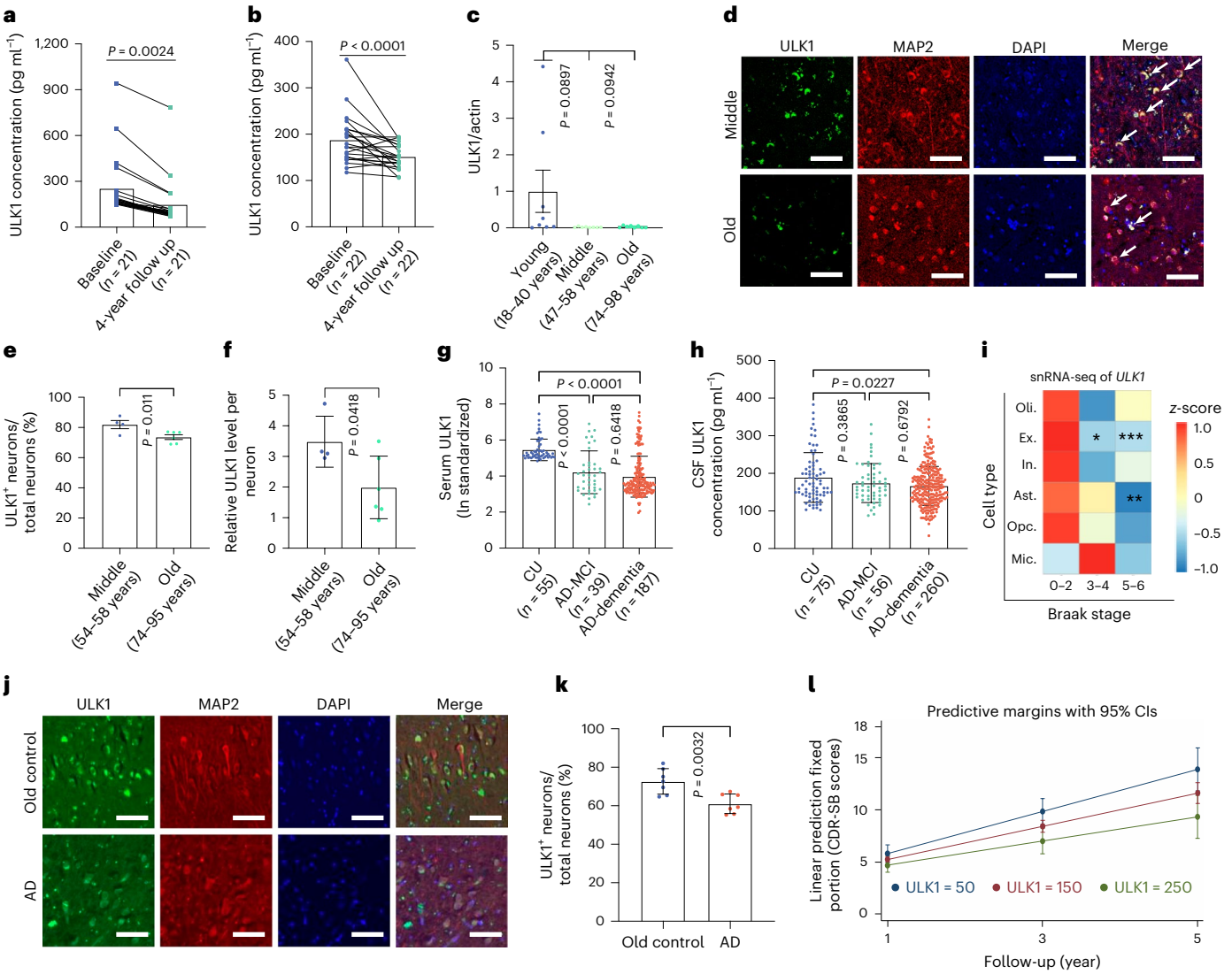

Fig. 1 | ULK1 decreases with age and in AD. a, Serum ULK1 (pg ml^{-1}) was quantified in CU study participants at baseline ($n = 21$) and 4 years later ($n = 21$). n = number of study participants per experimental group. **b**, CSF ULK1 (pg ml^{-1}) was quantified in CU controls at baseline ($n = 22$) and 4 years later ($n = 22$). **c**, Changes of hippocampal ULK1 in different age groups. Post-mortem hippocampal samples from young, middle-aged and old people ($n = 8$ per group). Original WB data are provided in Extended Data Fig. 1a. **d**, Tissue sections (7 µm) were prepared from HIP of human post-mortem brain tissues from middle-aged and old groups. Slides were stained for ULK1 (green), MAP2 (red) and DAPI (blue). Scale bars, 20 µm. **e**,**f**, Quantification of immunofluorescent signals in tissues (**d**) in two ways, including with the data presented as ULK1-positive (ULK1^{+}) neurons/total neurons (**e**) or signal intensity per neuron (**f**) ($n = 4$ and 6). **g**, Bar chart comparing serum ULK1 (ln transformed pg ml^{-1}) in CU, AD-MCI and AD-dementia patients. Data points were subjected to ln transformation to correct for skewed data distribution. n = number of participants per group. (Age, years ± s.d., min–max: CU, 71.8 ± 6.4, 64–89 years; AD-MCI, 70.6 ± 5.4, 52–81 years; AD-dementia, 69.7 ± 6.7, 49–84 years.) **h**, Box plots showing changes of CSF ULK1 in designated groups. (Age, years ± s.d., min–max: CU, 72.2 ± 6.4, 64–89 years; AD-MCI, 70.7 ± 5.9, 49–81 years; AD-dementia, 70.2 ± 6.4, 49–84 years.) **i**, Heat map for relative abundance of *ULK1* small nuclear RNA (snRNA) stratified by Braak stages (0–2, 3–4, 5–6) and brain cell types. Data represent single-nucleus RNA samples prepared from post-mortem human brain. **j**,**k**, Changes of neuronal ULK1 expression between old control and AD hippocampal tissues. ULK1 (green), MAP2 (red) and DAPI (blue). A representative set of images (**j**) and quantified data in the form of ULK1-positive (ULK1^{+}) neurons/total neurons (**k**) ($n = 6$ and 7). Scale bars, 20 µm (**j**). **l**, CDR-SB data showing that higher ULK1 correlates with slower AD progression. CSF ULK1 was measured at baseline and the patient cohort stratified into subgroups with low (50 pg ml^{-1}), medium (150 pg ml^{-1}) or high (250 pg ml^{-1}) expression of ULK1. CDR-SB protocol was administered at 1-, 3- or 5-year follow-up assessment. The graph shows linear regression for CDR-SB score versus time. Unless specified elsewhere, data are mean ± s.e.m. Statistical analyses used were as follows: paired t-test (**a**,**b**), two-sided unpaired two-tailed Student's t-test (**e**,**f**,**k**). One-way ANOVA followed by Dunnett's multiple comparisons test (**c**) and by Tukey's multiple comparisons test (**g**,**h**) and Wilcoxon test (**i**). Oli., oligodendrocytes; Ex., excitatory neurons; In., inhibitory neurons; Ast., astrocytes; Opc., oligodendrocyte progenitor cells; Mic., microglia; CI, confidence interval. *$P < 0.05$, **$P < 0.01$, ***$P < 0.001$.

and $A\beta_{1\text{-}42}$-induced tauopathy. Subcellular accumulation of tau in the somatodendritic domain forming p-tau aggregates is a typical pathological feature of AD and can be induced by oligomer $A\beta_{1\text{-}42}$ (ref. 37). To investigate whether ULK1 can reduce the somatodendritic accumulation of tau induced by $A\beta_{1\text{-}42}$ in vitro, we treated both WT and $Ulk1^{OV}$ neurons from DIV16 for 6 days. Morphologically, ULK1 overexpression counteracted $A\beta_{1\text{-}42}$-induced axon shortening from 258.50 ± 30.11 µm to 397.5 ± 33.71 µm (Fig. 2h–j). Moreover, ULK1-overexpressing neurons exhibited 24% fewer $A\beta_{1\text{-}42}$-induced tau aggregates in the somatodendritic domain than the WT group (Fig. 2h,k). These data suggest that ULK1 protects mouse primary neurons against excitotoxic and metabolic stress and ameliorates $A\beta_{1\text{-}42}$ and tauopathy.

https://doi.org/10.1038/s43587-026-01108-z

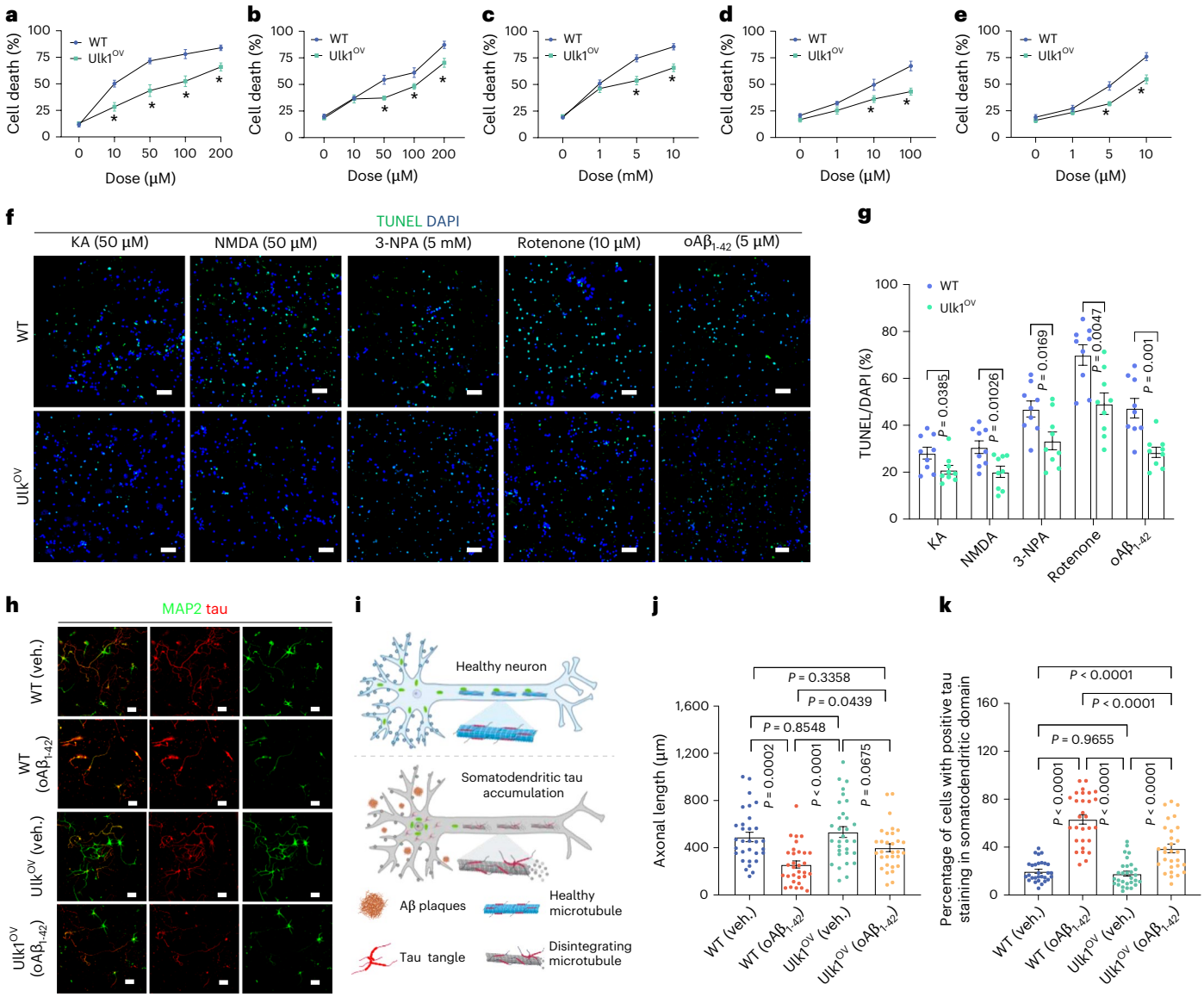

Fig. 2 | ULK1 overexpression increases neuronal resilience against excitatory metabolic stresses as well as inhibits Aβ and tau pathologies. a–**e**, Primary cortical neurons from WT and Ulk1^{OV} mice were exposed to neurotoxicants for 24 h at the indicated doses, and percent neuronal death by apoptosis was quantified using a Hoechst dye: KA (**a**), NMDA (**b**), 3-NPA (**c**), rotenone (**d**), oAβ$_{1-42}$ (**e**). $n = 3$ biological sets. **f**,**g**, Representative images (TUNEL signal after 24 h exposure) (**f**) and quantified data (from three biological sets) (**g**). ULK1-overexpressed neurons were more resilient than WT neurons against apoptotic cell death induced by different neurotoxicants. **h**,**i**, Representative images (**h**) and a schematic diagram showing the adverse effects of Aβ and tau tangles on neuronal health (**i**). ULK1 overexpression reduced oAβ$_{1-42}$-induced tau pathology in primary neurons. DIV 5 neurons were treated with oAβ$_{1-42}$ (5 μM) or vehicle (0.5% dimethyl sulfoxide) for 5 days and then stained with antibodies to tau (red) or MAP2 (somatodendritic compartment, green). **j**,**k**, Axonal length (**j**) and percent tau in the somatodendritic domain (**k**) in the indicated experimental groups. ULK1 overexpression reduced oAβ$_{1-42}$-induced neuronal toxicity. One dot denotes data from one neuron ($n = 9$ technical repeats from a total of 3 biological replicates). Unless specified elsewhere, data are mean ± s.e.m. Statistical analyses were performed as follows: two-way ANOVA followed by Dunnett's multiple comparisons test (**a**–**e**,**g**); two-way ANOVA followed by Tukey's multiple comparisons test (**j**,**k**). Scale bars, 50 μm (**h**). Veh., vehicle. *$P < 0.05$.

ULK1 overexpression improves learning and memory but does not change body composition or basal metabolism in 7-month-old 5xFAD mice

Because ULK1 overexpression improved neuronal resilience, we aimed to determine whether it ameliorated symptoms in AD mice. We crossed Ulk1^{OV} mice with the 5xFAD mice and generated 5xFAD;Ulk1^{OV} mice (Fig. 3a). Seven-month-old mice of both sexes from WT, 5xFAD, Ulk1^{OV}, 5xFAD;Ulk1^{OV} were then subjected to a series of memory tests, including novel object location (NOL), novel object recognition (NOR) and Y-maze. In the NOL discrimination index, 5xFAD mice scored lower than WT mice, but this was reversed in 5xFAD;Ulk1^{OV} mice (Fig. 3b); similar results were shown when the data were presented for exploration frequency (Extended Data Fig. 3a–e,k). A similar effect on ULK1-based memory improvement was evident for the NOR (Fig. 3c and Extended Data Fig. 3f–j,l) and Y-maze mice (Fig. 3d and Extended Data Fig. 3m). We further asked whether ULK1 was able to improve the cognitive performance of the 5xFAD mice in the standard Morris water maze (MWM). Relative to WT mice, 5xFAD animals exhibited a significant latency from day 3 to 7, and this was normalized by ULK1 overexpression (Fig. 3e and Extended Data Fig. 3p,q). During the probe trial on day 8, 5xFAD;Ulk1^{OV} mice spent more time exploring the target quadrant than 5xFAD mice, presumably reflecting better memory (Fig. 3f,g); there was a trend toward the same pattern observed for exploration frequency (Fig. 3h), without changes in swim speed

(Extended Data Fig. 3r–t). As there is a gender difference in the risk of developing AD[38], we asked whether ULK1 worked equally well in female and male AD mice. Due to the variations in the data, some of the aforementioned NOR/NOL/Y-maze data did not reach statistical significance (Extended Data Fig. 3). However, ULK1 overexpression increased memory in male mice in NOR (Extended Data Fig. 3g) and improved female (not male) AD mice's performance in Y-maze (Extended Data Fig. 3n,o). Additionally, ULK1 overexpression improved MWM-based spatial memory in female and male AD mice (Extended Data Fig. 3u,v). Together, these data suggest that ULK1 supports cognitive function in male and female mice.

We then asked whether ULK1 overexpression in AD mice could improve motor function, body composition and basal metabolism. ULK1 overexpression in AD mice did not alter motor function as calculated by grip strength and rotarod (exhaustion) behavior (Extended Data Fig. 4a,b). To measure the body composition of mice, we used a low-field nuclear magnetic resonance imaging system; overexpression of ULK1 in AD mice did not affect body weight, fat mass or lean tissue mass (Extended Data Fig. 4c–e). Furthermore, compared to AD mice, 5xFAD;Ulk1^{OV} mice showed similar metabolic parameters, including food intake, oxygen consumption, carbon dioxide exhalation, respiratory exchange ratio and energy expenditure, via a metabolic cage system assay (Extended Data Fig. 4f–j). These parameters may differ in older mice and warrant follow-up. Note that ULK1 overexpression in 5xFAD mice achieved a more than twofold change of expression in brain ULK1 but did not impact serum ULK1 level at the age we tested (7 months old) (Extended Data Fig. 4k–n). Collectively, overexpression of ULK1 in the 5xFAD mice did not affect the animals' motor function, body composition or basal metabolism at 7 months old with the method of administration tested.

ULK1 overexpression reduces Aβ pathology in 5xFAD mice

As ULK1 overexpression improved cognition in 5xFAD mice, we asked whether this was due to reduced Aβ burden. We first checked changes of Aβ in the hippocampi of the 7.5-month mice after the MWM: compared to 5xFAD mice, 5xFAD;Ulk1^{OV} mice had fewer Aβ plaques (Fig. 3i,j), which were smaller in size (Fig. 3k) and displayed reduced insoluble $Aβ_{1-40}$ and $Aβ_{1-42}$ (Fig. 3l,m). However, ULK1 overexpression did not reduce soluble $Aβ_{1-40}$ or $Aβ_{1-42}$ in 5xFAD;Ulk1^{OV} mice (Fig. 3n,o). Reduced Aβ burdens were likely contributed by reduced Aβ production and increased phagocytic engulfment when cells were overexpressing ULK1: (1) expression levels of full-length amyloid precursor protein (APP), APP C-terminal fragment and APP N-terminal fragments were significantly lower in hippocampi from 5xFAD;Ulk1^{OV} mice than that from 5xFAD mice (Extended Data Fig. 5a,b); (2) the total number of microglia as well as the average numbers of microglia close to Aβ plaque were increased from 5xFAD to 5xFAD;Ulk1^{OV} mice (Fig. 3p,q and Extended Data Fig. 5c–g); and (3) isolated Ulk1^{OV} microglia had higher phagocytic capacity toward $Aβ_{1-42}$ (Fig. 3r and Extended Data Fig. 5h).

Reactive astrocytosis is an abnormal increase in the number of astrocytes due to severe brain stress, such as that seen in AD[39]. We tested whether ULK1 could change reactive astrogliosis by staining hippocampal tissue with GFAP. ULK1 overexpression in the 5xFAD mice reduced astrocytosis in cornu ammonis (CA1 and CA2–CA3) regions and the dentate gyrus (Fig. 3s and Extended Data Fig. 5i–l). We asked whether reduced Aβ burden would help prevent neuronal loss. However, we did not see differences in neuronal numbers or the thickness of CA1 in any of the ULK1-overexpressing mouse models (Extended Data Fig. 5m–p); this was not surprising as the 7-month 5xFAD mice have weak or no neurodegeneration in CA1[40]. These data suggest that ULK1 mitigates astrocytosis; however, whether ULK1 can slow neurodegeneration should be further tested in an AD model with neurodegeneration. Motivated by the substantial protective effect of ULK1 against Aβ pathology, we asked when the benefit started and how long it might last, and accordingly checked Aβ plaques in 2-, 7- and 19-month-old animals using IF. Compared to 5xFAD, whereas there were reduced Aβ plaques in 2-month-old 5xFAD;Ulk1^{OV} mice (5.6 ± 1.6 versus 1.0 ± 0.5), there was a 43% reduction in 7-month-old 5xFAD;Ulk1^{OV} mice, and the benefit carried over to a nearly 30% reduction in 19-month-old mice (Fig. 3t and Extended Data Fig. 5q). Therefore, ULK1 confers sustained protection against Aβ pathology at multiple age points spanning early, middle and old ages.

Although ubiquitous expression of ULK1 ameliorated Aβ pathology in the 5xFAD mice, this improvement could be attributed to indirect benefits from outside of the brain[41,42]. To minimize peripheral confounders and assess brain-localized effects, we performed hippocampal regional manipulations in CA1. Using AAV2/9-CMV-Ulk1-3xFLAG-WPRE-pA for overexpression and AAV2/9-U6-shRNA (Ulk1)-CMV-EGFP-pA for knockdown (KD) in WT and 5xFAD mice (Extended Data Fig. 6a). IF and western blot (WB) data verified that green fluorescent protein (GFP) was primarily expressed in the hippocampal CA1 region with satisfactory overexpression (2.74 ± 0.10-fold increase) or KD efficiency (from 1 to 0.19 ± 0.03) (Extended Data Fig. 6b–e). Although AAV2/9 is not neuron-specific, in our system it drives predominantly neuronal expression within the injected hippocampal region (Extended Data Fig. 6b,c). We then performed behavioral studies to assess cognition in these mice. CA1 ULK1 overexpression in the 5xFAD mice conveyed no improvement in NOL, NOR or Y-maze (Extended Data Fig. 6f–h). In the MWM test, compared to 5xFAD (scramble) mice, CA1 ULK1 overexpression in 5xFAD mice significantly reduced mouse latency to the platform on training day 7 (Extended Data Fig. 6i,j,p); and on day 8 during the probe trial, it increased exploration frequency and increased time in the target quadrant (Extended Data Fig. 6k–m). ULK1 KD did not exacerbate memory impairment in 5xFAD mice, possibly due to low sensitivity of

Fig. 3 | Overexpression of ULK1 normalizes cognitive deficit and amyloid pathology in 5xFAD mice. a, A graphic abstract depicting genotypes of parental and F1 progeny mice used in behavioral tests to assess cognitive function or dysfunction. **b**–**d**, ULK1 overexpression in the 5xFAD mice improved animals' memory. Results of NOL (**b**), NOR (**c**) and Y-maze (**d**) assays performed in the designated four groups (n = 31, 16, 24 and 16, respectively). Open and closed dots correspond to test results for female and male mice, respectively. **e**–**h**, ULK1 overexpression in the 5xFAD mice increased animals' learning and memory. WT, 5xFAD, Ulk1^{OV} and 5xFAD;Ulk1^{OV} mice (n = 30, 16, 24 and 16, respectively) were subjected to MWM. Swimming trajectories were recorded during the initial 7-day training period of the MWM test (**e**). Results of probe trial test on day 8: representative images (**f**), total time in the target quadrant (**g**) and number of times mice passed the platform location (**h**). **i**–**o**, ULK1 overexpression in the 5xFAD mice reduced animals' Aβ pathologies. Representative images of hippocampal brain region of 7.5-month-old mice stained for Aβ plaques (6E10-positive, green), a microglia marker (Iba1-positive, red) and nucleus (DAPI, blue) (**i**). The number (**j**) and size (**k**) of Aβ plaques were quantified (n = 8, 8, 8 and 7, respectively). ELISA assays were used to detect insoluble $Aβ_{1-40}$ (**l**), insoluble $Aβ_{1-42}$ (**m**), soluble $Aβ_{1-40}$ (**n**), and soluble $Aβ_{1-42}$ (**o**) in hippocampal tissue from mice of the indicated genotypes (n = 8 and 7). Scale bars, 1,000 μm (top rows), 100 μm (middle and bottom rows) (**i**). **p**–**q**, Total number of Iba-1$^+$ microglia per region of interest (ROI) (**p**) and average number of microglia per Aβ plaque (**q**). Data in **q** from 50–132 plaques, with 7 mice per group. **r**, ULK1 overexpression increased microglia phagocytosis (uptake) of $oAβ_{1-42}$ (n = 20–25 microglia per group from a total of 3 biological replicates). **s**, Hippocampal astrocytes (GFAP$^+$ cells per ROI) were counted in designated groups of mice (n = 8, 8, 8 and 7 mice with a total of 23–35 randomly selected fields per group). **t**, Total number of Aβ plaques per ROI (6E10$^+$) was determined in 2-, 7- and 19-month-old mice of the indicated genotypes. n = 5 or 8 mice per group, with 3 slides per mouse. Unless specified elsewhere, data are mean ± s.e.m. Statistical analyses were performed as follows: two-way ANOVA followed by Dunnett's multiple comparisons test (**b**–**d**,**g**,**h**,**j**,**k**,**r**–**t**); repeated measures ANOVA by Turkey's multiple comparisons test (**e**); two-sided unpaired two-tailed Student's t-test (**l**–**q**). $^*P < 0.05$, $^{**}P < 0.01$, $^{***}P < 0.001$.

https://doi.org/10.1038/s43587-026-01108-z

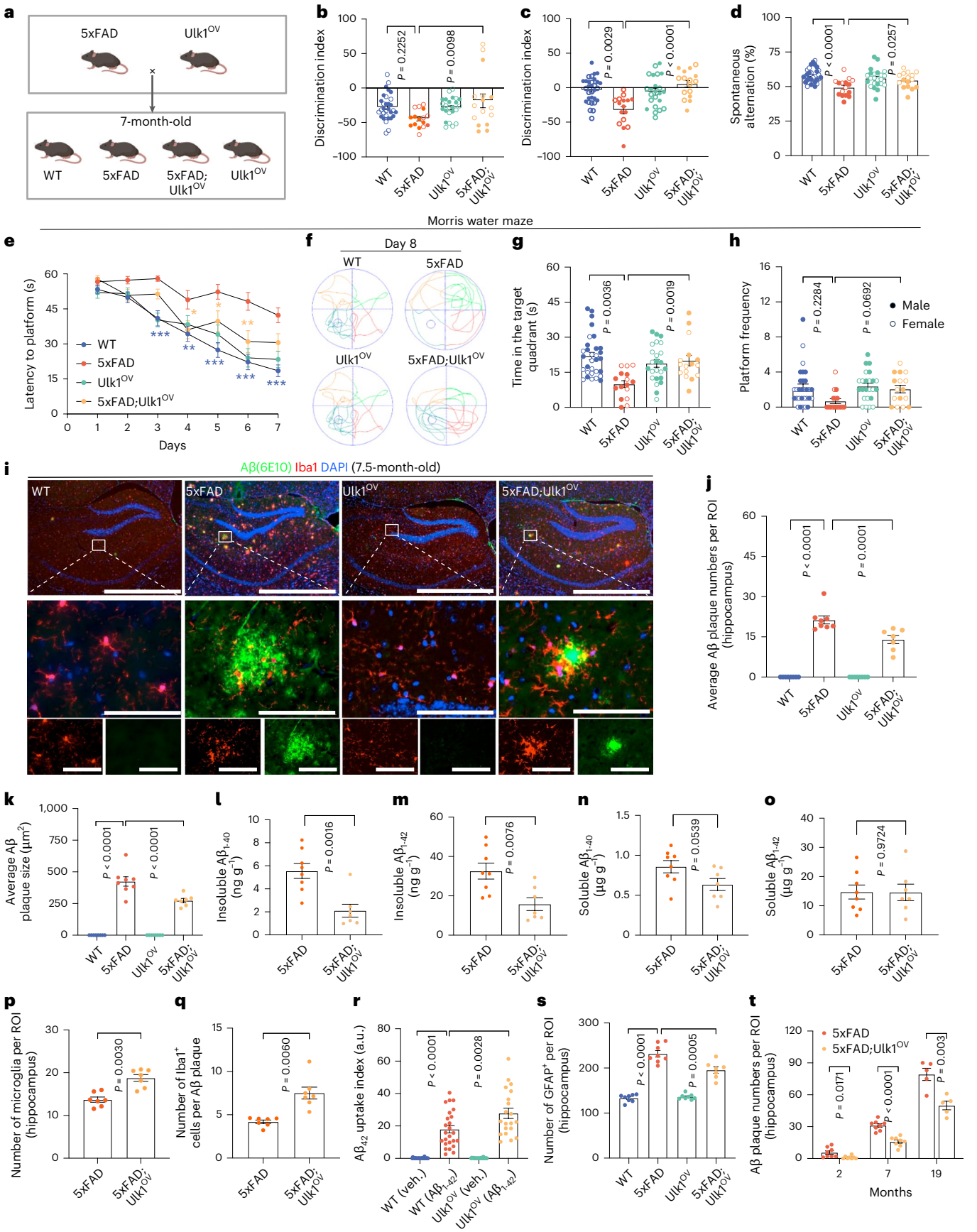

the behavioral protocols. ULK1 overexpression and KD did not change exploration distance or swimming speed (Extended Data Fig. 6n,o,q). In summary, in 5xFAD mice, CA1 ULK1 overexpression improved memory.

ULK1 overexpression normalizes dendritic spine density and promotes mitophagy in 5xFAD mice

Although ULK1 overexpression did not change the number of neurons in the HIP of 5xFAD mice, we undertook a more detailed exploration by analyzing dendritic spine density, which is known to correlate with memory and is reduced in AD[43]. We evaluated changes of the density of Golgi-impregnated hippocampal neuronal dendritic spines from 5xFAD;Ulk1^{OV} and 5xFAD mice (Fig. 4a). The density of apical (or basal) dendritic spines of hippocampal CA1 and CA3 neurons were approximately 20–30% lower in 5xFAD mice than in WT mice. ULK1 overexpression improved the density of dendritic spines in 5xFAD mice (Fig. 4b and Extended Data Fig. 7a–c).

We then explored the molecular mechanisms of ULK1-driven brain Aβ reduction. Initially, we examined whether canonical ULK1 upstream regulators such as mTOR and AMPK pathways were affected in vivo. WB analysis revealed no statistically significant changes in these regulatory pathways in the HIP of 5xFAD;Ulk1^{OV} mice (Extended Data Fig. 7d,e), suggesting that the protective effects may operate through alternative mechanisms. To further investigate these mechanisms, RNA-seq data were generated using hippocampal tissue from WT, 5xFAD, Ulk1^{OV} and 5xFAD;Ulk1^{OV} mice and subject to three-dimensional principal component analysis. Although the transcriptomic profiles were distinctly separated between WT and 5xFAD, ULK1 overexpression normalized the transcriptome of the 5xFAD mice to closely match that of WT mice (Extended Data Fig. 8a). ULK1 overexpression upregulated 222 and downregulated 48 genes in the HIP of 5xFAD mice (Extended Data Fig. 8b). Differentially expressed genes (DEGs) were identified and grouped into eight clusters, showing a high degree of similarity between the transcriptomic profiles of 5xFAD;Ulk1^{OV} and WT mice (Extended Data Fig. 8c,d). For example, cluster 2 was a group of pathways that were reduced in 5xFAD but restored to a level that was even higher than that of WT in 5xFAD;Ulk1^{OV} mice; among these pathways, some were key mitochondrial pathways, such as those related to the reduced nicotinamide adenine dehydrogenase complex (mitochondrial complex I) and proton-transporting ATP synthase complex (mitochondrial complex V). Because we had narrowed our attention to ULK1 in mitochondrial homeostasis, we performed Gene Ontology (GO) enrichment analysis and focused on pathways that were changed in 5xFAD but were normalized to WT-levels by ULK1. Among the markedly changed pathways, many were involved in mitochondrial function and/or energy metabolism, including ATP-coupled electron transport and mitochondrial complexes (Fig. 4c). Our RNA-seq data provide additional evidence of ULK1-associated maintenance of mitochondrial homeostasis as a potential mechanism for how ULK1 abrogates AD pathologies in mice.

Although ULK1 is a key protein in the initiation of autophagy, it also contributes to mitophagy[29,44]. As ULK1 overexpression normalized many of the mitochondrial pathways in the 5xFAD mice (Fig. 4c), we speculated that it may also improve mitochondrial quality via mitophagy. We thus used electron microscopy to visualize and count damaged mitochondria and mitophagy-like events in hippocampal tissue sections from WT, 5xFAD, Ulk1^{OV} and 5xFAD;Ulk1^{OV} mice. Compared with WT mice, 5xFAD mice had higher levels of damaged mitochondria and lower levels of mitophagy-like events (Fig. 4d–f). ULK1 overexpression reduced damaged mitochondria and upregulated mitophagy in the HIP of Ulk1^{OV} mice; similar results were shown in EC and PFC tissue (Extended Data Fig. 7f–k). ULK1 overexpression in the 5xFAD mice increased the ATP level (Fig. 4g). At the protein level, we evaluated autophagic flux (LC3-II/LC3-I ratio after treatment with the autophagy-lysosome inhibitor leupeptin) in hippocampi from WT and 5xFAD mice at 2 and 6 months of age. We found that autophagic flux was reduced in 5xFAD hippocampi and exacerbated with age (Extended Data Fig. 4o–q). We also checked a series of proteins related to autophagy and mitophagy in the hippocampi. Compared to 5xFAD mice, our data suggest higher mitophagy and autophagy in the 5xFAD;Ulk1^{OV} mice (Fig. 4h–k); further validation using mitophagy/autophagy reporter mice are needed. Notably, we observed that ULK1 overexpression significantly elevated Pink1 at both the protein and mRNA levels (Extended Data Fig. 7d–l), suggesting that ULK1 enhances mitophagy through transcriptional upregulation of *Pink1*, pending further molecular mechanism to be addressed. Therefore, our results suggest that ULK1 overexpression protected against Aβ-mediated mitochondrial damage.

ULK1 overexpression mitigates tau pathology

In addition to intraneuronal Aβ and extracellular Aβ plaques, accumulation of tau tangles is another AD pathology. We thus evaluated the capacity of ULK1 to mitigate tauopathy by crossing hTau.P301S mice[45] with Ulk1^{OV} to generate hTau.P301S;Ulk1^{OV} mice (Fig. 5a). Compared to WT mice, hTau.P301S mice showed a significant increase in latency from training day 3 to day 7, whereas latency to the platform was similar for WT and hTau.P301S;Ulk1^{OV} mice (days 4 and 7) (Fig. 5b). The hTau.P301S;Ulk1^{OV} mice exhibited better memory than hTau.P301S mice, as evidenced by greater exploration frequency and longer time in the target quadrant during the probe trial at day 8 (Fig. 5c–e); however, there was no difference when we split male and female mice, very likely due to a small number of animals of each sex (Extended Data Fig. 9a–d).

Accumulation of tau tangles, due to higher p-tau (pTau-Thr181, pTau-Thr217), contributes to AD progression; acetylated tau (acTau-Lys174, acTau-Lys274 and acTau-Lys281) exacerbates p-tau and is proposed as a cause of AD[46–48]. Therefore, we decided to assess tau pathology and specific p-tau and ac-tau sites. Brain sections were assessed using IF targeting pTau-Ser202/Thr205, and although no signal was present in WT mice, a large amount of AT8^{+} tau filaments were

Fig. 4 | Overexpression of ULK1 in 5xFAD mice maintains mouse dendritic spine density and promotes mitophagy. a, Representative images of Golgi staining of apical and basal dendritic spines in hippocampal CA1. **b**, Staining of apical dendrites in CA1 brain region of 7- to 8-month-old mice of the indicated genotype; representative images (upper) quantified data (lower). $n = 4$ mice per group; ≥20 dendritic fragments per mouse were counted. Scale bar, 10 µm. **c**, GO linked to, and hierarchical clustering (Cluster 2) of, genes differentially upregulated or downregulated in the HIP region of 5xFAD mice but normalized in 5xFAD;Ulk1^{OV} mice. GO biological process analysis of Cluster 2 demonstrated enrichment in pathways related to mitochondrial organization and energy production. $n = 3$ mice per group. RNA-seq was performed using total RNA isolated from hippocampal tissue of 7- to 8-month-old mice. **d**–**f**, ULK1 overexpression in the 5xFAD mice increased CA1 stratum pyramidale mitophagy and eliminated damaged mitochondria. Representative set of electron microscopy images (**d**), number of mitophagy events per ROI (**e**) ($n = 6$ mice per group) and damaged mitochondria (percentage of total mitochondria) (**f**). For **e** and **f**, in each group a total of 39–54 random fields from 6 mice were analyzed. Scale bar, 2 µm (**d**). **g**, Relative hippocampal ATP levels in WT, 5xFAD, Ulk1^{OV} and 5xFAD;Ulk1^{OV} mice. $n = 5$ mice per group. **h**,**i**, WB analysis of autophagy-related (LC3B) and mitophagy-related proteins (mitochondrial inner membrane protein MT-CO2/Cox2 and the lysosomal protein cathepsin B) in hippocampal tissues from 5xFAD and 5xFAD;Ulk1^{OV} mice treated with the autophagy-lysosome inhibitor leupeptin to assess autophagic flux. Representative WB images (**h**) and quantified data (**i**). $n = 3$ mice per group. **j**,**k**, ULK1 overexpression in 5xFAD mice increased brain mitophagy as evidenced by higher colocalization of mitochondrial inner membrane protein Cox2 with the lysosomal protein cathepsin B. $n = 4$ mice per group. Relative colocalization of Cox2 and cathepsin B (**j**) and representative set of IF images (**k**). Scale bars, 40 µm (large panels), 2 µm (small panels) (**k**). Unless specified elsewhere, data are mean ± s.e.m. Statistical analysis used two-way ANOVA followed by Dunnett's multiple comparisons test (**b**,**e**–**g**,**i**,**j**). BP, biological process; NADH, nicotinamide adenine dinucleotide (reduced form).

https://doi.org/10.1038/s43587-026-01108-z

present in the hTau.P301S mice, similar to that reported before[45]. Strikingly, compared to the hTau.P301S mice, the hTau.P301S;Ulk1^{OV} mice had an approximately 36% reduction in AT8^{+} tau filaments (Fig. 5f,g). At the molecular level, ULK1 overexpression reduced the abundance of several p-tau phospho-isoforms, including pTau-Thr at 231, 181 and 217 sites (Fig. 5h,i), but did not change the level of pTau-Ser199, pTau-Ser396 or pTau-Ser404 (Extended Data Fig. 9e,f). Note that pTau-Thr181 and pTau-Thr217 are specifically and closely correlated with AD diagnosis and progression[46,49]. It is thus interesting that in hippocampi, ULK1 overexpression in hTau.P301S mice specifically

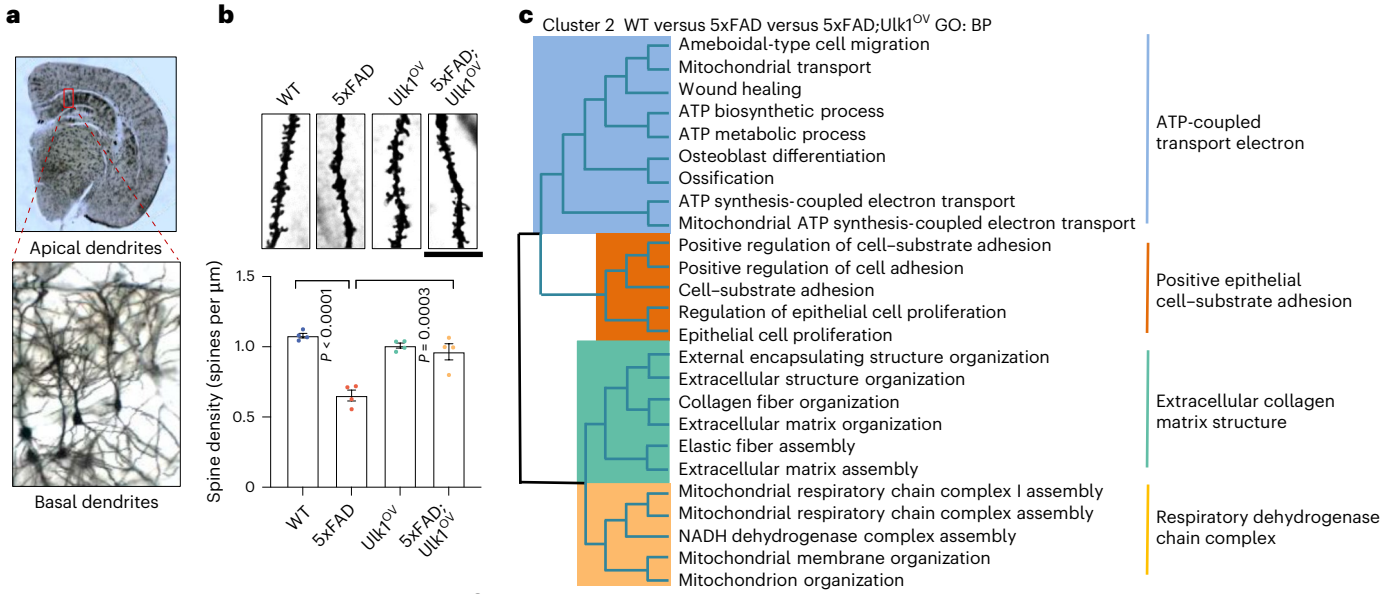

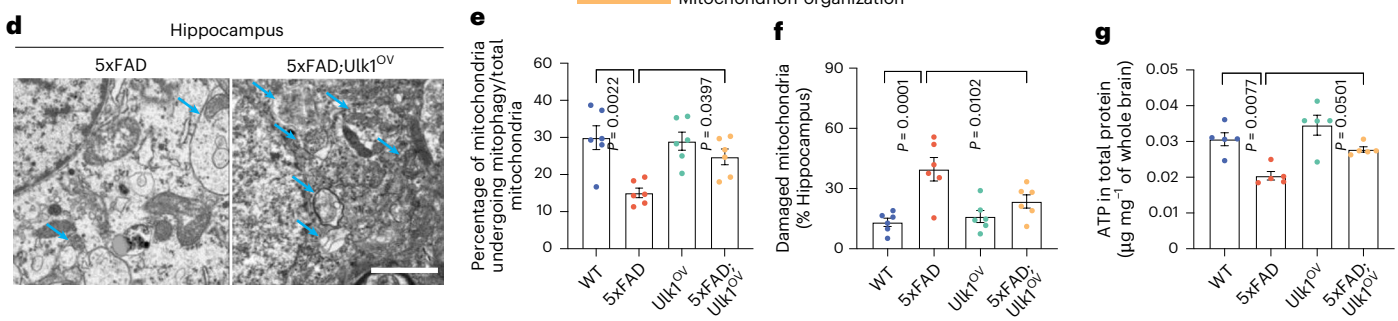

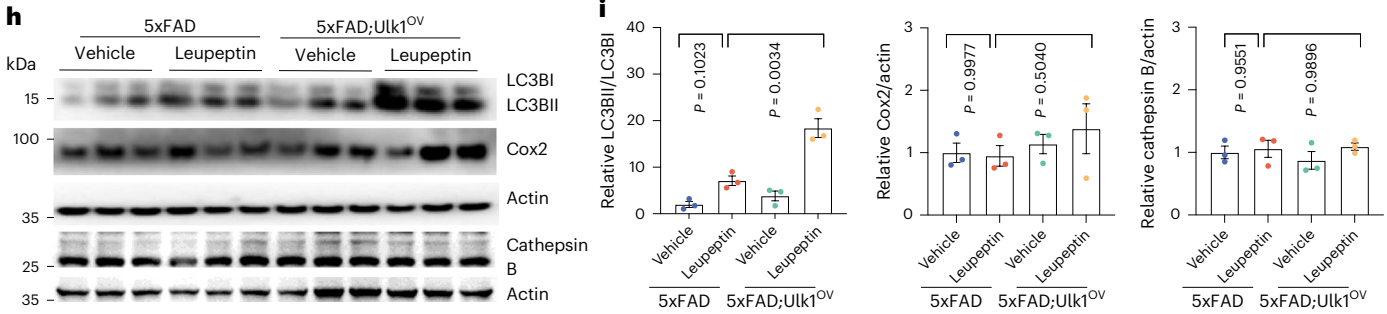

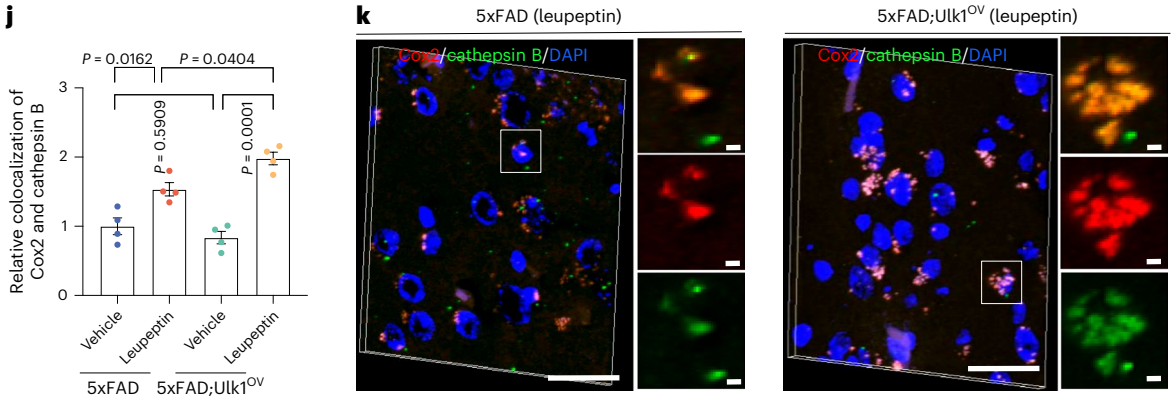

https://doi.org/10.1038/s43587-026-01108-z

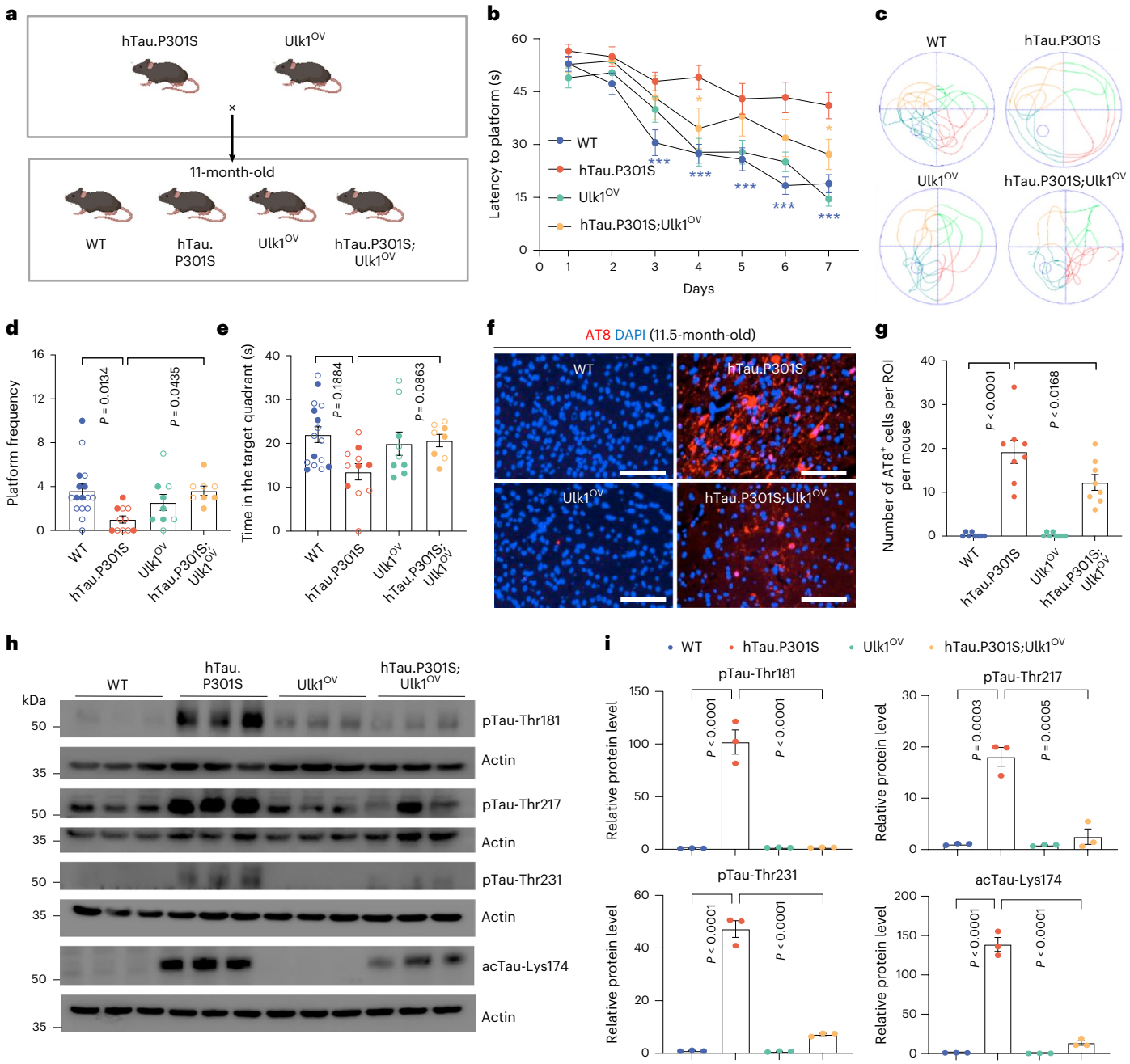

Fig. 5 | Overexpression of ULK1 in hTau.P301S mice improves learning and memory and antagonizes tau pathology. a, Breeding strategy for generating the four groups of experimental mice used in this set of experiments. **b**–**e**, Latencies to hidden platform during the 7-day training period for mice of the indicated genotypes (**b**). Representative images showing the results of the day-8 probe trial (**c**). The number of times mice passed the platform (**d**) and time spent in the target quadrant (**e**) during the probe trial. The numbers of mice used were $n = 16$, 11, 9 and 8 for WT, hTau.P301S, Ulk1^{OV} and hTau.P301S;Ulk1^{OV}, respectively. Open and closed dots correspond to test results for female and male mice, respectively. **f**,**g**, Representative images after immunofluorescence staining of AT8$^+$ cells (**f**) accompanied by quantified data (**g**). For each group, $n = 8$ mice. Scale bars, 100 µm (**f**). **h**,**i**, The levels of p-tau and ac-tau were measured by WB from the hippocampal tissues of WT, hTau.P301S, Ulk1^{OV} and hTau.P301S;Ulk1^{OV} mice. Representative blots (**h**) accomplished with quantifications (**i**). $n = 3$ mice per group. Unless specified elsewhere, data are mean ± s.e.m. Statistical analyses performed were two-way ANOVA followed by Dunnett's multiple comparisons test (**d**,**e**,**g**,**i**); repeated measures ANOVA followed by Tukey's multiple comparisons test (**b**). $^*P < 0.05$, $^{***}P < 0.001$.

reduced AD-related p-tau sites (pTau-Thr181 and 217). Although ULK1 did not reduce acTau-Lys274 and acTau-Lys281, it dramatically reduced acTau-Lys174 to 9.88% (Fig. 5h and Extended Data Fig. 9e,f).

Overexpression of ULK1 impedes acTau-lys174-oriented tauopathy by upregulating the autophagy–NAD$^+$–SIRT1 axis

Although hyperacetylation of tau exacerbates p-tau and is proposed as a cause of AD[46–48], we noticed that ULK1 upregulation dramatically inhibited acTau-lys174 (Fig. 5i). We asked how ULK1 inhibits acTau-lys174 and whether this inhibition plays a role in inhibiting tauopathy. NAD$^+$ is a pivotal metabolite in life and health and is reduced in AD; NAD$^+$ augmentation inhibits AD through different mechanisms including stimulation of autophagy and mitophagy. ULK1 overexpression in hTau.P301S mice significantly enhanced the animal's hippocampal autophagy (Fig. 6a,b). Consistently, in primary hippocampal neurons derived from hTau.P301S mice and hTau.P301S;Ulk1^{OV} embryonic mice,

ULK1 overexpression also enhanced autophagic flux (Fig. 6c,d). Furthermore, ULK1 overexpression in hTau.P301S mice significantly increased hippocampal NAD^+ levels (Fig. 6e). Because the NAD^+-dependent deacetylase SIRT1 plays an important role in removing acetyl groups from acetylated tau to improve brain resilience[50], we checked the deacetylation activity in hTau.P301S;$Ulk1^{OV}$ mice. Compared to hTau.P301S mice, hTau.P301S;$Ulk1^{OV}$ mice had higher SIRT1-based deacetylation activity, as evidenced by low acetylation of its target protein p53 (Fig. 6f–h and Extended Data Fig. 9g). AcTau-Lys174 was positively correlated with tau-seeds-induced generation of tau puncta; accordingly, ULK1 overexpression inhibited acTau-Lys174 in a SIRT1-dependent manner, and this correlated well with the changes in tau puncta (Fig. 6i,j and Extended Data Fig. 9h). This discovery was further validated in primary cortical neurons from hTau.P301S and hTau.P301S;$Ulk1^{OV}$ embryonic mice: ULK1-overexpression-induced acTau-Lys174 inhibition was annulled by a SIRT1 inhibitor selisistat (Fig. 6k,l). Collectively, our data implicate the ULK1–NAD^+–SIRT1 axis in reducing acTau-Lys174 correlating to reduced tau pathology (Fig. 6m). Finally, immunofluorescent staining of AT8 and IBA1 in hippocampi showed higher numbers of microglia and low AT8 signal in hTau.P301S;$Ulk1^{OV}$ mice (Extended Data Fig. 9i,j).

ULK1 overexpression stimulates PINK1-, FUNDC1- and AMBRA1-associated mitophagy

The evidence that ULK1 overexpression ameliorated neurodegeneration-associated memory impairments in 5xFAD and hTau.P301S mice prompted us to ask whether pharmacological activation of ULK1 could achieve similar effects and inform translation. Here we focused on tauopathy, taking advantage of a well-established in vitro tau seeding assay in which adding exogenous tau seeds induces aggregation of Venus-tagged endogenous mutant tau to form green tau foci[23,51]. A tau seeding system was used for two purposes: (1) to check a specific condition for tau-seeds-induced aggregation of tau foci and (2) to check whether these specific conditions could increase the degradation of formed tau foci. Assays were conducted in the absence or presence of ULK1 activators (Rac-BL-918[52] and LYN-1604 dihydrochloride[53]) or inhibitors (SBI-0206965[54] and XST-14[23,55]). ULK1 activator Rac-BL-918 inhibited intracellular p-tau aggregation (in a dose-dependent manner from 0.5 μM to 5 μM) and increased degradation of preformed tau foci (Fig. 7a and Extended Data Fig. 10a,b). The other ULK1 activator LYN-1604 reduced intracellular p-tau aggregation at 4 μM, but at the dose tested it did not change the degradation speed of aggregated tau foci (Extended Data Fig. 10a,b). Furthermore, the ULK1 inhibitor SBI-0206965 showed a trend toward increasing tau puncta formation, whereas the ULK1 inhibitor XST-14 at 5 μM exacerbated intracellular p-tau aggregation but had no effect on degradation of preformed tau foci (Extended Data Fig. 10a,b). To investigate whether the differential pTau-inhibition capacities of ULK1 activators Rac-BL-918 and LYN-1604 were correlated with their distinct mitophagy-induction capacities, we checked mitophagy levels using HeLa cells stably expressing the mitophagy reporter mt-Keima and YFP-tagged Parkin. In line with our hypothesis, the ULK1 activator Rac-BL-918 strongly stimulated mitophagy but ULK1 activator LYN-1604 did not in doses similar to those used for the tau seeding assay; none of the ULK1 inhibitors reduced mitophagy under the chosen conditions (Extended Data Fig. 10c–f). To further validate our findings, primary mouse neurons were treated with ULK1 activators and inhibitors for 24 h, followed by quantification of mitophagy events using a mitophagy detection dye kit. Although the ULK1 activator Rac-BL-918 (5 μM) increased neuronal mitophagy 2.7 times, the other ULK1 activator, LYN (4 μM), showed a trend toward mitophagy induction ($P = 0.061$). On the other hand, the ULK1 inhibitors (5 μM SBI and 5 μM XST) showed a trend toward inhibiting neuronal mitophagy (Extended Data Fig. 10g,h). These findings validate the key role of ULK1 in the inhibition of tauopathy and furthermore the possibility of pharmacological inhibition of tauopathy via turning up ULK1 activity.

Based on the robustness seen in the induction of neuronal mitophagy and inhibition of tauopathy, we focused on the ULK1 activator Rac-BL-918. Off-target effects are common when using small molecules, so we further asked whether Rac-BL-918-induced inhibition of tauopathy was dependent on ULK1 rather than on other ULK1-independent pathways. To address this question, we used short interfering RNA (siRNA) targeting *ULK1* and reached over 99% KD efficiency (Extended Data Fig. 10i). With this approach, our data show that ULK1 was essential in inhibiting tau aggregation as well as in Rac-BL-918-induced tauopathy inhibition (Fig. 7b). Among the five mammalian Atg1 homologs (ULK1-4, STK36), ULK1 and ULK2 are 52% identical, sharing 78% homology within their protein kinase domains, and are functionally redundant in some conditions[56]. To further investigate whether the specificity of Rac-BL-918-induced tauopathy inhibition was dependent on ULK2 or not, we applied a similar KD strategy (Extended Data Fig. 10i). Unlike ULK1, ULK2 was not essential for the inhibition of tauopathy and did not participate in Rac-BL-918-induced tauopathy inhibition (Fig. 7c). The results point to an essential role for ULK1 in inhibiting tauopathy and indicate that Rac-BL-918-induced tauopathy inhibition was dependent on ULK1 but not ULK2.

As Rac-BL-918-induced tauopathy inhibition was dependent on ULK1, we wondered whether any other key autophagy proteins (AMBRA1, Atg5 and Beclin1) and/or mitophagy proteins (AMBRA1, FUNDC1, BNIP3, NIX, PINK1 and Parkin)[12] participate in this process. In addition to including siRNA-*ULK1*, we included siRNA-*GSK3β* as an independent internal control: GSK3β KD reduced the formation of tau puncta and accelerated the degradation of preaggregated tau foci (Fig. 7d,e and Extended Data Fig. 10i). First, we achieved high KD efficiency of the aforementioned genes (Extended Data Fig. 10i). In addition to ULK1, FUNDC1, PINK1, AMBRA1 and Beclin1 also participated in autophagic/mitophagic inhibition of the formation of tau puncta (Fig. 7d); among the tested genes, only *ULK1* and *Beclin1* were essential in reducing preformulated tau puncta (Fig. 7e). Our data further consolidated the role of ULK1-induced autophagy and ULK1-induced mitophagy in inhibiting tauopathy. We further tested whether this reduction was preserved in animals. We carried out an

Fig. 6 | Overexpression of ULK1 impedes acTau-lys174-oriented tauopathy by upregulating the autophagy–NAD^+–SIRT1 axis. a,**b**, Representative WB images (**a**) and quantified data (**b**) of autophagy-related (LC3B) and mitophagy-related proteins (mitochondrial inner membrane protein MT-CO2/Cox2 and the lysosomal protein cathepsin B) in hippocampal tissues from hTau.P301S, $Ulk1^{OV}$ and hTau.P301S;$Ulk1^{OV}$ mice treated with the autophagy-lysosome inhibitor leupeptin to assess autophagic flux. $n = 3$ mice per group. **c**,**d**, Representative WB images (**c**) and quantified data (**d**) of autophagy-related (LC3B) and mitophagy-related proteins (mitochondrial inner membrane protein MT-CO2/Cox2 and the lysosomal protein cathepsin B) in primary cortical neurons from hTau.P301S, $Ulk1^{OV}$ and hTau.P301S;$Ulk1^{OV}$ mice treated with the autophagy-lysosome inhibitor bafilomycin A1 (Baf1) to assess autophagic flux. $n = 3$ biological sets. **e**, NAD^+ levels in the hippocampal tissue of four groups of mice ($n = 4$ mice per group). **f**, Changes of *Sirt1* gene expression in designated groups ($n = 4$ mice per group). **g**,**h**, Quantification of Sirt1 (**g**) and ac-p53 (**h**) protein levels in designated groups ($n = 3$ mice per group). Original WB data are shown in Extended Data Fig. 9g. **i**,**j**, Overexpression of ULK1 inhibits acTau-lys174 and tau tangles. Quantified data from acTau-lys174 (**i**) and tau aggregation (**j**) in HEK293 cells expressing 0N4R P301S Tau-Venus ($n = 14$ technical repeats from a total of 3 biological replicates). **k**,**l**, Representative images (**k**) and quantification data (**l**) of ac-Tau174 staining of primary cortical neurons from hTau.P301S and hTau.P301S;$Ulk1^{OV}$ mice treated with or without the SIRT1 inhibitor selisistat. Nuclei were stained with DAPI. $n = 12$ technical repeats from a total of 3 biological replicates. Scale bars, 50 μm (**k**). **m**, Schematic diagram of the proposed pathway. Unless specified elsewhere, data are mean ± s.e.m. Statistical analyses performed were two-way ANOVA followed by Dunnett's multiple comparisons test (**b**,**d**–**j**,**l**).

https://doi.org/10.1038/s43587-026-01108-z

olfactory-dependent chemotaxis assay to investigate memory-like behavior in WT (N2) and hTau[P301L] *C. elegans*, which uses preconditioning to isoamyl alcohol (IA) during starvation as a cue, where a lower score correlates with better learning/memory[11,57]. Compared to the N2 control, neuron-specific KD of *unc-51* (the *C. elegans* ortholog of mammalian *ULK1*) itself impaired memory (Fig. 7f). Similarly, the ULK1 inhibitors SBI and XST-14 caused a functional memory deficit in N2$^{n\text{-}sid\text{-}1OV}$ *C. elegans* (Extended Data Fig. 10j). Conversely, hTau[P301L] animals had reduced memory, and administering the ULK1 activator Rac-BL-918 to animals improved memory in the hTau[P301L] animals in a ULK1/UNC-51-dependent manner (Fig. 7f). As ULK1 is essential for autophagy and mitophagy[29,44], we asked whether ULK1-dependent mitophagy plays a role in memory restoration in the hTau[P301L] *C. elegans*. We generated a neuronal ULK1-overexpressing worm model named *unc-51$^{n\text{-}OV}$* and crossed it with the tau model to generate hTau[P301L];unc-51$^{n\text{-}OV}$ animals. In line with the above data in mice (Fig. 5), neuronal overexpression of UNC-51 improved memory in the tau worms (Fig. 7g). Importantly, KD of neuronal *pink-1* and *fndc-1*

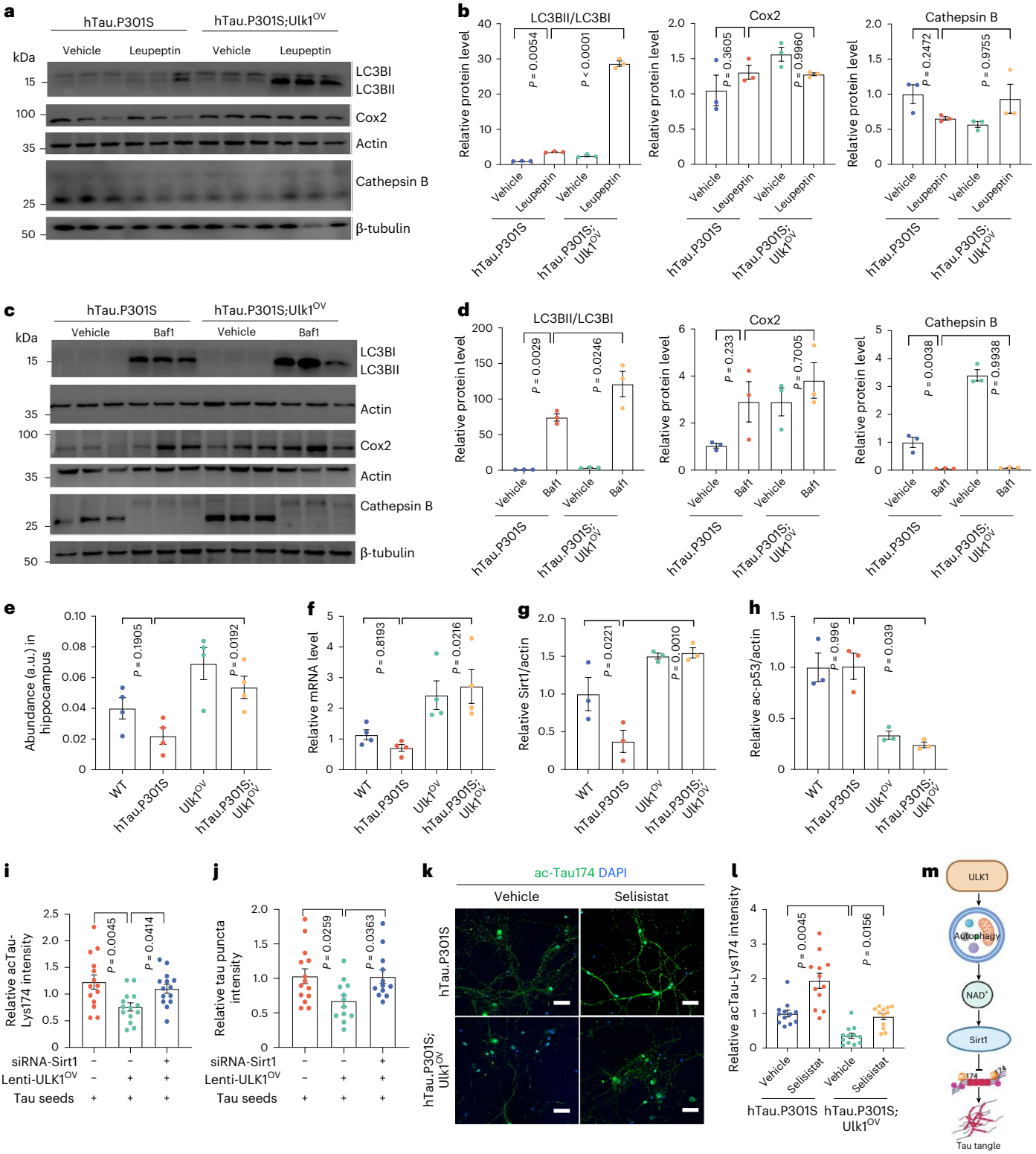

(the *C. elegans* ortholog of the mammalian *FUNDC1*) annulled UNC-51 overexpression-induced memory improvement (Fig. 7g). Collectively, these in vitro and in vivo data suggest that Rac-BL-918 is a specific pharmacological ULK1 activator, counteracting tauopathy and memory loss in a mitophagy-dependent manner.

Discussion

This study suggests that ULK1 is downregulated during normal human aging and that this downregulation is exacerbated in and correlates with disease progression in AD. Although our serum and CSF data indicate a reduction in ULK1 during aging in the CU group after a 4-year follow-up, further multiple linear regression analysis did not suggest a correlation ($\beta = -0.12$, $P = 0.21$; Supplementary Table 6). This could be due to limited sample size and high variability, and large clinical studies will be necessary to resolve it. On the other hand, multiple linear regression analyses showed a positive correlation between CSF ULK1 levels and age in patients with AD ($\beta = 0.14$, $P = 0.007$; Supplementary Table 5). ULK1 in CSF and serum could be present in extracellular vesicles[58], exophers jettisoned by neurons[59] and degraded neurons (released to biofluids due to the leaking of the blood–brain barrier in AD); we speculate that the older a patient with AD is, the higher the likelihood of increased CSF ULK1 sourced from degraded neurons. Again, further studies are needed. Note that within the CU group, our 'paradoxical' data (on the positive correlation between serum, CSF ULK1 and T+) suggest an increase of cellular ULK1-associated autophagy to compensate for the higher tauopathy, safeguarding cognition; this hypothesis should be tested in the future.

We furthermore show that ULK1 positively regulates autophagy and mitophagy across species and may have potential as a therapeutic target or diagnostic biomarker in human patients with AD. ULK1 reduces Aβ and tau pathology by enhancing autophagy- and mitophagy-mediated clearance of aggregated proteins. ULK1 also modulates pathways linked to p-tau and ac-tau. In a translational approach, activating ULK1 via a small molecule Rac-BL-918 inhibits AD pathology and improves memory in a tau *C. elegans* model, highlighting the possibility that modulating ULK1 could be a feasible approach in future anti-AD drug development. Collectively, ULK1-associated autophagy and mitophagy are important in inhibiting the formation of tau puncta; ULK1-associated autophagy (Beclin1) (not mitophagy in the current experimental setting) is important for the degradation of preformed tau puncta; ULK1-mediated memory in AD-like worms is at least significantly managed by PINK1- and FUNDC1-associated mitophagy.

Importantly, our findings that the ULK1–Beclin1–autophagy axis reduces tau pathology align with earlier reports on the role of Beclin1 against Aβ and aging. From the perspective of autophagy, ULK1 phosphorylates Beclin1 (Ser14) to enhance the activity of the ATG14L-containing VPS34 complexes, finally resulting in full autophagic induction[60]. Genetic activation of autophagy could be achieved by Becn1 gain of function via knocking-in of point mutation F121A, which reduces the interaction of Beclin1 with its inhibitor BCL2. Intriguingly, this *Becn1*$^{F121A/F121A}$ mutation caused significant autophagic degradation of Aβ oligomers and improved cognition in the 5xFAD mice[24]. In line with this, *Becn1*$^{F121A/F121A}$ mutation also increased lifespan and healthspan in mice, highlighting a pivotal role for a higher level of basal autophagy in healthy longevity[61]. Similarly, pharmacological reactivation of the AMPK–ULK1 axis using metformin has been shown to reverse mitochondrial abnormalities and promote the lysosomal degradation of APP C-terminal fragments and Aβ aggregates, thereby mitigating neuroinflammation and rescuing cognitive deficits in AD models, further supporting the therapeutic potential of restoring autophagy-initiation signaling[62]. Taken together, results from previous works and this current one converge on turning up the ULK1–Beclin1–autophagy pathway as a potential therapeutic pathway to forestall AD pathologies.

Substantial clinical and experimental data presented here encourage us to propose ULK1 as an important brain protector that helps ensure healthy aging. ULK1 is reduced during aging and is essential in neuronal resilience and cognition. Our data show a dramatic reduction of ULK1 in the cognitively normal older human population over a 4-year period and, moreover, that neuronal-specific ULK1 KD and pharmacological ULK1 inhibition impair memory. These data signal a neuronal protective role for ULK1. Mechanistically, ULK1 increased neuronal resilience against excitatory and metabolic challenges as well as brain toxic proteins. Conversely, ULK1 reduction appears to contribute to AD based on our findings (1) showing reduced serum and CSF ULK1 in a clinically well-characterized AD cohort (versus CU), (2) showing that the severity of reduced ULK1 in different post-mortem human AD brain regions positively correlates with Braak-associated tauopathy, and (3) showing that ULK1 upregulation forestalled AD pathologies and memory loss in Aβ- and tau-bearing mice. In line with a causative role for ULK1 reduction in AD progression, our CDR-SB data indicate that higher baseline CSF ULK1 levels are associated with better maintenance of cognition after adjusting for related mixed clinical factors.

A defining feature of AD is its selective vulnerability, with excitatory neurons and the EC representing early sites of tauopathy[63]. Our cell-type analyses suggest that ULK1 is preferentially reduced in excitatory neurons with advancing Braak stage. Our current data from a set of post-mortem human samples likely support this hypothesis; during a comparison of the numbers of ULK1^{+} neurons and the average intensity of ULK1/neurons between post-mortem EC and HIP, we noticed a

Fig. 7 | Pharmacological or genetic upregulation of ULK1 antagonizes tau pathology in human cells and *C. elegans*. **a**, Tau puncta formation (left) and degradation of preformed tau puncta (right) were quantified in HEK293 cells expressing 0N4R P301S Tau-Venus in the presence or absence of ULK1 activator Rac-(BL)-918. *n* = a total of 50 randomly selected fields per group from 3 biological replicates. **b**,**c**, HEK293 P301S tau-Venus cells were transfected with siRNA-ULK1 (**b**), siRNA-ULK2 (**c**) or siRNA-scramble (**b**,**c**), and transfected cells were incubated with or without 5-μM Rac-(BL)-918 in the presence of 10-nM tau seeds. Graphs in **a**–**c** show normalized fluorescence intensity relative to vehicle control (**a**) or in the absence of Rac-(BL)-918 (**b**,**c**), as indicated. *n* = a total of 54 randomly selected fields per group from 3 biological replicates. **d**, Rac-(BL)-918 inhibited the formation of tau puncta dependent on ULK1, FUNDC1, PINK1, Ambra1 and Beclin1. HEK293 P301S tau-Venus cells were transfected with siRNA-scramble or a siRNA candidate, followed by treatment with 10-nM tau seeds and 5-μM Rac-(BL)-918 simultaneously. *n* = a total of 36–40 randomly selected fields per group from 3 biological replicates. **e**, Rac-(BL)-918 increased the degradation of preformed tau puncta dependent on ULK1 and Beclin1. HEK293 P301S tau-Venus cells were transfected with siRNA-scramble or a siRNA candidate, followed by subsequent treatment with 10-nM tau seeds and 5-μM Rac-(BL)-918. *n* = a total of 36–40 randomly selected fields per group from 3 biological replicates. **f**, Associative memory tests were administered to adult day-2 transgenic *C. elegans* expressing hTau[P301L] *n*-sid-1^{OV} in the presence of siRNA targeting *unc-51/ULK1* or control siRNA in the presence of Rac-(BL)-918, where indicated. Data are shown in the format of % CI, where a lower score corresponds to greater response to odorant and better memory function. *n* = 3 biological sets. **g**, Associative memory tests were administered to adult day-2 transgenic *C. elegans* expressing hTau[P301L] *n*-sid-1^{OV} in the absence or presence of siRNA to *pink-1* or *fndc-1/FUNDC1*. Data are shown in the format of % CI, where a lower score corresponds to greater response to odorant and better memory function. *n* = 5 biological sets. In the box plots, the center line denotes the median, box range indicates the 25th–75th percentile and whiskers denote minimum and maximum values. Unless specified elsewhere, data are mean ± s.e.m. Results represent pooled data from three to five biological replicates. Violin and box plots are centered around the median with interquartile ranges and all data points shown; the shape of the plot reflects the distribution of data. Statistical significance was determined using the Kruskal–Wallis test (non-normal data distribution) or one-way ANOVA (normal data distribution) (**a**–**e**) or two-way ANOVA followed by Tukey's multiple comparisons test (**f**,**g**).

https://doi.org/10.1038/s43587-026-01108-z

reduced neuronal ULK1 level in the EC and HIP in AD. In the PFC, in AD there was a trend toward the reduction of ULK1^{+} neurons/total neurons.

Several challenges need to be further explored. First, the decline of ULK1 in brain tissue and biofluids observed during aging and AD may be attributed to several mechanisms. Although reduced ULK1 in AD could be due to lower transcription in specific cell types (including excitatory neurons and astrocytes; Fig. 1i), it could also be caused by increased ULK1 degradation; the upstream pathways controlling ULK1 stability should be investigated[64,65]. Note that the transcription levels of other components of the ULK1 initiation complex (*ATG101*, *RB1CC1*/*FIP200* and *ATG13*) were also lower in AD excitatory neurons (Extended Data Fig. 1i–k), indicating that further studies on their protein levels, activities, and effects on autophagy in AD should be explored. Second, is it possible to uncouple ULK1-associated autophagy and ULK1-associated mitophagy in neuroprotection? This is a conceptual and experimental challenge as mitophagy is a subtype of autophagy, so changes to mitophagy could affect autophagy and vice versa. However, our in vitro and in vivo data do suggest that ULK1-associated mitophagy plays a dominant role in neuroprotection and elimination of AD pathologies; ULK1 overexpression improves the mitochondrial transcriptomic profile and mitochondrial homeostasis (Fig. 4), and key mitophagy proteins FUNDC1 and PINK1 were essential

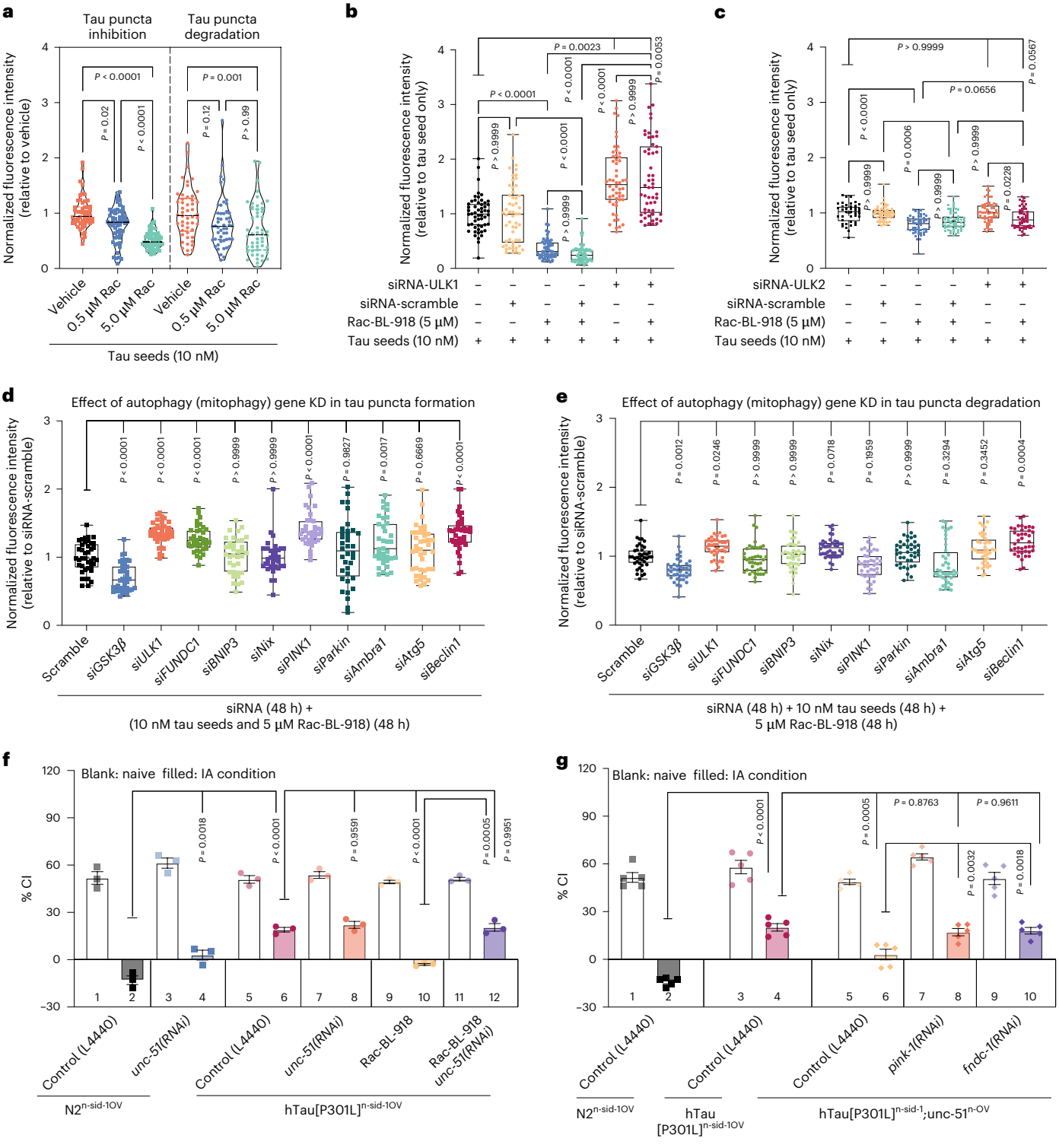

in ULK1 inhibition of tau tangles and memory loss (Fig. 7). Such data are in line with the essential roles of ULK1 in PINK1-dependent-mitophagy[29] and FUNDC1-dependent mitophagy[66]. Third, some CSF samples from the CU control group that showed individuals with high tau (T+) also showed high ULK1 levels (Supplementary Table 4), especially when all CU individuals were cognitively normal. We hypothesize that elevated CSF ULK1 in CU T+ individuals may reflect a protective/compensatory response that helps preserve cognition despite tau pathology. This hypothesis should be further tested in preclinical and clinical studies. Fourth, the activities and roles of AMPK and mTORC1 in AD and how they interact with ULK1 need to be investigated. Although our initial exploration did not capture any differences between the activity of mTOR (p-mTOR at Ser2448) or AMPK (p-AMPKα at Thr172) in the hippocampi of 5xFAD and 5xFAD;Ulk1^{OV} mice (7 months old; Extended Data Fig. 7d,e), possibly due to small sample size, further studies with a larger sample size and other endpoints (for example, additional mTORC1/AMPK readouts) are needed. Finally, the ULK1 activator Rac-BL-918 is a robust neuronal mitophagy inducer and shows the capacity to inhibit tauopathy and memory loss in an ULK1-associated manner; further validation studies in mice and in human induced pluripotent stem cell-derived neurons (or a neuron-glia coculture system) should be performed.

Our results do not imply that mitophagy outweighs other autophagy pathways but underscore the importance of mitochondrial homeostasis for overall autophagic function. The initiation and progression of macroautophagy requires ATP, as the initiation of chaperon-mediated autophagy is ATP-dependent. Similarly, microautophagy uses ATP to sequester cargo (review in ref. 67). Furthermore, the mechanism by which ULK1 decreases phosphorylation and acetylation of tau remains obscure. Our data show that ULK1 overexpression rebalanced the levels of proteins involved in the regulation of pTau-Thr231/181/217 and acTau-Lys174. Our memory data in *C. elegans* indicate that ULK1-associated mitophagy contributes fully to memory improvements as KD of key mitophagy proteins (PINK1 and FNDC1/FUNDC1) almost completely annulled these improvements via ULK1 overexpression (Fig. 7g). However, in view of the existence of the many kinase substrates in addition to FUNDC1 and the PINK1 downstream protein Parkin[66,68,69], as well as the limitations of our methods and model systems, we speculate that there is a high probability that ULK1 overexpression could also inhibit tau spreading and pathology via additional kinase substrates and via mitophagy/autophagy-independent pathways in rodents and humans. In addition, although our AAV2/9-CMV-based ULK1 overexpression model was not neuron-specific, future works should use neuron-specific promoters (for example, hSyn, CamKIIα) to test the neuron-specific roles of ULK1.

Looking ahead, recent advances with anti-Aβ antibodies lecanemab and donanemab show promising clinical efficacy, reducing memory decline by 25–35%, despite some associated adverse effects[70,71]. This encouraging result highlights the multifactorial complexity of AD, which involves not only Aβ plaques and tau pathology but also inflammation, oxidative stress, metabolic dysfunction and aging-related processes[15,63,72,73]. The causal role of Aβ and tau aggregates in AD is still being debated[74], underscoring the need to investigate broader pathogenic mechanisms—including autophagy and mitophagy[9,19,23,75–77]. To note, although our clinical and preclinical data point to a hypothesis of reduced ULK1 as a correlation of disease progression in AD, further direct data linking the two are needed. Additionally, our recent studies further reveal distinct alterations in ULK1 and related autophagy or lysosomal proteins in CSF and serum across the AD continuum, with differential patterns observed between AD and frontotemporal lobar degeneration. These findings support the potential of ULK1 and associated proteins as biomarkers for tracking AD progression[78,79]. Our data are in line with another clinical study showing altered expression of several autophagy proteins, including ATG5, UBQLN2, ULK1 and LC3, in AD, dementia with Lewy bodies and frontotemporal dementia[80]. All in all, to accelerate progress toward an effective strategy to manage the large socioeconomic and public health burden of AD, our study presents a strong case for the development of ULK1 as a potential therapeutic target and disease progression biomarker for AD.

Methods

The human study was performed according to the principles of the Helsinki declaration and King's College London. All participants gave their written informed consent before participating in the study. The regional Ethics Committee for medical research in the South-East of Norway (REK 2011/2052, REK 2017/371 and REK 82685) and the Data Protection Officer at our institution approved the study. All experiments and animal were approved by the Jinan University Institutional Animal Care and Use Committee (IACUC-20181029-01).

Study participants

Memory Clinic Cohort (patients with AD). We included 316 patients with AD including 56 patients with AD-MCI and 260 AD-dementia. AD patients were recruited from the memory clinics at Oslo University Hospital (n = 180) and St. Olav's University Hospital, Trondheim (n = 136) during the period from 2010 to 2018. The patients were included in the Norwegian Registry of Persons Assessed for Cognitive Symptoms (the NorCog registry) and went through a comprehensive clinical assessment following a standardized research protocol[81] including an interview with the patients and their caregivers, cognitive testing, physical examination, blood sampling, imaging (computed tomography, magnetic resonance imaging, fluorodeoxyglucose-positron emission tomography) and lumbar puncture. All patients met the clinical criteria of probable or possible AD or AD mixed with cerebrovascular disease according to the US National Institute of Aging and the Alzheimer's Association criteria[82,83]. Patients who underwent a minimum of one follow-up at the clinics after the baseline examination were included in the progression analyses (n = 254). Cognitive and functional impairment was assessed by the CDR scale[84] post hoc by certified CDR raters based on all the information from the clinical records. The categories of memory, orientation, judgment and problem-solving, community affairs, home and hobbies and personal care were given a score of 0–3 (higher values indicating more severe impairment) and summed up to give the CDR-SB (0–18)[85,86]. The AD core CSF biomarkers were analyzed at Akershus University Hospital (Ahus) by enzyme-linked immunosorbent assays (ELISA; Innotest hTau Ag, phoshoTau (181P) and β-amyloid 1–42 Fujirebio Europe). Specific cut-offs provided by the laboratory were applied and used when categorizing the patients according to the AT (N) classification[87]: A, $A\beta_{42}$ > 700 pg ml^{-1}; T, p-tau$_{181}$ < 80 pg ml^{-1}; and age-adjusted cut-off concentrations for N, total tau < 300 pg ml^{-1} for patients under the age of 50, 450 pg ml^{-1} for those aged 50–70 years and < 500 pg ml^{-1} for those older than 70 years.

CU controls (the COGNORM study). Additionally, 75 CU older controls were recruited when referred to hospital for elective gynecological orthopedic or urological surgery. These patients were assessed with the same battery of cognitive tests as the memory clinic patients, and the majority were cognitively followed yearly for up to 5 years. At baseline, CSF was collected in conjunction with spinal anesthesia at the time of surgery. Repeated CSF sampling was performed in a subgroup of CU controls who volunteered for a second lumbar puncture (n = 22) after 4.48 years (0.48 s.d.). Further details of this cohort are available elsewhere[88]. CSF AD core biomarkers were analyzed in the Sahlgrenska University Hospital (Mölndal, Sweden) by ELISA (Innotest hTau Ag, phoshoTau (181 P) and β-amyloid 1–42 Fujirebio Europe). Their laboratory-specific cut-offs were applied: A, $A\beta_{42}$ > 530 pg ml^{-1}; T, p-tau$_{181}$ < 60 pg ml^{-1}; and N, total tau < 350 pg ml^{-1} (ref. 89). These cut-offs were applied when categorizing the CU controls according to the AT (N) classification[87].

CSF and serum ULK1 measurements. Aliquoted CSF and serum samples from the Memory Clinic Cohort and CU controls were transferred from Oslo University Hospital on dry ice and were stored at −80 °C until assays were performed at the Department of Clinical Molecular Biology, Akershus University Hospital (EpiGen). ULK1 protein was quantified in CSF and serum using commercially available sandwich ELISA Kits (Nordict Biosite, cat. no. EKX-PZ9LPK-96) following the manufacturer's instructions. Samples were processed after the same freeze–thaw cycle and plated at twofold to fourfold dilution. Each assay plate also included multiple dilutions of manufacturer-provided calibration standards. Protein concentrations (pg ml^{-1}) were calculated using appropriate calibration standards. Log transformations of data were applied, as needed, to calculate serum ULK1.

Bioinformatics analysis. RNA-seq data were obtained from publicly accessible MIT datasets[34]. We processed the single-cell raw data using the Seurat package. Specifically, we kept genes detected in more than 2 cells and kept all cells with at least 200 detected genes. We identified outlier cells based on multiple quality metrics, including unique gene count, the ratio of mitochondrial RNAs relative to endogenous RNAs and total gene count. Cells that passed quality control were log-normalized using a scale factor of 10,000. The Louvain algorithm in Seurat was implemented to detect clusters. The cell type of each cluster was identified from corresponding marker genes as described elsewhere[87].

Human brain immunofluorescence and quantification. The experiments were performed similarly to what we have published elsewhere[76]. Human brain sections (7 µm) were rehydrated from xylene to water, rinsed in phosphate-buffered saline (PBS) and blocked in 5% bovine serum albumin in tris-buffered saline + Triton X-100/Tween-20 for 1.5 h. Sections were incubated overnight at 4 °C with primary antibodies (1:300) in tris-buffered saline + Triton X-100/Tween-20, rinsed and incubated with secondary antibodies (1:1,000). After PBS washes, slides were mounted with Prolong Gold with 4, 6-diamidino-2-phenylindole (DAPI; Invitrogen, P36931). Tissues included EC, HIP and PFC from controls and Braak staging 1/2, 3/4 and 5/6. Primary antibodies used were anti-ULK1 (Sigma, A7481) and anti-Map2 (Novus Biologicals, B91375). Secondary antibodies used were anti-Rabbit Alexa-546 (Invitrogen, A10040) and anti-Mouse Alexa-488 (Invitrogen, A-11001). Imaging was performed on a Zeiss AxioScan Z1 (×20, numerical aperture 0.8) and analyzed via ZEN lite blue. Eight 5-$µm^2$ grid squares per region were quantified to ensure even distribution.

Animal maintenance. All animals were maintained at the Jinan University Institutional Animal Care Facility (Guangdong, China) under standard conditions. In brief, mice were housed in standard cages (dimensions 22.2 cm × 30.8 cm × 16.24 cm) with autoclaved corncob bedding and a nestlet for enrichment and normally with no more than four mice per cage. The lights were turned off at 8:00 p.m. local time and back on at 8:00 a.m. each day. Mice were fed a standard diet (including amino acids, minerals and vitamins) throughout their lives. The standard diet was purchased from Collaborative Biotechnology (catalog no. XTI01CR-004).

Generation of transgenic mice. $Ulk1^{OV}$ mice (C57BL/6-Tg (CAG-Ulk1)1Cyagen) were generated by Cyagen Biosciences via pronuclear injection of a Cre-loxP-dependent CAG-Ulk1 construct. Genotyping was performed using PCR primers: Pair 1 (F: GTTCGGCTTCTGGCGTGTG, R: TCCTTGCGAGAGAACTCGAAC; 325 bp); Pair 2 (F: TTGATGAGATGTTCCAGCACCGAG, R: TAGCCAGAAGTCAGATGCTCAAGG; 339 bp); and GAPDH (F: CCTTCCGTGTTCCTACCC, R: CCCAAGATGCCCTTCAGT; 150 bp). The colony, registered in the Jackson Laboratory as C57BL/6-Tg (CAG-Ulk1)1Cgen/Eff (synonym $Ulk1^{OV(UBQ)}$; simplified here as $Ulk1^{OV}$), was maintained by breeding $Ulk1^{OV}$ male mice to WT female mice. 5xFAD mice (Jackson catalog no. 034848, via Wei Wei Lab) and Thy1-hTau.P301S mice (gift from M. Goedert) were bred with $Ulk1^{OV}$ females to generate 5xFAD;$Ulk1^{OV}$ and hTau.P301S;$Ulk1^{OV}$ cohorts, respectively. Behavioral assays were conducted at 7 or 12 months. For Aβ-related (WT, 5xFAD, $Ulk1^{OV}$ and 5xFAD;$Ulk1^{OV}$) and tau-related (WT, hTau.P301S, $Ulk1^{OV}$ and hTau.P301S;$Ulk1^{OV}$) mouse studies, pathological and molecular analyses were performed on the same animals used for behavioral testing. Separate cohorts of 5xFAD mice were utilized for AAV-mediated CA1 overexpression and metabolic studies. The gender, age and number of mice used in each experiment are provided in the figure legends.

Neuronal survival assays (cell death assays). Cellular death was assessed using two methods: Hoechst dye staining[36] and the TUNEL assay (to detect DNA fragmentation)[90]. Briefly, primary cultured neurons were treated with KA (0µ M, 10 µM, 50 µM, 100 µM, 200 µM), NMDA (0 µM, 10 µM, 50 µM, 100 µM, 200 µM), 3-NPA (0 mM, 1 mM, 5 mM, 10 mM), rotenone (0 µM, 1 µM, 10 µM, 100 µM) or oligomer $Aβ_{1-42}$ (0 µM, 1 µM, 5 µM, 10 µM). Following treatment, cells were stained with Hoechst 33342 for 30–60 min based on previously published methods[36]. For each group, 3–4 randomly selected fields were imaged using a Zeiss fluorescence microscope (×20 objective), acquiring phase contrast and Hoechst fluorescence channel images. Condensed (apoptotic) and diffuse (healthy) nuclei were counted using ImageJ software. The TUNEL assay was performed according to the manufacturer's protocol (Beyotime, catalog no. C1088). All data represent three biological replicates, and both image quantification and data analysis were performed by operators blinded to the experimental groups.

RNA-seq. Total RNA extraction was performed using hippocampal tissues from WT, 5xFAD, 5xFAD;$Ulk1^{OV}$ and $Ulk1^{OV}$ mice. Agarose gel electrophoresis was done to check for RNA integrity and DNA contamination; RNA purity (as well as concentration) was checked using a NanoPhotometer spectrophotometer (IMPLEN) and Bioanalyzer 2100 system (Agilent Technologies). Then, cDNA libraries were constructed using ≥800 ng RNA per sample with Illumina's NEBNext UltraTM RNA Library Prep Kit following the manufacturer's recommendations. The effective concentration of the library was determined to be at least 2 nM. Next-generation sequencing data (performed by the company Novogene) were obtained and analyzed. FastQC and trim galore were used to filter raw sequence data and for the removal of adapters, N-containing reads and low-quality reads (reads below Q20). Transcriptome analysis was performed using raw counts processed through DESeq2 (v1.16.1) to identify DEGs across WT, 5xFAD, 5xFAD;$Ulk1^{OV}$ and $Ulk1^{OV}$ mice ($n = 3$ per group). Principal component analysis was conducted on normalized count data to visualize sample clustering and assess overall transcriptomic differences between experimental groups. Volcano plots were generated to visualize the distribution of DEGs, with the *x*axis representing $\log_2$(fold change) and the *y*axis showing $-\log_{10}$(adjusted *P*value (P_{adj})), allowing for simultaneous visualization of statistical significance and magnitude of expression changes. Genes with $P_{adj} < 0.05$ and $|\log_2(\text{fold change})| > 0.5$ were designated as DEGs. Mean fragments per kilobase million values of DEGs from each group were normalized using the mfuzz R package and subjected to fuzzy *c*-means clustering, generating eight distinct expression pattern clusters. Functional enrichment analysis was conducted using clusterProfiler (v4.0) to perform GO enrichment analysis (covering the biological process, cellular component and molecular function categories) and KEGG pathway analysis on genes within each cluster. The Benjamini–Hochberg method was applied for *P*-value adjustment, with terms having $P_{adj} < 0.05$ considered significantly enriched.

Golgi staining. Fresh mouse brain hemispheres were processed for Golgi staining according to the manufacturer's protocol (FD Rapid Golgi stain kit, catalog no. PK401A, FD Neuro Technologies). Briefly,

ten-month-old WT, 5xFAD, 5xFAD;Ulk1^{OV} and Ulk1^{OV} mice were anesthetized and decapitated with the brain quickly removed from the skull; brain hemispheres were immersed in A + B solution for 2 weeks in the dark at room temperature, transferred to C solution for 1 week and sectioned at 150 µm in C solution using a vibratome. Sections were washed in water (2 × 4 min), stained with D + E solution for 10 min, washed again (2 × 4 min), dehydrated through a graded ethanol series (50%, 75%, 95%, 100%; 4 min each), cleared in xylene (3 × 4 min) and mounted with resin. Images were taken in bright field using a ×63 oil objective and further analyzed with Neurolucida software (MBF Bioscience)[37,91,92]. Spine density was analyzed with ImageJ software. At least 60 dendrites (longer than 10 µm and from a total of four mice) per group were counted; data were presented as numbers of spines per 10 µm. The experiments were processed in a double-blind manner.

AAV injection in mice. The mice were anesthetized (Avertin, 10 µl g^{-1}, intraperitoneal) and placed in a stereotaxic instrument (RWD). A heat pad was used to hold body temperature at 37 °C. A small craniotomy hole was made using a dental drill (OmniDrill35, WPI), and injections were performed via a micropipette connected to a Nanoliter Injector (NANOLITER 2010, WPI) and its controller (Micro4, WPI) at a slow flow rate of 0.1 µl min^{-1} to avoid potential damage to local brain tissue. AAV2/9-CMV-Ulk1-3*flag-WPRE-pA, AAV2/9-U6-shRNA (Ulk-1)-CMV-EGFP-pA or AAV2/9-U6-shRNA (Scram)-CMV-EGFP-pA was injected into the hippocampal CA1 region of WT and 5xFAD mice (virus titers: 2.0 × 1,012 genome copies ml^{-1}, 1 µl per injection; AP: −2.2 mm; ML: ±2.0 mm; DV: −2.0 mm). Following injection, the micropipette was left in place for approximately 10 min and then extracted slowly (over approximately 1 min to completely move the micropipette from the injection site to the surface of the brain) to minimize virus leakage in the track. The wound was stitched, antibiotics (bacitracin and neomycin) were applied to the surgical wound, and ketoprofen (5 mg kg^{-1}) was injected subcutaneously. The animals were allowed to recover from anesthesia under a heat lamp.

NOL and NOR tests. For NOL and NOR tests, mice were acclimated to the arena (empty plastic box, 40 cm × 40 cm × 40 cm, ~15 lux, 21 °C) for 10 min per day over 3 consecutive days. During training, three distinct objects were placed in three corners (8 cm from walls)[93], and mice were allowed to explore them for 10 min per trial across three trials, with 10-min intertrial intervals. Memory was assessed 24 h later. For NOL testing, one object was moved to the diagonal corner; exploration time at the new location was recorded as a percentage. For NOR testing, one familiar object was replaced with a new object, while positions remained unchanged; exploration time of the new object was calculated as a percentage. Between all sessions, the arena and objects were cleaned with 75% ethanol, wiped dry and allowed to air dry thoroughly to eliminate olfactory cues.

MWM test. The MWM test was conducted to evaluate spatial learning and memory[76]. The apparatus consisted of a black circular pool (120 cm diameter, 50 cm height) filled with opaque water (21 ± 2 °C, depth 40 cm). Four distinct visual cues (geometric shapes and high-contrast patterns) were fixed equidistantly on the inner walls and remained unchanged throughout the experiment. The pool was divided into four quadrants, with a submerged platform (10 cm diameter, 1.5 cm below water surface) placed in the third (target) quadrant. During training (seven consecutive days, three trials per day with 60-s intervals), mice were released from the midpoint of one of three non-target quadrants, facing the wall and allowed 60 s to locate the hidden platform. If successful, they remained on it for 15 s; otherwise, they were guided onto the platform and stayed for 15 s. A probe trial was performed 24 h after training with the platform removed. Mice were released from the quadrant opposite the original platform location. Time to the former platform site, platform-crossing frequency, swimming speed and distance were recorded by video and analyzed using EthoVision XT software. Room temperature (21 ± 1 °C), humidity (60–80%) and all environmental objects were kept constant.

Y-maze test. Spontaneous alternation was assessed using a symmetrical white plastic Y-maze (arms 50 cm × 10 cm × 20 cm). Between trials, the arms were cleaned with 75% ethanol, wiped dry and left for at least 5 min to allow ethanol evaporation. Mice were placed in the center and allowed to explore freely for 10 min. Arm entries (defined as all four paws entering an arm) were recorded. Percentage alternation was calculated as [number of triads containing all three arms/(total arm entries − 2)] × 100.

Grip strength. Forelimb grip strength of WT, 5xFAD, 5xFAD;Ulk1^{OV} and Ulk1^{OV} mice was assessed using a grip strength meter, with the procedure described as follows[94]: Forelimb grip strength was assessed using a grip strength meter as previously described[95]. Mice were suspended by the tail and lowered onto the pull bar, allowing only the forepaws to grasp the apparatus. The mouse was pulled backward steadily in a horizontal plane until the grip was released. Trials where hind paws contacted the bar were excluded. Each mouse underwent three trials, with an intertrial interval of at least 15 min, and the average force was calculated. To control for body mass variations, body weight was treated as a covariate in the statistical analysis.

Metabolic assessment. The metabolic rates of WT, 5xFAD, 5xFAD;Ulk1^{OV} and Ulk1^{OV} mice were evaluated using indirect calorimetry in open-circuit Oxymax chambers with CLAMS (Columbus Instruments), as described previously[96]. Briefly, mice (6.5 months old; n = 5–6 per group) were singly housed at 24 °C under a 12:12-h light–dark cycle (07:00–19:00) with ad libitum access to food and water. Following a 3–6 h acclimatization period, metabolic data were recorded over a 24-h cycle. The system was calibrated using standard gas mixtures and operated with a constant airflow of 0.6 l min^{-1}. Measurements were sampled for 30 s at 30-min intervals.

Body composition. Unanesthetized WT, 5xFAD, 5xFAD;Ulk1^{OV} and Ulk1^{OV} mice were placed in the transparent plastic tube of the Niumag Corporation Small Animal Body Composition Analyzer. This instrument is based on quantitative nuclear magnetic resonance technology[97]. Body fat, free body fluid and lean tissue content were quantified by exploiting tissue-specific differences in proton content and relaxation times (T1 and T2).

Primary microglia and astrocyte culture. We isolated microglia and astrocytes from a mixed primary glial cell culture system (including astrocytes and microglia) extracted from cerebral cortices of 1-day post-neonatal mice. The mouse cortices were carefully separated from meninges, minced and digested with 0.25% trypsin. After dissociation and passage through a 75-µm nylon cell strainer and centrifugation at 300g for 3 min, cells were resuspended in Dulbecco's Modified Eagle Medium/Nutrient Mixture F-12 (DMEM/F12) supplemented with 10% fetal bovine serum (FBS) and plated in T75 poly-D-lysine-coated flasks at 10 million cells per flask. The cultures were kept at 37 °C in 5% CO_2 with medium changes every 2–3 days. Approximately 30 days after plating, microglia and astrocytes were separated via the following methods: cultures were shaken at 230 rpm at 37 °C for 4–6 h, the medium (containing microglia) was collected and centrifuged at 300 g for 5 min, and cell pellets were resuspended and plated in 24-well poly-D-lysine-coated microtiter plates. The remaining cells in the T75 poly-D-lysine-coated flask were primary astrocytes and were harvested using 0.25% trypsin. The purity of astrocytes and microglia was checked by staining the cells with GFAP antibody and Iba1 antibody, respectively.

Culture of primary neurons. Primary neuronal cultures were prepared from cerebral cortices of embryonic day-16 mice[98]. The mouse brain was taken out carefully and soaked in D-Hank's solution (8.0 g NaCl, 0.4 g KCl, 0.13 g $Na_2HPO_4{\cdot}12H_2O$, 0.06 g KH_2PO_4, 0.35 g $NaHCO_3$, 1 l deionized water). Then, the cerebral cortex was separated and minced with scissors for 1 min and dissociated into a single-cell suspension using 0.125% trypsin digestion for 20 min. Digestion was terminated by DMEM/F12 supplemented with 10% (v/v) FBS. After dissociation and passage through a 75-µm nylon cell strainer, cells were centrifuged at 300 g for 3 min, resuspended at the desired density and seeded on glass coverslips coated with Poly-L-Lysine. After 4 h, the medium was replaced with Neurobasal medium containing 2% B27 and 1% penicillin/streptomycin (P&S). The medium was diluted with 50% fresh medium on day 3, and this procedure was repeated every 3 days until the day of the experiments.

Western blotting. Western blots were performed as described previously[91,95,99]. Mouse brain tissue was homogenized in radioimmunoprecipitation assay buffer (Cell Signaling Technology, catalog no. 9806S) supplemented with protease and phosphatase inhibitors (Bimake, catalog nos. B14002 and B15002), followed by sonication. After centrifugation at 12,000*g* at 4 °C for 30 min, the supernatant was collected, and the protein concentration was determined using a bicinchoninic acid assay. Equal amounts of protein were then denatured with loading dye at 95 °C for 5 min, separated on 4–12% sodium dodecyl sulfate–polyacrylamide gel electrophoresis gels and transferred to polyvinylidene fluoride membranes (Bio-Rad). Membranes were blocked with 3% bovine serum albumin in tris-buffered saline with Tween-20 and incubated with primary and HRP-conjugated secondary antibodies. Signals were detected by chemiluminescence using a ChemiDoc MP system (Bio-Rad) and analyzed with ImageJ. The following primary antibodies were used: Rabbit polyclonal anti-ULK1 antibody (1:1,000, Sigma, catalog no. A7481); Rabbit monoclonal anti-ULK1 antibody (1:1,000, Cell Signaling Technology, catalog no. 6439); Rabbit monoclonal anti-TAU antibody (1:1,000, Abcam, catalog no. ab254256); Rabbit monoclonal anti-LC3B antibody (1:1,000, Cell Signaling Technology, catalog no. 43566); Mouse monoclonal anti-β-Amyloid antibody (1:500, Biolegend, catalog no. 803008); Rabbit monoclonal anti-APP antibody (1:1,000, Cell Signaling Technology, catalog no. 2452S); Rabbit polyclonal anti-APP-CTFs antibody (1:500, Invitrogen, catalog no. CT695); Rabbit monoclonal anti-ambra1 antibody (1:1,000, Cell Signaling Technology, catalog no. 24907); Rabbit monoclonal anti-Pink1 antibody (1:1,000, Cell Signaling Technology, catalog no. 6946T); Rabbit monoclonal anti-Parkin antibody (1:1,000, Cell Signaling Technology, catalog no. 4211S); Rabbit monoclonal anti-Beclin antibody (1:1,000, Cell Signaling Technology, catalog no. 3495); Rabbit monoclonal anti-NIX antibody (1:1,000, Cell Signaling Technology, catalog no. 12396S); Mouse monoclonal anti-SirT1 antibody (1:500, Cell Signaling Technology, catalog no. 8469); Rabbit monoclonal anti-Cathepsin B antibody (1:500, Invitrogen, catalog no. MAB30458); Rabbit polyclonal phospho-Tau (Thr231) antibody (1:1,000, Cell Signaling Technology, catalog no. 71429); Rabbit polyclonal phospho-Tau (Thr181) antibody (1:1,000, Cell Signaling Technology, catalog no. 12885S); Rabbit polyclonal phospho-Tau (Thr217) antibody (1:1,000, Invitrogen, catalog no. 44-744); Rabbit monoclonal phospho-Tau (Ser396) antibody (1:1,000, Invitrogen, catalog no. MA5-41154); Rabbit polyclonal phospho-Tau (Ser404) antibody (1:1,000, Cell Signaling Technology, catalog no. 70194S); Rabbit polyclonal phospho-Tau (Ser199) antibody (1:1,000, Cell Signaling Technology, catalog no. 29957); Rabbit monoclonal anti-Tau antibody (1:1,000, Cell Signaling Technology, catalog no. 46687s); Mouse monoclonal anti-ac-tauK174 (1:250, Gan lab, Cornell); Rabbit monoclonal anti-ac-tauK274 (1:500, Gan lab, Cornell); Rabbit monoclonal anti-ac-tauK281 (1:500, Gan lab, Cornell); Rabbit monoclonal anti-actin antibody (1:2,000, Cell Signaling Technology, catalog no. 3700); Rabbit monoclonal anti-GSK3 antibody (1:1,000, Cell Signaling Technology, catalog no. 5676); Rabbit monoclonal anti-Atg5 antibody (1:1,000, Cell Signaling Technology, catalog no. 12994); Rabbit polyclonal anti-ULK2 antibody (1:1,000, Abcam, catalog no. ab97695); Rabbit monoclonal anti-Fundc1 antibody (1:1,000, Cell Signaling Technology, catalog no. 49240); Rabbit monoclonal anti-BNIP3 antibody (1:1,000, Cell Signaling Technology, catalog no. 44060S); Rabbit monoclonal anti-gapdh antibody (1:1,000, Cell Signaling Technology, catalog no. 5174); Rabbit monoclonal anti-p-mTOR antibody (1:1,000, Cell Signaling Technology, catalog no. 2971s); Rabbit monoclonal anti-mTOR antibody (1:1,000, Abcam, catalog no. ab109268); Rabbit monoclonal anti-p-AMPK antibody (1:1,000, Cell Signaling Technology, catalog no. 2535s); Rabbit monoclonal anti-AMPK antibody (1:1,000, Cell Signaling Technology, catalog no. 5831s); Mouse monoclonal anti-COX2 antibody (1:500, Santa Cruz, catalog no. sc-514489). Secondary antibodies were anti-mouse immunoglobulin G (1:10,000, Cell Signaling Technology, catalog no. 7060) and anti-rabbit IgG (1:10,000, Invitrogen, catalog no. 31460), both from GE Healthcare.

ELISA for $A\beta_{1\text{-}40}$ and $A\beta_{1\text{-}42}$. Mouse hippocampal and cortical extracts were prepared as reported previously[100]. In brief, brain tissue from different groups was extracted, and the cortices were dissected and homogenized in eight volumes of ice-cold TBS containing 5 mM EDTA, phosphatase inhibitor, EDT-free protease inhibitor cocktail (Roche) and 2 mM 1,10-phenantroline (Sigma). Homogenates were centrifuged at 100,000*g* for 1 h at 4 °C using an Optima TL ultracentrifuge and a Ti70 rotor (Beckman Coulter). Supernatants were collected, and cell pellets were homogenized in 70% formic acid. Samples were centrifuged at 100,000*g* for 1 h at 4 °C, and supernatants were collected. FA-containing supernatants were neutralized with 1 M Tris-base, pH 11 (1:20 v/v), and samples were used to measure FA-soluble Aβ. ELISA assays were performed using Aβ ELISA kits (Wako catalog nos. 292-64501 and 294-62501).

Immunofluorescence using mouse tissue. As described earlier[11,37], anesthetized mice were perfused with normal saline and 4% paraformaldehyde in PBS. The collected brains were fixed in 4% paraformaldehyde overnight at 4 °C and then equilibrated in 30% sucrose for 24 h. Brain tissues were cut into 30-µm coronal slices. The sections in 1:6 series equidistant floating (180-µm interval) from each mouse were incubated in blocking buffer (10% donkey serum and 0.3% Triton X-100 in PBS) for 30 min at room temperature. Samples were incubated with the primary antibodies (Rabbit polyclonal anti-ULK1 antibody (1:500, Sigma, catalog no. A7481); Mouse monoclonal anti-Map2 (1:100, Sigma, catalog no. MAB3418); Rabbit monoclonal anti-TAU antibody (1:200, Abcam, catalog no. ab254256); Mouse monoclonal anti-β-Amyloid antibody (1:250, Biolegend, catalog no. 803008); Rabbit polyclonal anti-IBA1 antibody (1:500, FUJIFILM Wako Pure, catalog no. 019-19741); Mouse monoclonal anti-COX2 antibody (1:250, Santa Cruz, catalog no. sc-514489); Rabbit monoclonal anti-Cathepsin B antibody (1:200, Invitrogen, catalog no. MAB30458); Mouse monoclonal anti-AT8 antibody (1:500, Invitrogen, catalog no. MN1020B); ac-Tau174 (1:250, Gan lab, Cornell); Rabbit monoclonal anti-NeuN antibody (1:500, Abcam, catalog no. ab177487); Rabbit polyclonal anti-GFAP antibody (1:500, Abcam, catalog no. ab116010)) overnight at 4 °C and then probed with a appropriate fluorescent probe-conjugated secondary antibody (Donkey Anti-Rabbit IgG H&L (Alexa Fluor 488) (1:1,000, Abcam, catalog no. ab150073); Donkey Anti-Rabbit IgG H&L (Alexa Fluor 594) (1:1,000, Abcam, catalog no. ab150076); Donkey Anti-Mouse IgG H&L (Alexa Fluor 488) (1:1,000, Abcam, catalog no. ab150105); Donkey Anti-Mouse IgG H&L (Alexa Fluor 594) (1:1,000, Abcam, catalog no. ab150108) Goat Anti-Mouse IgG H&L (Alexa Fluor 488) (1:1,000, Invitrogen, catalog no. a-11001); Goat Anti-Rabbit IgG H&L (Alexa Fluor 546) (1:1,000, Invitrogen, catalog no. A10040)) for 1 h at room temperature while protected from light. Nuclei were stained with DAPI at 1:5,000. Images were obtained with an Axiovert 200 M microscope (ZEISS) or a confocal microscope (Leica).

Electron microscopy. HIP, EC and PFC tissues from WT, 5xFAD, 5xFAD;Ulk1^{OV} and Ulk1^{OV} mice were processed for transmission electron microscopy with minor modifications to established protocols[76,101]. Tissues were cut into small pieces (<1 mm), fixed in Trump's fixative for 2 h at room temperature, washed in 0.1 M cacodylate buffer, post-fixed in 1% osmium tetroxide, dehydrated through graded ethanol, embedded in an EMbed 812 kit (Electron Microscopy Sciences) and imaged on a JEOL 1200EX microscope. For quantitative studies, the percentages of damaged mitochondria (number of damaged mitochondria per total mitochondria; here damaged mitochondria are morphologically damaged, such as showing incompleteness of mitochondrial membrane and loss of mitochondrial cristae) and mitophagy-like events (including mitophagy at different stages) were counted[99]. Neurons and microglia were identified by ultrastructural features[102]. Analyses focused on neuronal mitochondria; data collection and statistical analyses were performed blinded.

ATP detection. ATP concentrations in whole brains from WT, 5xFAD, 5xFAD;Ulk1^{OV} and Ulk1^{OV} mice were determined using a commercial ATP Assay Kit (MedChemExpress, catalog no. HY-K0314) following the manufacturer's protocol. Briefly, tissue samples were homogenized in ice-cold lysis buffer and centrifuged (12,000*g*, 20 min, 4 °C) to collect supernatants. ATP levels were determined using a 0–10 µM standard curve; standards and samples were assayed in triplicate in 96-well plates, incubated with detection reagent for 10 min at room temperature with gentle shaking and read for luminescence on a BioTek Cytation 5 (1 s per well). ATP concentrations were calculated from the standard curve with blank controls, and experiments were repeated three times independently.

Mitophagy assay in primary cortical neurons. Primary cortical neurons were cultured from postnatal day-0 mouse brains and maintained in Neurobasal medium supplemented with 2% B27 and 1% GlutaMAX. At 8 days in vitro, mitophagy was assessed using a commercially available Mitophagy Detection Kit (Dojindo, catalog no. MD01) according to the manufacturer's instructions. Briefly, neurons were incubated with the mitophagy dye (100 nM) in prewarmed culture medium at 37 °C for 30 min. The cells were then washed twice with fresh medium and imaged using a confocal microscope (Zeiss LSM880). The mitophagy index was calculated using ImageJ software.

Effect ULK1 activators and inhibitors on mitophagy in cell line culture. HeLa cells expressing YFP-tagged Parkin and mt-Keima (YPH-mtKeima) were a generous gift from H.-M. Shen, National University of Singapore[103]. The YPH-mtKeima cells were grown in DMEM under normal conditions. For experiments, 80,000 cells were seeded on Ibidi dishes in 2 ml normal growth medium. The cells were allowed to attach to the plates overnight and then treated for 24 h with ULK1 activators (Rac-BL-918, MCE, catalog no. HY-124729A; LYN-1604 dihydrochloride, MCE, catalog no. HY-101923B) or inhibitors (SBI-0206965, MCE, catalog no. HY-16966; XST-14, MCE, catalog no. HY-137506) at doses of 0.5, 5 µM for Rac. 2, 4 µM for LYN; 5, 10 µM for SBI; 2.5, 5 µM for XST for 24 h, respectively. Three hours before imaging, 20 µM CCCP was added as a positive control for mitophagy activation. Cells were imaged live under a Zeiss LSM720 confocal microscope. Quantification was performed with ImageJ software, and the ratio of the mean fluorescence intensities was calculated[104]. Five images were taken per biological repeat. Data were pooled from three biological repeats.

In vitro tau seeding assay in HEK293 cells. HEK293 cells expressing P301S tau-Venus were used for 'tau seeding' assays as previously described[23,105], with some modifications. In brief, tau seed-lipid (Lipofectamine 2000) complex (20 nM) transfected cells were cultured at 37 °C for 2 h before addition of an equal volume of 2× working solution of each drug (1, 10 µM for Rac; 4, 8 µM for LYN; 10, 20 µM for SBI; 5, 10 µM for XST, respectively) in DMEM (with 20% FBS and 2% P&S) followed by incubation for 48 h. Alternatively, tau seed-lipid complex (20 nM) transfected cells were cultured in a 37 °C CO_2 incubator for 2 h. A equal volume of DMEM-20% FBS was added followed by incubation for 48 h. Media were removed and replaced with 1× working solution of each drug (0.5, 5 µM for Rac; 2, 4 µM for LYN; 5, 10 µM for SBI; 2.5, 5 µM for XST, respectively) in DMEM (with 10% FBS and 1% P&S), and cells were incubated for 48 h. Cells were then rinsed with PBS, fixed with fresh 4% (mass/vol) formaldehyde solution (Sigma Aldrich) and stained with DAPI (Sigma Aldrich) at 1 µg ml^{-1} in PBS. Images were taken using a ×20 objective lens on a Nikon inverted fluorescence microscope equipped with a DS-Fi3 camera. Cells, nuclei and tau-Venus aggregates were detected and GFP intensity quantified using ImageJ software. Two to three images per well were taken with a total of 12 to 18 images per biological repeat. Data were pooled from three biological repeats.

Lentivirus packaging and transductions. To perform related overexpression or KD experiments, lentivirus was packaged in HEK293 cells using standard protocols for second-generation packaging. Cells were then incubated for 48 h after transfection, and the lentivirus-containing medium was filtered using 0.45-µm polyethersulfone membranes (or centrifuged at 300 g for 5 min) to remove cellular debris. The filtered lentiviral supernatants were added to HEK293 P301S tau-Venus cells along with 4 µg ml^{-1} polybrene. The cell–virus mixture was centrifuged at 1,000*g* for 2 h. Following centrifugation, the cells were resuspended in fresh medium and allowed to expand for 48 h before proceeding with the selection process.

siRNA transfection. HEK293 P301S tau-Venus cells were transiently transfected with different siRNA materials together with Lipofectamine RNAiMAX (catalog no. 13778150, Invitrogen, ThermoFisher) to increase transfection efficiency; the experiments were performed according to the protocol provided by the manufacturer. The siRNA reagents used including siRNA targeting ULK1 (catalog no. SR322391, OriGene), PINK1 (catalog no. SR324912, OriGene), Parkin (catalog no. SR321228, OriGene), FUNDC1 (catalog no. SR315322, OriGene), Ambra1 (catalog no. SR310808, OriGene), BNIP3 (catalog no. SR300461, OriGene), BNIP3L/NIX (catalog no. SR300462, OriGene), GSK3-beta (catalog no. SR301979, OriGene), ULK2 (catalog no. SC-44183, Santa Cruz Biotechnology), Atg5 (catalog no. SR322789, OriGene), Beclin1 (catalog no. SR322490, OriGene), Sirt1 (catalog no. SR323581, OriGene) or scramble control siRNA Oligo Duplexes at 100 nM. After 48 h of siRNA treatment, decent KD efficiency was achieved for each KD experiment (more than 90%, as validated by WB). Tau seeding experiments (as mentioned elsewhere) were performed 48 h after transfection.

***C. elegans* strains and maintenance.** The experiment was performed per our protocol reported elsewhere[23,99]. All strains were in the N2 WT background, EFF191 (N2$^{n\text{-}sid\text{-}1}$;unc-51$^{n\text{-}OV}$). The EFF029 (hTau[P301L]$^{n\text{-}sid\text{-}1OV}$) and EFF192 (hTau[P301L]$^{n\text{-}sid\text{-}1}$;unc-51$^{n\text{-}OV}$) *C. elegans* strains were obtained from the Fang lab. The TU3401 (N2$^{n\text{-}sid\text{-}1OV}$) was provided by the Rafal Ciosk lab. All strains are described in Supplementary Table 7. In brief, *C. elegans* strains were maintained at 20 °C on standard solid nematode growth medium (NGM) containing *Echerichia coli* OP50 (ref. 106). Gravid adults were isolated and bleached to obtain a synchronized population of worms[107] and then incubated until day 2 of adulthood; when needed, experimental worms were also collected through a 4–6-h egg lay by gravid adults to achieve synchronized age. For drug treatments, ULK1 activators and inhibitors were dissolved in dimethyl sulfoxide, added to fresh NGM plates, respectively, and administered to worms from late L4 stage onward.

RNA-mediated interference KD in *C. elegans*. N2 nematodes engineered for neuronal overexpression of *sid-1*[108] were used for RNA-mediated interference KD of *unc-51*, *pink-1* or *fndc-1*. Briefly,

dsRNA-expressing bacteria were grown on Luria–Bertani agar plates supplemented with ampicillin at 37 °C overnight, followed by inoculation of a bacterial colony into Luria–Bertani broth supplemented with ampicillin and overnight growth. Bacterial cultures were inoculated onto 1-day-old NGM plates containing 1 mM isopropyl β-D-1-thiogalactopyranoside and 100 μg ml^{-1} ampicillin and allowed to dry for 24 h or 48 h (ref. 109). Synchronized embryos obtained by bleaching were added to each RNA-mediated interference plate and incubated until day 2 of adulthood (or as specified elsewhere) for designated experiments. Bacteria carrying the empty L4440 vector were used as a vector control.

***C. elegans* short-term memory assay.** Chemotaxis assays were performed as described previously[23,57,76]. First, synchronized adult day-2 worms (200 worms per group) were collected and washed with M9 buffer to remove residual bacteria, followed by placement in plain 6-cm NGM plates (with no OP50) with/without IA for 90 min. A droplet of 10 μl IA was applied to the middle of the lid of the IA conditioning plate. Ten-cm assay plates were then prepared by adding 20 μl 20 mM NaN_3 to the 'IA' and 'T' ('trap') points, respectively. Plates were dried at 20–22 °C for 30 min prior to use. Each plate was covered with 50 mm × 50 mm parafilm. The worms were collected and washed with M9 buffer after the conditioning step and then placed on the 'S' point area ('start' point: location where all the worms being tested were loaded). On the 'IA' area, 5 μl 2% IA was applied to the parafilm. The worms were incubated at room temperature for 2 h. Worms in the 'S', 'IA' and 'T' regions were counted. The chemotaxis index (% CI) was calculated as follows: (#'IA' − #'T')/(#'IA' + #'T' + #'S'), with '#' denoting the number of worms[11,57,110]. A lower score indicates better performance. Data were from at least three biological replicates.

Statistics and reproducibility

Baseline statistical analyses were performed using IBM SPSS version 26 (IBM). In the descriptive analyses, parametric tests were used. Pearson's χ^2 was applied for the categorical variables. Student's *t*-test was used for the continuous variables, except for the Mann–Whitney *U* analysis used for serum ULK1, as it was highly skewed. Spearman's rho was used for bivariate correlation analyses. The CSF core biomarkers were analyzed in two different laboratories, preventing us from using them as continuous variables in the analyses including both patients and CU controls. Progression analyses were performed using Stata/IC 17.0 (StataCorp LLC). We applied a linear mixed-effects regression model to test the interaction of CSF ULK1 × time on CDR-SB scores. The dependent variable was thus CDR-SB. The fixed effects included CSF ULK1 × time + CSF $A\beta_{1\text{-}42}$ × time + CSF p-tau_{181} × time + CSF ULK1 + CSF $A\beta_{1\text{-}42}$ + CSF p-tau_{181} + clinical syndrome (MCI or dementia) + age + sex + years of education. Random effects included time and intercept. The variable time was defined as the follow-up duration of the CDR scorings in years. The interaction of CSF $A\beta_{1\text{-}42}$ and p-tau_{181} with time (CSF $A\beta_{1\text{-}42}$ × time and CSF p-tau_{181} × time) were included in addition to the simple main effects of these variable because we were interested in whether higher concentrations of CSF ULK1 relative to AD pathology is favorable. We further calculated plots of predictive margins using margins and marginsplot. For other data, GraphPad Prism 9 software was used for statistical analysis of experimental data, and results are presented as mean ± s.e.m. unless otherwise specified. We performed a minimum of three independent biological trials for each wet-lab experiment. The details of biological replicates are in the figure legends. Values of $P < 0.05$ were considered significant. All sample populations were first assessed for normality. Two-tailed unpaired Student's *t*-tests were used for comparisons between two groups. Group differences were analyzed with one-way analysis of variance (ANOVA) followed by Šidák's multiple-comparisons test or two-way ANOVA followed by Tukey's or Dunnett's multiple-comparisons test for multiple groups when data were determined to be normally distributed; otherwise, data were analyzed via the Mann–Whitney *U* test or the Kruskal–Wallis test. Outlier handling was performed in consultation with UiO/Ahus statistical departments and was based on established protocols[111–113]; no data were excluded from the analyses. No statistical methods were used to predetermine sample sizes, but our sample sizes are similar to those reported in previous publications[82,83]. To eliminate subjectivity, we have specified that both the investigators administering the treatment and those assessing the outcomes were blinded to the group allocation. Samples were allocated to experimental groups according to genotypes or treatments. No method of randomization was used to assign samples to experimental groups.

Reporting summary

Further information on research design is available in the Nature Portfolio Reporting Summary linked to this article.

Data availability

RNA-seq data are available at the Gene Expression Omnibus (GEO) under accession code GSE263411. All data supporting the findings of this study are available from the corresponding authors upon request. Source data are provided with this paper.

References

1. Scheltens, P. et al. Alzheimer's disease. *Lancet* **388**, 505–517 (2016).
2. Hardy, J. & Selkoe, D. J. The amyloid hypothesis of Alzheimer's disease: progress and problems on the road to therapeutics. *Science* **297**, 353–356 (2002).
3. Braak, H. & Braak, E. Neuropathological stageing of Alzheimer-related changes. *Acta Neuropathol.* **82**, 239–259 (1991).
4. Lautrup, S., Sinclair, D. A., Mattson, M. P. & Fang, E. F. NAD+ in brain aging and neurodegenerative disorders. *Cell Metab.* **30**, 630–655 (2019).
5. Masters, C. L. et al. Alzheimer's disease. *Nat. Rev. Dis. Prim.* **1**, 1–18 (2015).
6. Morris, M., Maeda, S., Vossel, K. & Mucke, L. The many faces of tau. *Neuron* **70**, 410–426 (2011).
7. Kunkle, B. W. et al. Genetic meta-analysis of diagnosed Alzheimer's disease identifies new risk loci and implicates Aβ, tau, immunity and lipid processing. *Nat. Genet.* **51**, 414–430 (2019).
8. Aman, Y. et al. Autophagy in healthy aging and disease. *Nat. Aging* **1**, 634–650 (2021).
9. Fleming, A. et al. The different autophagy degradation pathways and neurodegeneration. *Neuron* **110**, 935–966 (2022).
10. Reeves, B. C. et al. Glymphatic system impairment in Alzheimer's disease and idiopathic normal pressure hydrocephalus. *Trends Mol. Med.* **26**, 285–295 (2020).
11. Fang, E. F. et al. Mitophagy inhibits amyloid-beta and tau pathology and reverses cognitive deficits in models of Alzheimer's disease. *Nat. Neurosci.* **22**, 401–412 (2019).
12. Lou, G. et al. Mitophagy and neuroprotection. *Trends Mol. Med.* **26**, 8–20 (2019).
13. Wilson, D. M. et al. Hallmarks of neurodegenerative diseases. *Cell* **186**, 693–714 (2023).
14. Lopez-Otin, C., Blasco, M. A., Partridge, L., Serrano, M. & Kroemer, G. Hallmarks of aging: an expanding universe. *Cell* **186**, 243–278 (2023).
15. Kobro-Flatmoen, A. et al. Re-emphasizing early Alzheimer's disease pathology starting in select entorhinal neurons, with a special focus on mitophagy. *Ageing Res. Rev.* **67**, 101307 (2021).
16. Lee, J. H. et al. Faulty autolysosome acidification in Alzheimer's disease mouse models induces autophagic build-up of Abeta in neurons, yielding senile plaques. *Nat. Neurosci.* **25**, 688–701 (2022).

17. Cummins, N., Tweedie, A., Zuryn, S., Bertran-Gonzalez, J. & Gotz, J. Disease-associated tau impairs mitophagy by inhibiting Parkin translocation to mitochondria. *EMBO J.* **38**, e99360 (2018).
18. Bourdenx, M. et al. Chaperone-mediated autophagy prevents collapse of the neuronal metastable proteome. *Cell* **184**, 2696–2714 (2021).
19. Kerr, J. S. et al. Mitophagy and Alzheimer's disease: cellular and molecular mechanisms. *Trends Neurosci.* **40**, 151–166 (2017).
20. Hou, Y. et al. NAD(+) supplementation reduces neuroinflammation and cell senescence in a transgenic mouse model of Alzheimer's disease via cGAS-STING. *Proc. Natl Acad. Sci. USA* **118**, e2011226118 (2021).
21. Gulen, M. F. et al. cGAS-STING drives ageing-related inflammation and neurodegeneration. *Nature* **620**, 374–380 (2023).
22. Fairley, L. H. et al. Mitochondrial control of microglial phagocytosis by the translocator protein and hexokinase 2 in Alzheimer's disease. *Proc. Natl Acad. Sci. USA* **120**, e2209177120 (2023).
23. Xie, C. et al. Amelioration of Alzheimer's disease pathology by mitophagy inducers identified via machine learning and a cross-species workflow. *Nat. Biomed. Eng.* **6**, 76–93 (2022).
24. Rocchi, A. et al. A Becn1 mutation mediates hyperactive autophagic sequestration of amyloid oligomers and improved cognition in Alzheimer's disease. *PLoS Genet.* **13**, e1006962 (2017).
25. Lee, J. H. et al. Lysosomal proteolysis and autophagy require presenilin 1 and are disrupted by Alzheimer-related PS1 mutations. *Cell* **141**, 1146–1158 (2010).
26. Fu, H. et al. A tau homeostasis signature is linked with the cellular and regional vulnerability of excitatory neurons to tau pathology. *Nat. Neurosci.* **22**, 47–56 (2019).
27. Heckmann, B. L. et al. Noncanonical function of an autophagy protein prevents spontaneous Alzheimer's disease. *Sci. Adv.* **6**, eabb9036 (2020).
28. Mizushima, N. The role of the Atg1/ULK1 complex in autophagy regulation. *Curr. Opin. Cell Biol.* **22**, 132–139 (2010).
29. Lazarou, M. et al. The ubiquitin kinase PINK1 recruits autophagy receptors to induce mitophagy. *Nature* **524**, 309–314 (2015).
30. Zachari, M. & Ganley, I. G. The mammalian ULK1 complex and autophagy initiation. *Essays Biochem.* **61**, 585–596 (2017).
31. Wu, W. et al. ULK 1 translocates to mitochondria and phosphorylates FUNDC 1 to regulate mitophagy. *EMBO Rep.* **15**, 566–575 (2014).
32. Cai, Y. et al. Comparing machine learning-derived MRI-based and blood-based neurodegeneration biomarkers in predicting syndromal conversion in early AD. *Alzheimers Dement.* **19**, 4987–4998 (2023).
33. Shi, L. et al. Multiomics profiling of human plasma and cerebrospinal fluid reveals ATN-derived networks and highlights causal links in Alzheimer's disease. *Alzheimers Dement.* **19**, 3350–3364 (2023).
34. Mathys, H. et al. Single-cell transcriptomic analysis of Alzheimer's disease. *Nature* **570**, 332–337 (2019).
35. Knapskog, A. B. et al. Higher concentrations of kynurenic acid in CSF are associated with the slower clinical progression of Alzheimer's disease. *Alzheimers Dement.* **19**, 5573–5582 (2023).
36. Cheng, A. et al. Mitochondrial SIRT3 mediates adaptive responses of neurons to exercise and metabolic and excitatory challenges. *Cell Metab.* **23**, 128–142 (2016).
37. Li, C. & Götz, J. Somatodendritic accumulation of tau in Alzheimer's disease is promoted by Fyn-mediated local protein translation. *EMBO J.* **36**, 3120–3138 (2017).
38. Xiong, J. et al. FSH blockade improves cognition in mice with Alzheimer's disease. *Nature* **603**, 470–476 (2022).
39. McAlpine, C. S. et al. Astrocytic interleukin-3 programs microglia and limits Alzheimer's disease. *Nature* **595**, 701–706 (2021).
40. Eimer, W. A. & Vassar, R. Neuron loss in the 5XFAD mouse model of Alzheimer's disease correlates with intraneuronal Abeta42 accumulation and Caspase-3 activation. *Mol. Neurodegener.* **8**, 2 (2013).
41. Pluvinage, J. V. & Wyss-Coray, T. Systemic factors as mediators of brain homeostasis, ageing and neurodegeneration. *Nat. Rev. Neurosci.* **21**, 93–102 (2020).
42. Berriat, F., Lobsiger, C. S. & Boillée, S. The contribution of the peripheral immune system to neurodegeneration. *Nat. Neurosci.* **26**, 942–954 (2023).
43. Merlini, M. et al. Fibrinogen Induces microglia-mediated spine elimination and cognitive impairment in an Alzheimer's disease model. *Neuron* **101**, 1099–1108 (2019).
44. Egan, D. F. et al. Phosphorylation of ULK1 (hATG1) by AMP-activated protein kinase connects energy sensing to mitophagy. *Science* **331**, 456–461 (2011).
45. Allen, B. et al. Abundant tau filaments and nonapoptotic neurodegeneration in transgenic mice expressing human P301S tau protein. *J. Neurosci.* **22**, 9340–9351 (2002).
46. Palmqvist, S. et al. Discriminative accuracy of plasma phospho-tau217 for Alzheimer disease vs other neurodegenerative disorders. *JAMA* **324**, 772–781 (2020).
47. Tracy, T. E. et al. Acetylated tau obstructs KIBRA-mediated signaling in synaptic plasticity and promotes tauopathy-related memory loss. *Neuron* **90**, 245–260 (2016).
48. Min, S. W. et al. Critical role of acetylation in tau-mediated neurodegeneration and cognitive deficits. *Nat. Med.* **21**, 1154–1162 (2015).
49. Thijssen, E. H. et al. Plasma phosphorylated tau 217 and phosphorylated tau 181 as biomarkers in Alzheimer's disease and frontotemporal lobar degeneration: a retrospective diagnostic performance study. *Lancet Neurol.* **20**, 739–752 (2021).
50. Shin, M. K. et al. Reducing acetylated tau is neuroprotective in brain injury. *Cell* **184**, 2715–2732 (2021).
51. Mukadam, A. S. et al. Cytosolic antibody receptor TRIM21 is required for effective tau immunotherapy in mouse models. *Science* **379**, 1336–1341 (2023).
52. Ouyang, L. et al. Small-molecule activator of UNC-51-like kinase 1 (ULK1) that induces cytoprotective autophagy for Parkinson's disease treatment. *J. Med. Chem.* **61**, 2776–2792 (2018).
53. Zhang, L. et al. Discovery of a small molecule targeting ULK1-modulated cell death of triple negative breast cancer in vitro and in vivo. *Chem. Sci.* **8**, 2687–2701 (2017).
54. Lu, J. et al. Overexpression of ULK1 represents a potential diagnostic marker for clear cell renal carcinoma and the antitumor effects of SBI-0206965. *EBioMedicine* **34**, 85–93 (2018).
55. Xue, S. T. et al. The role of the key autophagy kinase ULK1 in hepatocellular carcinoma and its validation as a treatment target. *Autophagy* **16**, 1823–1837 (2020).
56. Lee, E. J. & Tournier, C. The requirement of uncoordinated 51-like kinase 1 (ULK1) and ULK2 in the regulation of autophagy. *Autophagy* **7**, 689–695 (2011).
57. Cao, S. Q., Wang, H. L., Palikaras, K., Tavernarakis, N. & Fang, E. F. Chemotaxis assay for evaluation of memory-like behavior in wild-type and Alzheimer's-disease-like *C. elegans* models. *STAR Protoc.* **4**, 102250 (2023).
58. Manolopoulos, A., Yao, P. J. & Kapogiannis, D. Extracellular vesicles: translational research and applications in neurology. *Nat. Rev. Neurol.* **21**, 265–282 (2025).
59. Melentijevic, I. et al. *C. elegans* neurons jettison protein aggregates and mitochondria under neurotoxic stress. *Nature* **542**, 367–371 (2017).

60. Russell, R. C. et al. ULK1 induces autophagy by phosphorylating Beclin-1 and activating VPS34 lipid kinase. *Nat. Cell Biol.* **15**, 741–750 (2013).
61. Fernandez, A. F. et al. Disruption of the beclin 1-BCL2 autophagy regulatory complex promotes longevity in mice. *Nature* **558**, 136–140 (2018).
62. Mary, A. et al. Hampered AMPK-ULK1 cascade in Alzheimer's disease (AD) instigates mitochondria dysfunctions and AD-related alterations which are alleviated by metformin. *Alzheimers Res. Ther.* **17**, 127 (2025).
63. Fu, H., Hardy, J. & Duff, K. E. Selective vulnerability in neurodegenerative diseases. *Nat. Neurosci.* **21**, 1350–1358 (2018).
64. Liu, C. C. et al. Cul3-KLHL20 ubiquitin ligase governs the turnover of ULK1 and VPS34 complexes to control autophagy termination. *Mol. Cell* **61**, 84–97 (2016).
65. Nazio, F. et al. Fine-tuning of ULK1 mRNA and protein levels is required for autophagy oscillation. *J. Cell Biol.* **215**, 841–856 (2016).
66. Wu, W. et al. ULK1 translocates to mitochondria and phosphorylates FUNDC1 to regulate mitophagy. *EMBO Rep.* **15**, 566–575 (2014).
67. Singh, R. & Cuervo, A. M. Autophagy in the cellular energetic balance. *Cell Metab.* **13**, 495–504 (2011).
68. Hu, Z. et al. ULK1 phosphorylation of striatin activates protein phosphatase 2A and autophagy. *Cell Rep.* **36**, 109762 (2021).
69. Hung, C. M. et al. AMPK/ULK1-mediated phosphorylation of Parkin ACT domain mediates an early step in mitophagy. *Sci. Adv.* **7**, eabg4544 (2021).
70. van Dyck, C. H. et al. Lecanemab in early Alzheimer's disease. *N. Engl. J. Med.* **388**, 9–21 (2023).
71. Mintun, M. A. et al. Donanemab in early Alzheimer's disease. *N. Engl. J. Med.* **384**, 1691–1704 (2021).
72. Canter, R. G., Penney, J. & Tsai, L. H. The road to restoring neural circuits for the treatment of Alzheimer's disease. *Nature* **539**, 187–196 (2016).
73. Goedert, M. Neurodegeneration. Alzheimer's and Parkinson's diseases: the prion concept in relation to assembled Abeta, tau, and alpha-synuclein. *Science* **349**, 1255555 (2015).
74. Herrup, K. The case for rejecting the amyloid cascade hypothesis. *Nat. Neurosci.* **18**, 794–799 (2015).
75. Lautrup, S., Sinclair, D. A., Mattson, M. P. & Fang, E. F. NAD(+) in brain aging and neurodegenerative disorders. *Cell Metab.* **30**, 630–655 (2019).
76. Fang, E. F. et al. Mitophagy inhibits amyloid-β and tau pathology and reverses cognitive deficits in models of Alzheimer's disease. *Nat. Neurosci.* **22**, 401–412 (2019).
77. Kingwell, K. Turning up mitophagy in Alzheimer disease. *Nat. Rev. Drug Discov.* **18**, 252 (2019).
78. Veverová, K. et al. Distinctive autophagy/mitophagy biomarker profiles in frontotemporal lobar degeneration and Alzheimer's disease. *Acta Neuropathol. Commun.* **13**, 37 (2025).
79. Veverová, K. et al. Alterations of human CSF and serum-based mitophagy biomarkers in the continuum of Alzheimer disease. *Autophagy* **20**, 1868–1878 (2024).
80. Longobardi, A. et al. Autophagy markers are altered in Alzheimer's disease, dementia with Lewy bodies and frontotemporal dementia. *Int. J. Mol. Sci.* **25**, 1125 (2024).
81. Braekhus, A., Ulstein, I., Wyller, T. B. & Engedal, K. The Memory Clinic-outpatient assessment when dementia is suspected. *Tidsskr. Nor. Laegeforen.* **131**, 2254–2257 (2011).
82. Albert, M. S. et al. The diagnosis of mild cognitive impairment due to Alzheimer's disease: recommendations from the National Institute on Aging-Alzheimer's Association workgroups on diagnostic guidelines for Alzheimer's disease. *Alzheimers. Dement.* **7**, 270–279 (2011).
83. McKhann, G. M. et al. The diagnosis of dementia due to Alzheimer's disease: recommendations from the National Institute on Aging-Alzheimer's Association workgroups on diagnostic guidelines for Alzheimer's disease. *Alzheimers Dement.* **7**, 263–269 (2011).
84. Hughes, C. P., Berg, L., Danziger, W. L., Coben, L. A. & Martin, R. L. A new clinical scale for the staging of dementia. *Br. J. Psychiatry* **140**, 566–572 (1982).
85. Williams, M. M., Storandt, M., Roe, C. M. & Morris, J. C. Progression of Alzheimer's disease as measured by Clinical Dementia Rating Sum of Boxes scores. *Alzheimers Dement.* **9**, S39–S44 (2013).
86. Cedarbaum, J. M. et al. Rationale for use of the Clinical Dementia Rating Sum of Boxes as a primary outcome measure for Alzheimer's disease clinical trials. *Alzheimers Dement.* **9**, S45–S55 (2013).
87. Jack, C. R. Jr. et al. NIA-AA research framework: toward a biological definition of Alzheimer's disease. *Alzheimers Dement.* **14**, 535–562 (2018).
88. Idland, A. V. et al. CSF neurofilament light levels predict hippocampal atrophy in cognitively healthy older adults. *Neurobiol. Aging* **49**, 138–144 (2017).
89. Hansson, O. et al. Association between CSF biomarkers and incipient Alzheimer's disease in patients with mild cognitive impairment: a follow-up study. *Lancet Neurol.* **5**, 228–234 (2006).
90. Daniel, B. & DeCoster, M. A. Quantification of sPLA2-induced early and late apoptosis changes in neuronal cell cultures using combined TUNEL and DAPI staining. *Brain Res. Brain Res. Protoc.* **13**, 144–150 (2004).
91. Mawuenyega, K. G. et al. Decreased clearance of CNS β-amyloid in Alzheimer's disease. *Science* **330**, 1774–1774 (2010).
92. Poppe, L. et al. EphA4 loss improves social memory performance and alters dendritic spine morphology without changes in amyloid pathology in a mouse model of Alzheimer's disease. *Alzheimers Res. Ther.* **11**, 1–13 (2019).
93. Huang, X. et al. A visual circuit related to the nucleus reuniens for the spatial-memory-promoting effects of light treatment. *Neuron* **109**, 347–362 (2021).
94. Bellantuono, I. et al. A toolbox for the longitudinal assessment of healthspan in aging mice. *Nat. Protoc.* **15**, 540–574 (2020).
95. Iaccarino, H. F. et al. Gamma frequency entrainment attenuates amyloid load and modifies microglia. *Nature* **540**, 230–235 (2016).
96. Mitchell, S. J. et al. Daily fasting improves health and survival in male mice independent of diet composition and calories. *Cell Metab.* **29**, 221–228 (2019).
97. Petr, M. A. et al. A cross-sectional study of functional and metabolic changes during aging through the lifespan in male mice. *eLife* **10**, e62952 (2021).
98. d'Errico, P. et al. Microglia contribute to the propagation of Aβ into unaffected brain tissue. *Nat. Neurosci.* **25**, 20–25 (2022).
99. Fang, E. F. et al. Defective mitophagy in XPA via PARP-1 hyperactivation and NAD(+)/SIRT1 reduction. *Cell* **157**, 882–896 (2014).
100. Griciuc, A. et al. Alzheimer's disease risk gene CD33 inhibits microglial uptake of amyloid beta. *Neuron* **78**, 631–643 (2013).
101. Fang, E. F. et al. NAD(+) replenishment improves lifespan and healthspan in ataxia telangiectasia models via mitophagy and DNA repair. *Cell Metab.* **24**, 566–581 (2016).
102. Peters, A. & Folger, C. A website entitled 'The fine structure of the aging brain'. *J. Comp. Neurol.* **521**, 1203–1206 (2013).
103. Lu, G. et al. WIPI2 positively regulates mitophagy by promoting mitochondrial recruitment of VCP. *Autophagy* **18**, 2865–2879 (2022).
104. Sun, N. et al. A fluorescence-based imaging method to measure in vitro and in vivo mitophagy using mt-Keima. *Nat. Protoc.* **12**, 1576–1587 (2017).

105. McEwan, W. A. et al. Cytosolic Fc receptor TRIM21 inhibits seeded tau aggregation. *Proc. Natl Acad. Sci. USA* **114**, 574–579 (2017).
106. Brenner, S. The genetics of *Caenorhabditis elegans*. *Genetics* **77**, 71–94 (1974).
107. Porta-de-la-Riva, M., Fontrodona, L., Villanueva, A. & Cerón, J. Basic *Caenorhabditis elegans* methods: synchronization and observation. *J. Vis. Exp.* **64**, e4019 (2012).
108. Calixto, A., Chelur, D., Topalidou, I., Chen, X. & Chalfie, M. Enhanced neuronal RNAi in *C. elegans* using SID-1. *Nat. Methods* **7**, 554–559 (2010).
109. Sutphin, G. L. & Kaeberlein, M. Measuring *Caenorhabditis elegans* life span on solid media. *J. Vis. Exp.* **27**, e1152 (2009).
110. Bargmann, C. I. & Horvitz, H. R. Chemosensory neurons with overlapping functions direct chemotaxis to multiple chemicals in *C. elegans*. *Neuron* **7**, 729–742 (1991).
111. Mramba, L. K. et al. Detecting potential outliers in longitudinal data with time-dependent covariates. *Eur. J. Clin. Nutr.* **78**, 344–350 (2024).
112. Altman, N. & Krzywinski, M. Analyzing outliers: influential or nuisance? *Nat. Methods* **13**, 281–282 (2016).
113. Salkovic, E., Sadeghi, M. A., Baggag, A., Salem, A. G. R. & Bensmail, H. OutSingle: a novel method of detecting and injecting outliers in RNA-Seq count data using the optimal hard threshold for singular values. *Bioinformatics* **39**, btad142 (2023).

Acknowledgements

This project was supported by the Cure Alzheimer's Fund (grant nos. 282952, 284930), Helse Sør-Øst (grant nos. 2020001, 2021021, 2023093), the Research Council of Norway (grant nos. 262175, 334361), the NordForsk Foundation (grant no. 119986), the National Natural Science Foundation of China (grant no. 81971327), Akershus University Hospital (grant nos. 269901, 261973, 262960), the Civitan Norges Forskningsfond for Alzheimers sykdom (grant no. 281931), the Czech Republic-Norway KAPPA program (with M. Vyhnálek, grant no. TO01000215) and HORIZON-TMA-MSCA-DN (grant no. 101073251, with R. Houtkooper) to E.F.F.; E.F.F. is also supported by the Rosa Sløyfe/Norwegian Cancer Society & Norwegian Breast Cancer Society (grant no. 207819) and Molecule AG/VITADAO (grant no. 282942). J.Z. is supported by Akershus University Hospital (grant nos. 263928, 390612) and Nasjonalforeningen for folkehelsen of Norway (grant no. 51418). H.-L.W. is supported by Nasjonalforeningen for folkehelsen of Norway (grant no. 43080). L.O.W. is funded by the South-Eastern Norway Regional Health Authorities (grant no. 2017095), the Norwegian Health Association (grant nos. 19536, 1513) and Wellcome Leap's Dynamic Resilience Program (jointly funded by Temasek Trust) (grant no. 104617). R.A. and S.-q.Z. were funded by the China Scholarship Council (https://www.csc.edu.cn/); the funders had no role in study design, data collection and analysis, decision to publish or preparation of the manuscript. A.-B.K. received funding from the Norwegian Health Association (grant no. 22679). G.C. was funded by the Key R&D Program Key Special Projects for International Science and Technology Innovation Cooperation between Governments (grant no. 2023YFE0118700), the National Natural Science Cross disciplinary Major Research Program (grant no. 92374203), the Science and Technology Project in Guangzhou (grant no. 202102070001), the Nonprofit Central Research Institute Fund of the Chinese Academy of Medical Sciences (grant no. 2024-JKCS-08), the Fundamental Research Funds for the Central Universities (grant no. 21625113) and Changzhi Medical College 1+1 Scientific Research Collaboration (grant no. HZZD202402). J.-P.P. was funded by the National Natural Science Foundation of China (grant no. 82301442) and the Norwegian Health Association (grant no. 35590). K.V. and M.V. were funded by National Institute for Neurological Research (Programme EXCELES, ID grant no. LX22NPO5107), which is funded by the European Union – Next Generation EU. The authors thank the participating individuals in the NorCog and COGNORM studies and also acknowledge NorCog for providing access to patient data and CSF samples.

Author contributions

E.F.F. provided the overall scientific ideas and experimental guidance. E.F.F. and G.C. designed the experiments and covered the experimental cost. J.-P.P., P.-J.W., J.Z., H.-L.W., S.L., M.J.L.-D., Z.-P.L. and L.-P.M. performed the experiments. A.-B.K., L.O.W., S.-q.Z., R.A., Q.W., S.L., T.H.E., T.Z., I.S., R.S.E., A.S., K.V., D.C., A.K.-F, H.P., T.S.-M., Z.W., H.W., L.-j.G., G.W., M.V., O.J.L., W.A.M., J.S.-M., L.G., Z.H., H.Z., M.P.W., N.B.H., D.A. and G.S. provided the experimental materials and comments on the data as well as editing of the paper. J.-P.P., P.-J.W., J.Z. and E.F.F. prepared the paper. E.F.F. and J.Z. did comprehensive editing of the paper.

Competing interests

E.F.F. is a co-owner of Fang-S Consultation AS (organization number 931 410 717) and NO-Age AS (organization number 933 219 127); he has an MTA with LMITO Therapeutics Inc. (South Korea), a CRADA arrangement with ChromaDex (USA), a commercialization agreement with Molecule AG/VITADAO and MTAs with GeneHarbor (Hong Kong) Biotechnologies Limited and Hong Kong Longevity Science Laboratory (Hong Kong); and he is a consultant to MindRank AI (China), NYO3 (Norway), AgeLab (Vitality Nordic AS, Norway) and Hong Kong Longevity Science Laboratory (Hong Kong). A.-B.K. has been principal investigator on the Boehringer-Ingelheim drug trial 1346.0023, the Roche drug trial BN29553 and the Novo Nordisk drug trial NN 6535-4730. The other authors declare no competing interests.

Additional information

Extended data is available for this paper at https://doi.org/10.1038/s43587-026-01108-z.

Supplementary information The online version contains supplementary material available at https://doi.org/10.1038/s43587-026-01108-z.

Correspondence and requests for materials should be addressed to Guobing Chen or Evandro Fei Fang.

Peer review information *Nature Aging* thanks the anonymous reviewers for their contribution to the peer review of this work.

[1]Department of Microbiology and Immunology, School of Medicine; Institute of Geriatric Immunology, School of Medicine, Jinan University, Guangzhou, China. [2]Guangdong Second Provincial General Hospital, Postdoctoral Research Station of Basic Medicine, School of Medicine, Jinan University, Guangzhou, China. [3]Department of Clinical Molecular Biology, University of Oslo and Akershus University Hospital, Lørenskog, Norway. [4]Department of Neurology, The First Affiliated Hospital of Zhengzhou University, Zhengzhou, China. [5]Xiangya School of Stomatology, Central South University, Changsha, China. [6]Department of Geriatric Medicine, Oslo University Hospital (Ullevaal), Oslo, Norway. [7]Institute of Clinical Medicine Campus Ahus, University of Oslo, Lørenskog, Norway. [8]Department of Geriatric Medicine, Akershus University Hospital, Lørenskog, Norway. [9]Department of Systems Biomedical Sciences, School of Medicine, Jinan University, Guangzhou, China. [10]Department of Geriatrics, The First Affiliated Hospital of Zhengzhou University, Zhengzhou, China. [11]Centre for Reproduction, Development and Aging, Faculty of Health Sciences, University of Macau, Macau, China. [12]Department of Neuromedicine and Movement Science, Norwegian University of Science and Technology, Trondheim, Norway. [13]Department of Geriatrics, St. Olavs Hospital, University Hospital of Trondheim, Trondheim, Norway. [14]UK Dementia Research Institute, Department of Clinical Neurosciences, University of Cambridge, Cambridge, UK. [15]Memory Clinic, Department of Neurology, Charles University, 2nd Faculty of Medicine and Motol University Hospital, Prague, Czech Republic. [16]Kavli Institute for Systems Neuroscience, K.G. Jebsen Centre for Alzheimer's Disease, Centre for Algorithms in the Cortex, Egil and Pauline Braathen and Fred Kavli Centre for Cortical Microcircuits, Faculty of Medicine and Health Sciences, Norwegian University of Science and Technology, Trondheim, Norway. [17]School of Pharmaceutical Sciences, Tsinghua-Peking Joint Center for Life Sciences, Beijing Frontier Research Center for Biological Structure, Tsinghua University, Beijing, China. [18]Institute of Clinical Medicine, Campus Ullevål, University of Oslo, Oslo, Norway. [19]Synaptic Neurochemistry and Amino Acid Transporters Labs, Division of Anatomy, Department of Molecular Medicine, Institute of Basic Medical Sciences (IMB) and Healthy Brain Aging Centre (SERTA), University of Oslo, Oslo, Norway. [20]The Norwegian Centre on Healthy Ageing (NO-Age) and The Norwegian National Anti-Alzheimer's Disease (NO-AD) Networks, Oslo, Norway. [21]Helen and Robert Appel Alzheimer's Disease Research Institute, Feil Family Brain and Mind Research Institute, Weill Cornell Medicine, New York, NY, USA. [22]Department of Psychiatry and Neurochemistry, Institute of Neuroscience and Physiology, Sahlgrenska Academy, University of Gothenburg, Mölndal, Sweden. [23]Clinical Neurochemistry Laboratory, Sahlgrenska University Hospital, Mölndal, Sweden. [24]Department of Neurodegenerative Disease, UCL Institute of Neurology, London, UK. [25]UK Dementia Research Institute at UCL, London, UK. [26]Hong Kong Center for Neurodegenerative Diseases, Hong Kong, China. [27]Wisconsin Alzheimer's Disease Research Center, University of Wisconsin School of Medicine and Public Health, University of Wisconsin-Madison, Madison, WI, USA. [28]Department of Old Age Psychiatry, Institute of Psychiatry, Psychology and Neuroscience, King's College London, London, UK. [29]Centre for Age-Related Medicine (SESAM), Stavanger University Hospital, Stavanger, Norway. [30]Norwegian National Centre for Aging and Health, Vestfold Hospital Trust, Tønsberg, Norway. [31]Faculty of Medicine, University of Oslo, Oslo, Norway. [32]Zhuhai Institute of Jinan University, Jinan University, Zhuhai, China. [33]These authors contributed equally: Jun-Ping Pan, Ping-Jie Wang, Jianying Zhang, Anne-Brita Knapskog, Leiv Otto Watne. ✉e-mail: guobingchen@jnu.edu.cn; e.f.fang@medisin.uio.no

https://doi.org/10.1038/s43587-026-01108-z

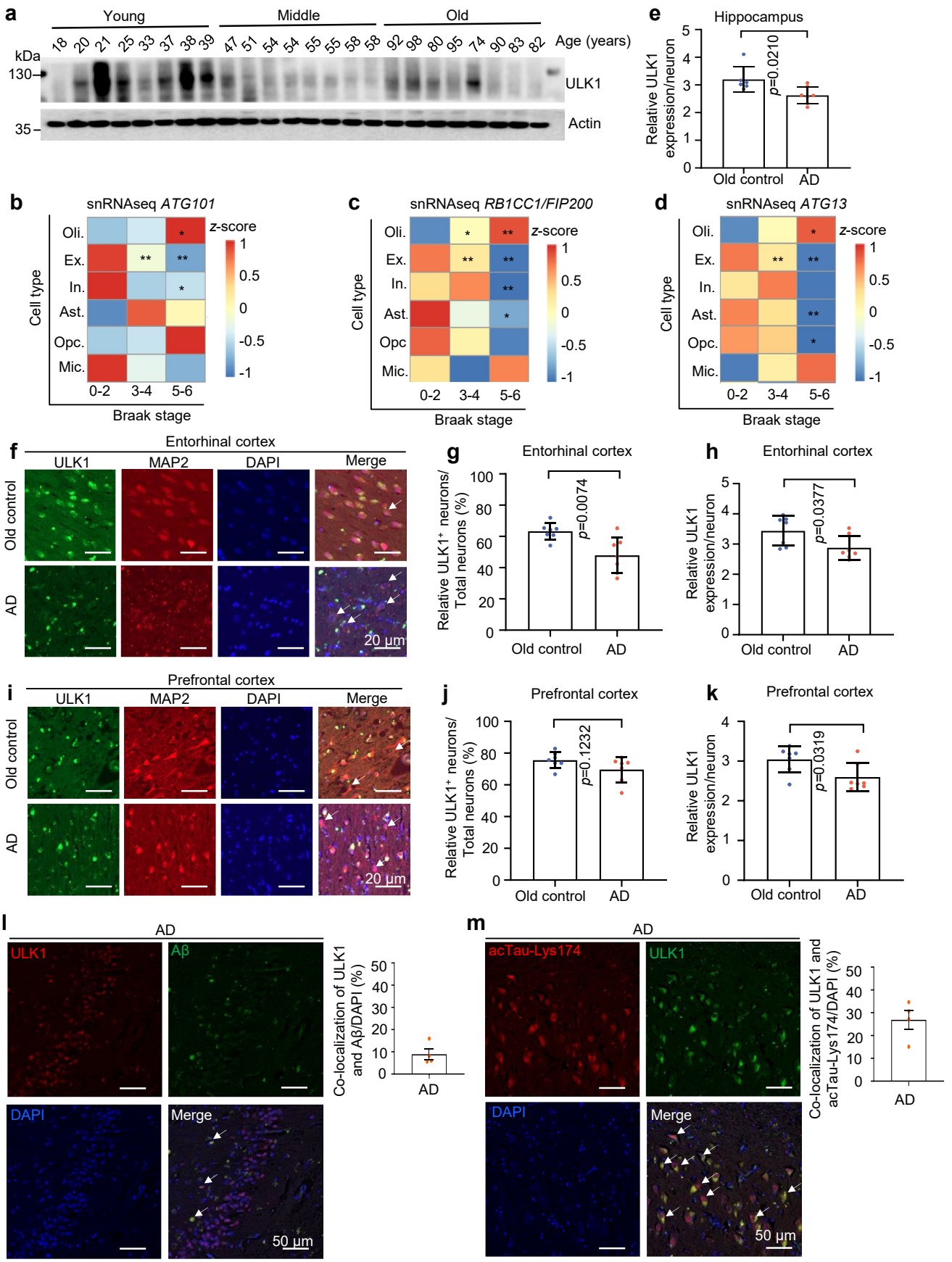

Extended Data Fig. 1 | See next page for caption.

https://doi.org/10.1038/s43587-026-01108-z

Extended Data Fig. 1 | ULK1 declines with age, diminishes further in AD, and is inversely correlated with AD severity. (**a**) Western blotting showing changes of ULK1 expression in hippocampal tissues from young, middle-aged, and old humans (n = 8 per group). (**b-d**) Heat map data showing the relative abundance of *ATG101*, *RB1CC/FIP200*, and *ATG13* mRNA stratified by Braak stages (0/2, 3/4, 5/6) and brain cell types (Oli., oligodendrocytes; Ex., excitatory neurons; In., inhibitory neurons; Ast., astrocytes; Opc., oligodendrocyte progenitor cells; Mic., microglia). Data represent single cell mRNA samples prepared from post-mortem human brain. (**e**) Changes of ULK1 signal intensity/neuron between old control and AD. (**f-k**) Changes of ULK1 in the entorhinal and prefrontal tissues between old control and AD patients. Slides were immunostained for ULK1 (green), Map2 (red), and nucleus (DAPI, blue), signals detected by immunofluorescence, and with merged images shown as indicated. Scale bars = 20 μm. Two types of data quantification were used, including data were presented as ULK1-positive ($ULK1^+$) neurons/total neurons (**j**, **i**) or signal intensity/neuron (**h**, **k**). (**l**) Representative images of hippocampal brain region of AD patient of the indicated genotype stained for ULK1 (Red), Aβ plaques (6E10-positive, green) and nucleus (DAPI, blue). Scale bars = 50 μm. (**m**) Representative images of cortical brain region of AD patient of the indicated genotype stained for cTau-Lys174 (Red), ULK1 (green) and nucleus (DAPI, blue). Scale bars = 50 μm. Unless specified elsewhere, data are mean ± S.E.M. Statistical analyses were as follows: two-sided unpaired two-tailed Student's t-test (**e**, **g**, **h**, **i**, **k**). Wilcox test (**b**, **c**, **d**). n.s., not significant, $^*p < 0.05$, $^{**}p < 0.01$, $^{***}p < 0.001$.

https://doi.org/10.1038/s43587-026-01108-z

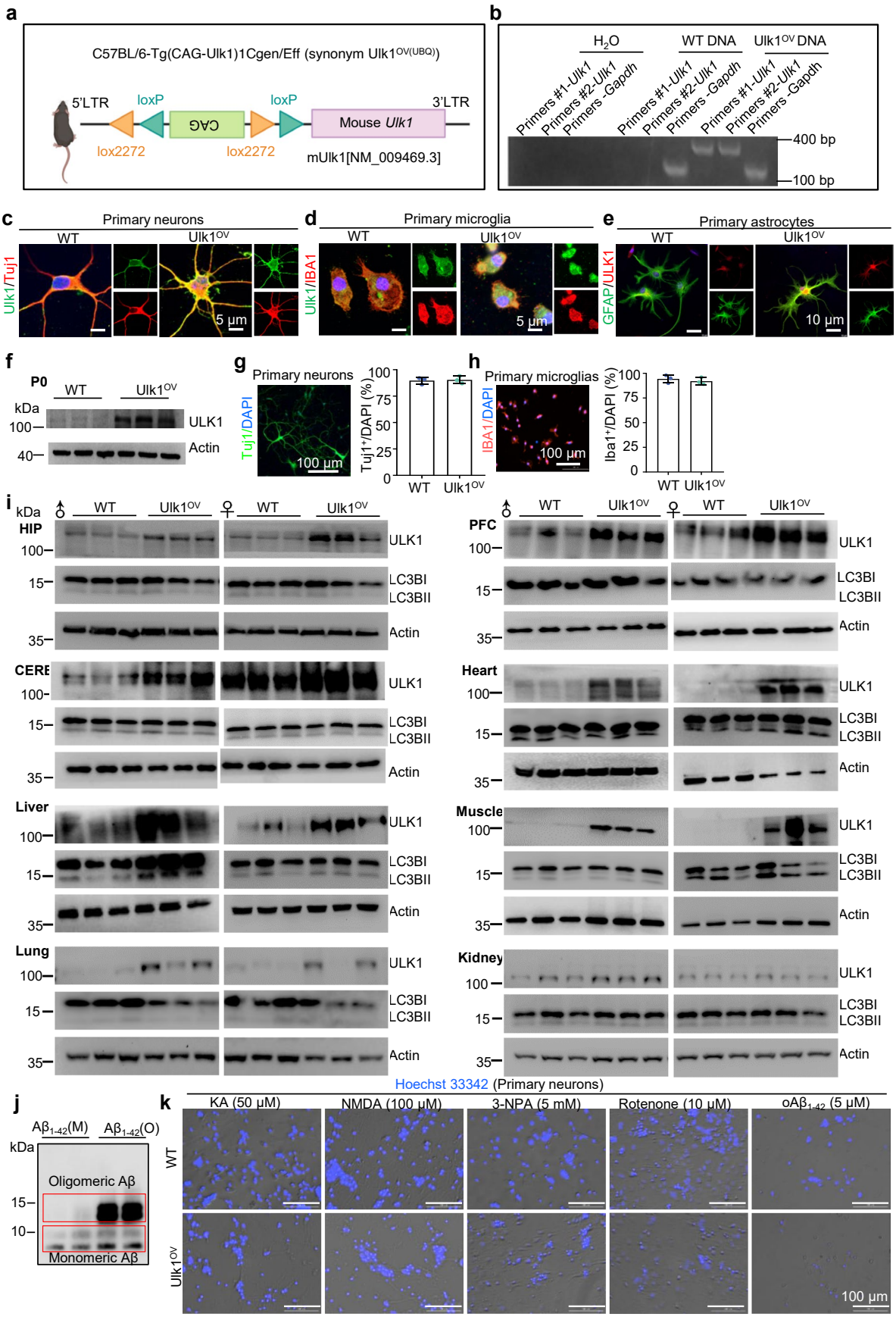

Extended Data Fig. 2 | See next page for caption.

https://doi.org/10.1038/s43587-026-01108-z

Extended Data Fig. 2 | Strategy to create Ulk1^{ov} mouse, and validation of ubiquitous high expression of ULK1 in Ulk1^{ov} mice, primary neurons, astrocytes, and microglia, with assessment of response to neurotoxic stress. (**a, b**) A schematic diagram of the strategy used to generate the Ulk1^{OV} mice (**a**) with PCR showing validated initial clones (**b**). (**c**-**e**) Representative images of primary neurons (**c**), microglia (**d**) and astrocytes (**e**) from brains of WT and Ulk1^{OV} mice stained for ULK1 and co-stained with Tuj1 (neuronal marker), IBA1 (microglial marker), or GFAP (a marker of astrocyte), as indicated. Scale bars = 5 µm (**c**, **d**) and 10 µm (**e**). (**f**) Representative western blots of ULK1 in extracts of whole brain tissue from WT and Ulk1^{OV} mice on postnatal day 0 (P0) (n = 3 mice/group). Actin was used as house a keeping control for quantification. (**g, h**) Representative images showing high purity of isolated primary cortical neurons (**g**) and microglia (**h**) from WT and Ulk1^{OV} mice. Neurons were co-stained with Tuj1 (neuronal marker) and DAPI (nucleus marker); microglia were co-stained with Iba1 (microglial marker) and DAPI. Scale bars = 100 µm. The high purity of isolated neuronal (or microglia) is indicated by the high percentage of Tuj1-positive neurons (or Iba1-positive microglia). (**i**) Western blot data of ULK1 and LC3B in whole cell extracts from HIP, PFC, and CERE of brain tissue and key organs (heart, liver, lung, kidney, muscle) from WT and Ulk1^{OV} mice (n = 3 female and male mice/group). HIP, hippocampus; PFC, prefrontal cortex; CERE, cerebellum. (**j**) Immunoblot analysis of different types of $A\beta_{1\text{-}42}$ prepared in this study according to in-house preparation protocol. (**k**) Representative Hoechst-staining (blue) images of cultured cortical neurons from WT and Ulk1^{OV} mice after 24 h exposure to the indicated reagents. Doses used were: 50 µM kainic acid (KA), 100 µM N-methyl-D-aspartate (NMDA), 5 mM 3-nitropropionic acid (3-NPA), 10 µM Rotenone, and 5 µM oAβ. Scale bars = 100 µm.

https://doi.org/10.1038/s43587-026-01108-z

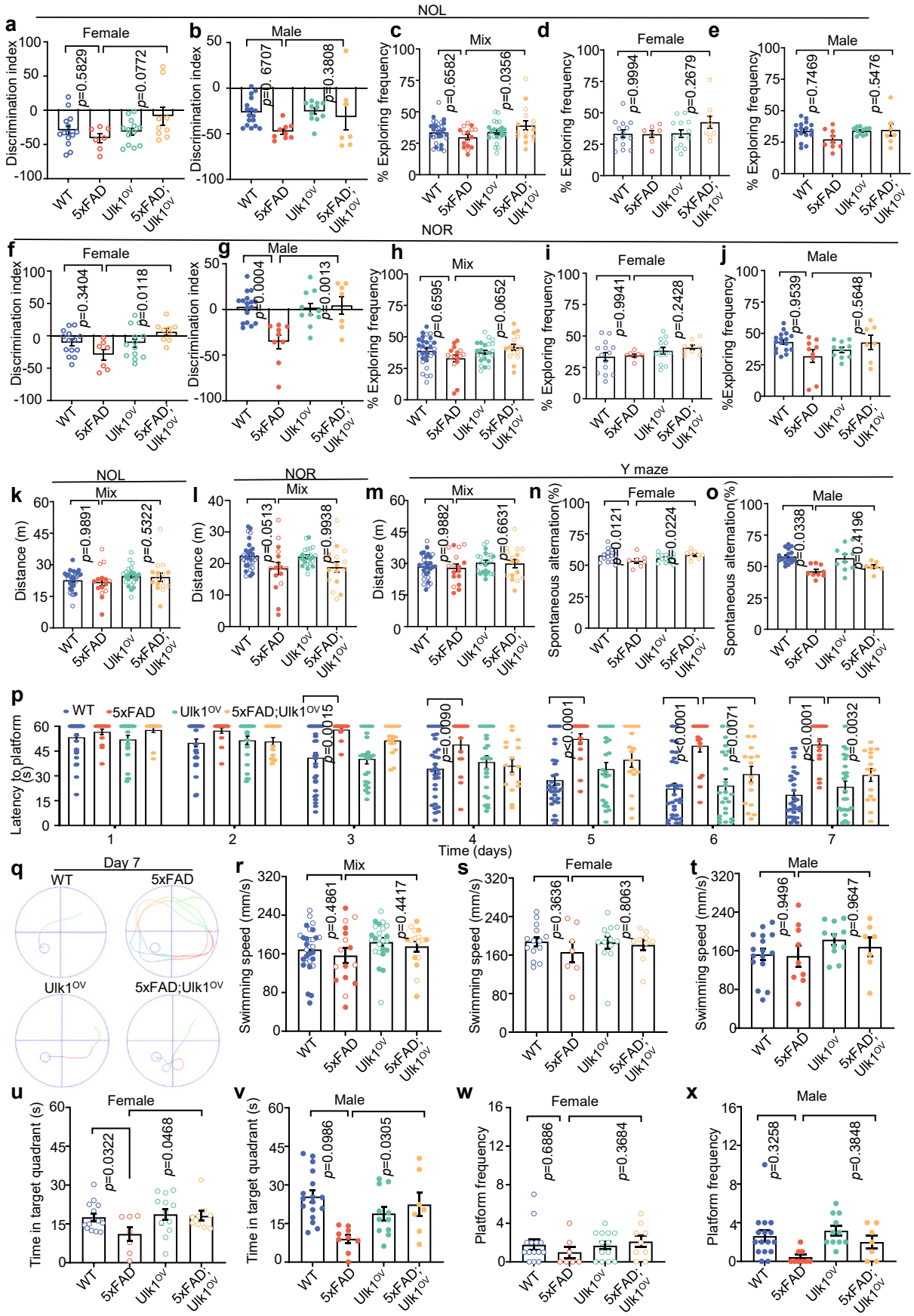

Extended Data Fig. 3 | See next page for caption.

https://doi.org/10.1038/s43587-026-01108-z

Extended Data Fig. 3 | Summary of behavioral studies in WT, 5xFAD, Ulk1^{ov}, and 5xFAD;Ulk1^{ov} mice. (**a**-**e**) Behavioral assays were performed using WT, 5xFAD, Ulk1^{ov}, and 5xFAD;Ulk1^{ov} mice. Results of novel objection location (NOL) tests in female (**a**, **d**), male (**b**, **e**) or mixed-sex mice showing discrimination index (**a**, **b**) or % exploring frequency (**c**, **d**, **e**). Female mice: n = 14, 7, 13 and 9 mice for WT, 5xFAD, Ulk1^{ov}, and 5xFAD;Ulk1^{ov}, respectively. Male mice: n = 17, 9, 10 and 7 mice for WT, 5xFAD, Ulk1^{ov}, and 5xFAD;Ulk1^{ov}, respectively. **(f-j)** Results of novel objection recognition (NOR) test. Discrimination index in female (**f**) and male (**g**) mice as well as percentage of exploring frequency showing in mixed (**h**), female (**i**), and male **(j)** mice are presented. Female mice: n = 14, 7, 13 and 9 mice for WT, 5xFAD, Ulk1^{ov}, and 5xFAD;Ulk1^{ov}, respectively. Male mice: n = 17, 9, 11 and 7 mice for WT, 5xFAD, Ulk1^{ov}, and 5xFAD;Ulk1^{ov}, respectively. (**k**-**m**) Distance explored by mice of different groups in the NOL (**k**), NOR (**l**), and Y maze (**m**) tests. n = 16-32 mice/group. **(n, o)** Spontaneous alternation was scored during the Y maze test in female **(n)** and male **(o)** mice of the indicated genotypes. Female mice: n = 14, 7, 13 and 9 mice for WT, 5xFAD, Ulk1^{ov}, and 5xFAD;Ulk1^{ov}, respectively. Male mice: n = 17, 9, 10 and 7 mice for WT, 5xFAD, Ulk1^{ov}, and 5xFAD;Ulk1^{ov}, respectively. (**p**-**x**) Results of the MWM test. The numbers of mice used were n = 7-14 female mice for WT, 5xFAD, Ulk1^{ov}, and 5xFAD;Ulk1^{ov}; while n = 7-17 male mice for WT, 5xFAD, Ulk1^{ov}, and 5xFAD;Ulk1^{ov}. Latency to platform during the 7-day initial training period of the MWM test (**p**); representative images of day 7 corresponding to (**p**) are shown in (**q**). Swimming speed during day 8 probe trial test using mixed sex (**r**), female (**s**) or male (**t**) mice. Time spent in the target quadrant during day 8 probe trial test using female (**u**) or male (**v**) mice. Number of times passing the platform location counted for female (**w**) or male (**x**) mice of the indicated genotypes. Open and closed dots correspond to results for female and male mice, respectively. Unless specified elsewhere, data are mean ± S.E.M. Statistical analyses performed were Two-way ANOVA followed by Dunnett's multiple comparisons test (**a**-**p**, **r**-**x**).

https://doi.org/10.1038/s43587-026-01108-z

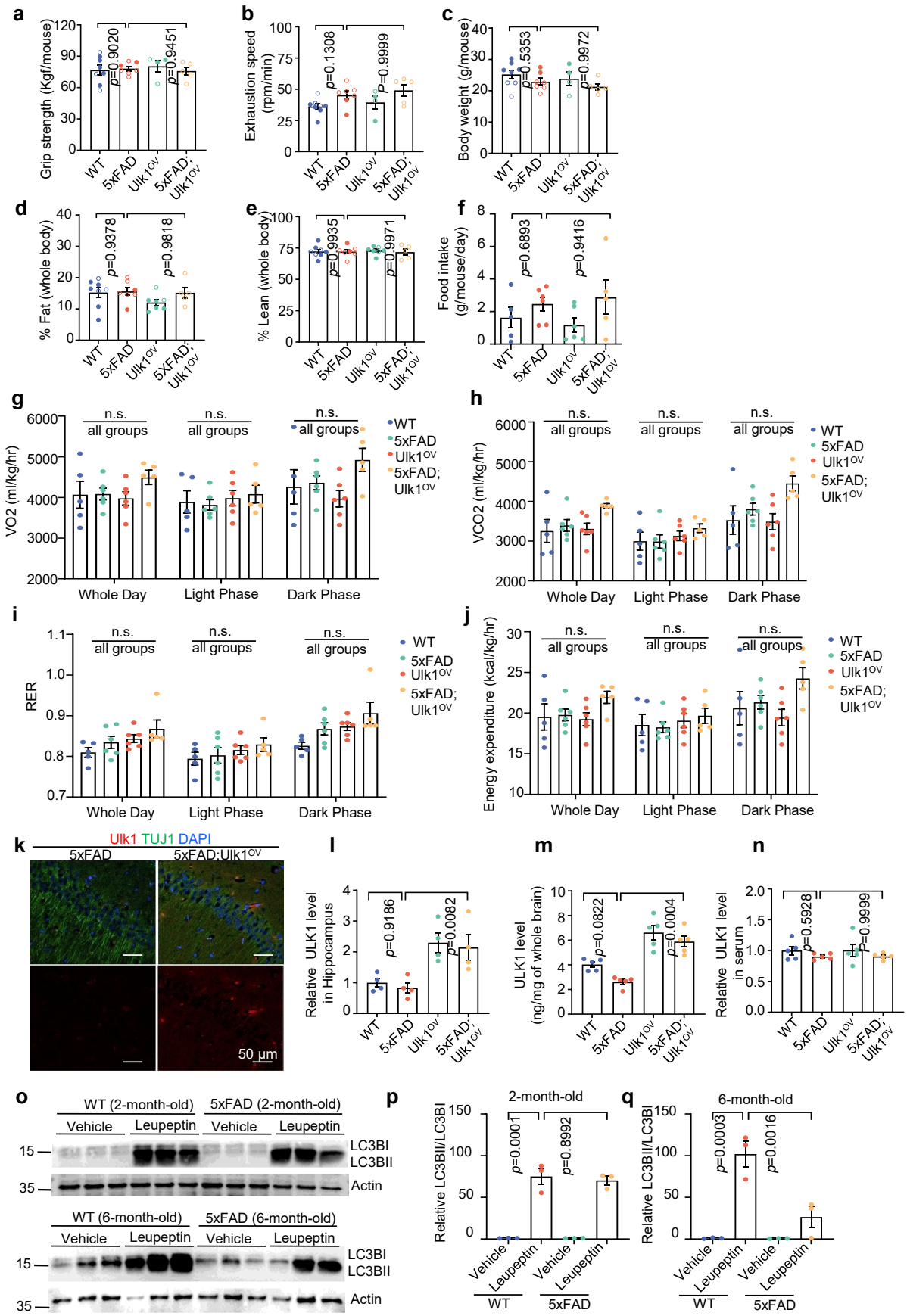

Extended Data Fig. 4 | See next page for caption.

https://doi.org/10.1038/s43587-026-01108-z

Extended Data Fig. 4 | Overexpression of ULK1 does not affect grip strength, exhaustion speed, body composition, or metabolism in 7-month-old 5xFAD mice. (**a**) Forelimb grip strength of mice with different genotypes. Open and closed dots correspond to test results for female and male mice, respectively. (**b**) Exhaustion rate of mice with different genotypes in the rotarod test. Open and closed dots correspond to test results for female and male mice, respectively. (**c-e**) Information on whole-body weight, lean tissue mass, and whole-body fat mass by low-field nuclear magnetic resonance imaging. Open and closed dots correspond to test results for female and male mice, respectively. (**f-j**) Average daily food intake, hourly oxygen consumption, hourly carbon dioxide exhalation, hourly respiratory exchange ratio (RER), and hourly energy expenditure of mice in a metabolic cage during dark/light cycles. (**k, l**) Representative images of hippocampal brain region of the indicated genotype stained for Ulk1, neuron marker (TUJ1-positive) and nucleus (DAPI, blue) (**j**). Scale bars = 50 μm. Ulk1 expression, in relative level, were quantified (**k**). n = 4 mice/group (4 slides/mouse). (**m, n**) ULK1 levels in whole brain and serum of WT, 5xFAD, Ulk1^{OV}, and 5xFAD;Ulk1^{OV} mice (7-month). n = 5 mice/group. (**o-q**) Western blot analysis of autophagy-related (LC3B) in hippocampal tissues from 2-and 6- month-old WT and 5xFAD mice treated with the autophagy-lysosome inhibitor leupeptin to assess autophagic flux. Representative western blot images (**o**) and quantified data in (**p, q**) are shown. n = 3 mice/group. Data are mean ± S.E.M. Statistical analyses performed were Two-way ANOVA followed by Dunnett's multiple comparisons test (**a-j**, **l-n**, **p**). n.s., not significant.

https://doi.org/10.1038/s43587-026-01108-z

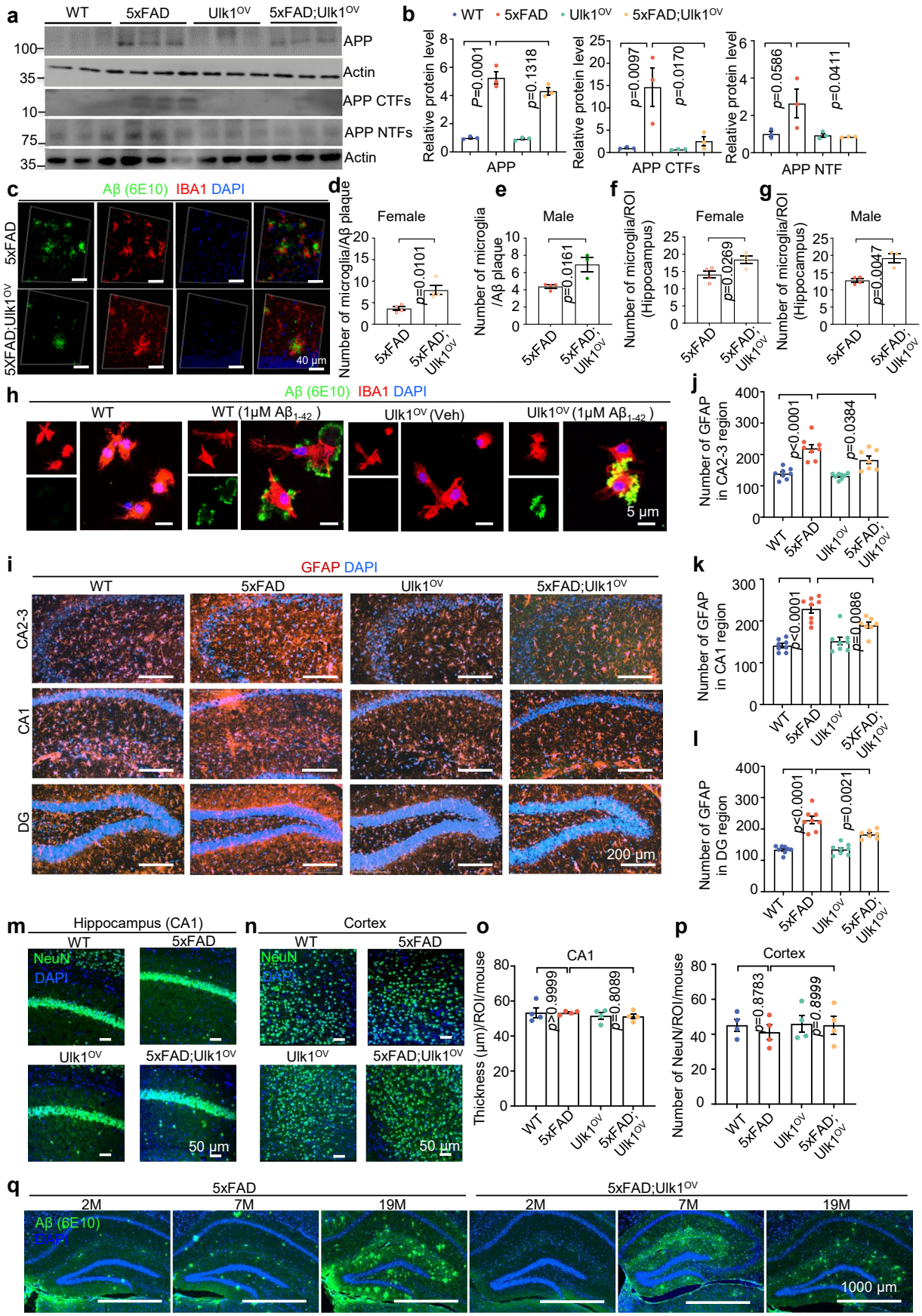

Extended Data Fig. 5 | See next page for caption.

https://doi.org/10.1038/s43587-026-01108-z

Extended Data Fig. 5 | Effects of ULK1 overexpression on amyloid pathology, microgliosis, and astrogliosis in 5xFAD mice. (a, b) Western blot analysis of amyloid precursor protein (APP) and its cleavage fragments (APP CTFs and APP NTFs) in hippocampal tissues from WT, 5xFAD, Ulk1^{OV}, and 5xFAD;Ulk1^{OV} mice. Western blots (**a**) and quantified data (**b**) of the designated proteins in different mouse groups (n = 3 mice/group). APP-CTF – APP C-terminal fragment; APP-NTF - APP N-terminal fragment. **(c-g)** Representative images of hippocampal brain region in 7.5-month-old mice of the indicated genotype stained for Aβ plaques (6E10-positive, green), microglia (Iba1-positive, red), and nucleus (DAPI, blue) (**c**). Scale bars = 40 µm. Number of microglia/Aβ plaque in female (**d**) and male (**e**) mice (n = 3 or 4 mice/group, and the value from each mouse were from the data of 6 slides). Number of microglia (Iba1^{+}) engulfing or near Aβ plaques in female (**f**) and male (**g**) mice. Open and closed dots correspond to data for female and male mice, respectively (**d-g**). **(h)** Microglia from mice of the indicated genotype were treated with Veh (DMSO) or 1uM $Aβ_{1-42}$. Phagocytic activity of microglia was estimated based on number and proximity to Aβ plaques. Scale bars = 5 µm. **(i-l)** Aβ plaques and astrogliosis were quantified in hippocampal tissue from mice of the indicated genotypes. Representative images show amyloid plaques (6E10-positive, green) and astrocytes (GFAP-positive, red) in the indicated brain regions (**i**). Quantitation of astrocyte abundance based of GFAP immunofluorescence intensity in CA2-3 (**j**), CA1 (**k**) and DG (**l**) brain regions. Scale bars = 200 µm. (n = 7- 8 mice/group). **(m-p)** Immunofluorescence was used to quantify NeuN and DAPI staining in the hippocampal CA1 of 7-month-old mice (**m**). The thickness of neurons in hippocampal CA1 region was assessed and is shown in (**o**) (n = 4 mice per group with 8 randomly selected areas in the regions of interest (ROIs) were selected per mouse). Representative images of cortical neurons (**n**); number of neurons/ROI is shown in (**p**) (n = 4 mice per group with 4 randomly selected areas in the ROI/mouse). Scale bars = 50 µm. **(q)** Representative images showing hippocampal tissue from 2-, 7-, and 19-month-old mice stained for amyloid plaques (6E10-positive, green) and microglia (Iba1-positive, red). Scale bars = 1000 µm. Unless specified elsewhere, data are mean ± S.E.M. Statistical analyses performed were two-way ANOVA followed by Dunnett's multiple comparisons (**b**, **j**, **k**, **l**); two-sided unpaired two-tailed Student's t-test (**d-g**)two-way ANOVA followed by Dunnett's multiple comparisons (**o**, **p**). Unless specified elsewhere, data are mean ± S.E.M. Statistical analyses performed were two-sided unpaired two-tailed Student's t-test (**d**, **e**); two-way ANOVA followed by Dunnett's multiple comparisons test (**f-h**, **k**, **l**, **n**, **o**, **q**); repeated measures ANOVA followed by Tukey's multiple-comparisons test (**i, j**). n.s., not significant, $^{*}p < 0.05$, $^{**}p < 0.01$, $^{***}p < 0.001$.

https://doi.org/10.1038/s43587-026-01108-z

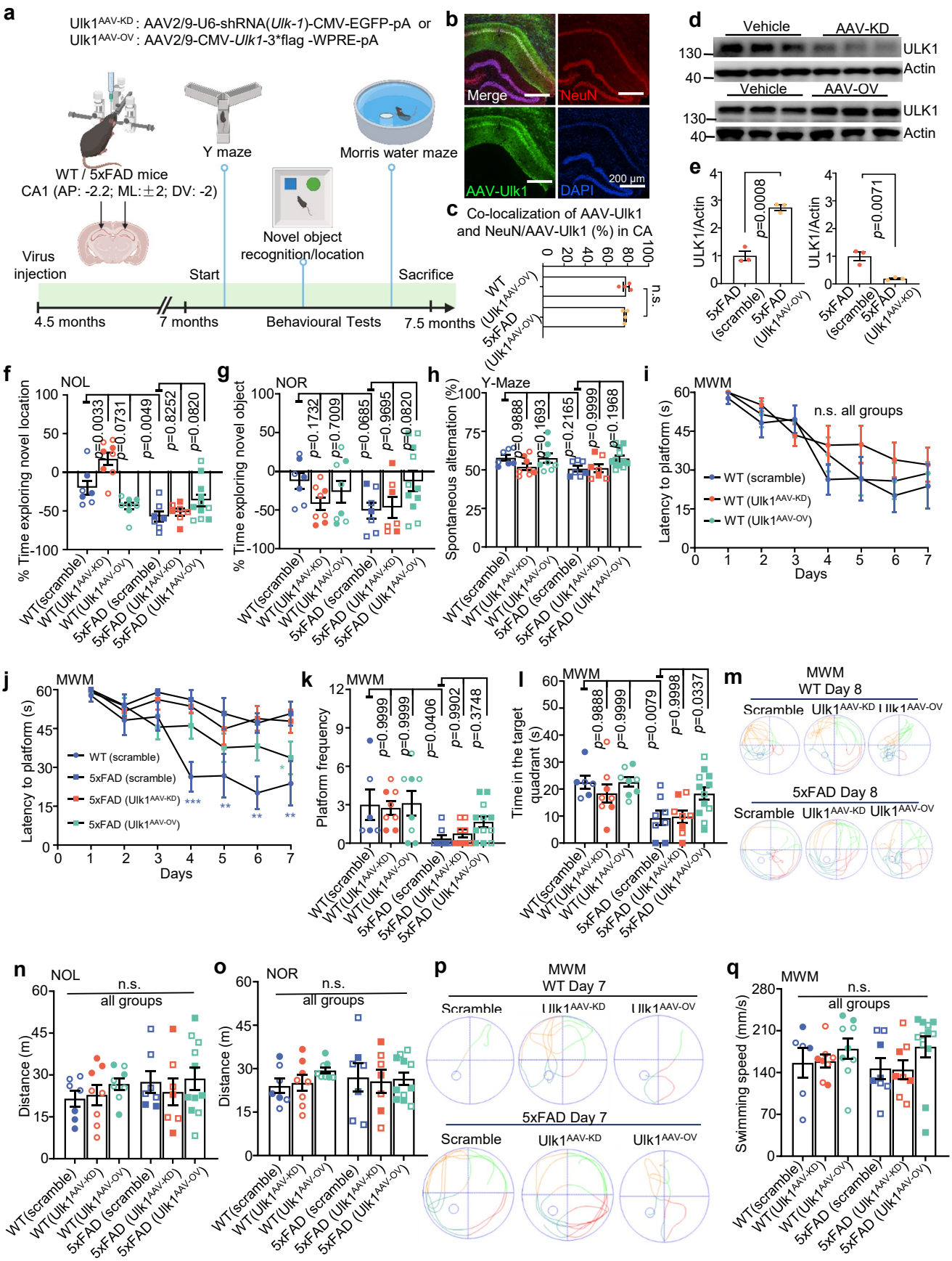

Extended Data Fig. 6 | See next page for caption.

https://doi.org/10.1038/s43587-026-01108-z

Extended Data Fig. 6 | Pan-neuronal AAV-mediated overexpression of ULK1 antagonizes cognitive decline in 5xFAD mice. (**a**) Schematic illustration of the workflow and data collection. Two recombinant AAV clones, AAV2/9-CMV-Ulk1-3*flag-WPRE-pA ($Ulk1^{AAV\text{-}OV}$) and AAV2/9-U6-shRNA(*Ulk-1*)-CMV-EGFP-pA, $Ulk1^{AAV\text{-}KD}$) were individually injected bilaterally into the hippocampal region of 4.5-month-old 5×FAD mice to generate mice that overexpress or lack ULK1 in neural tissue, respectively. Equivalent viral constructs with "scrambled" target sequences were injected and the resulting mice were used as negative controls. Behavioral tests were conducted 2 months after injection. (**b**) A representative confocal image showing AAV-ULK1 (green) and NeuN (red) in neural tissue 4 weeks after AAV injection. (**c**) Quantification of co-localization of AAV-ULK1 with NeuN, and the percentage of AAV-ULK1-positive cells that were also NeuN-positive in CA regions. For each group, n = 4 mice. (**d**-**e**) The efficient expression of $Ulk1^{AAV\text{-}OV}$ and $Ulk1^{AAV\text{-}KD}$ in their respective groups experimental mice is demonstrated in a representative Western blot (**d**). Quantification of Western blot data (**e**) is shown in (**e**) (n = 3 mice/group). (**f**-**h**) Results of NOL (**f**), NOR (**g**) and Y-Maze (**h**) tests are presented. Tests were administered to n = 7, 8, 8, 7, 7 and 12 mice for WT(scramble), WT($Ulk1^{AAV\text{-}KD}$), WT($Ulk1^{AAV\text{-}OV}$), 5xFAD (scramble), 5xFAD ($Ulk1^{AAV\text{-}KD}$), and 5xFAD ($Ulk1^{AAV\text{-}OV}$) mice, respectively. Circles and squares represent the WT and 5xFAD, respectively, with open dots indicating female mice and closed dots indicating male mice. **(i-m)** Results of MWM assays during the initial 7-day training period are shown (**i**, **j**). Results of day 8 probe trial test including platform frequency (**k**) and time spent in target quadrant (**l**) are shown. A representative set of images collected during the probe trial are presented (**m**). For these experiments, n = 6, 8, 8, 7, 8 and 11 mice were used for WT(scramble), WT($Ulk1^{AAV\text{-}KD}$), WT($Ulk1^{AAV\text{-}OV}$), 5xFAD (scramble), 5xFAD ($Ulk1^{AAV\text{-}KD}$), and 5xFAD ($Ulk1^{AAV\text{-}OV}$), respectively. Circles and squares represent the WT and 5xFAD, respectively, with open dots indicating female mice and closed dots indicating male mice. (**n, o**) The total distance travelled (in meters) was recorded in each group of mice during the NOL (**n**) and NOR (**o**) tests. (**p**) Representative trajectories of distance traveled in the MWM test on day 7. (**q**) Data for swimming speed of each mouse group (day 8). Unless specified elsewhere, data are mean ± S.E.M. Statistical analyses performed were two-sided unpaired two-tailed Student's t-test (**d**, **e**); two-way ANOVA followed by Dunnett's multiple comparisons test (**f**-**h**, **k**, **l**, **n**, **o**, **q**); repeated measures ANOVA followed by Tukey's multiple-comparisons test (**l**, **j**). n.s., not significant, $^{*}p < 0.05$, $^{**}p < 0.01$, $^{***}p < 0.001$.

https://doi.org/10.1038/s43587-026-01108-z

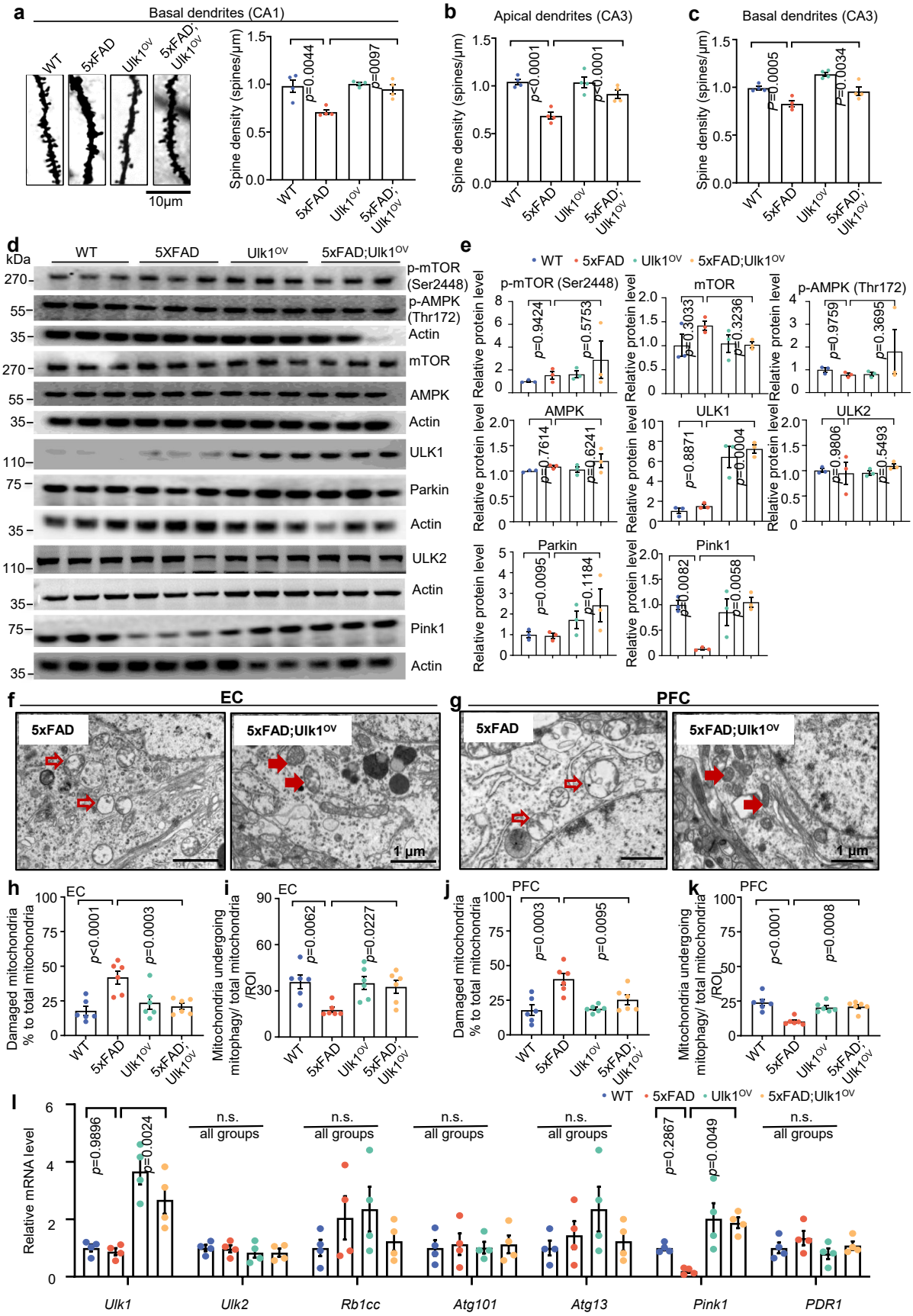

Extended Data Fig. 7 | See next page for caption.

https://doi.org/10.1038/s43587-026-01108-z

Extended Data Fig. 7 | Effect of overexpression of ULK1 on spine density, mitophagy, and mitochondrial homeostasis in the 5xFAD mouse brain. (**a**) Representative images and quantification of basal dendritic spine density in hippocampal CA1 of WT, 5xFAD, $Ulk1^{OV}$ and 5xFAD;$Ulk1^{OV}$ mice (n = 60 dendritic fragments from 4 mice). Scale bars = 10 µm. (**b**-**c**) Apical (**b**) and basal (**c**) dendritic spine density in CA3 of mice of the indicated genotypes (n = 60 dendritic fragments from 4 mice). (**d, e**) Effects of ULK1 overexpression on expression of the indicated proteins in hippocampal tissues of mice of the indicated genotypes. Representative western blots (**d**) and quantified data (**e**) (n = 3 mice/group). (**f**-**k**) Representative images of damaged mitochondria in entorhinal cortex (EC) (**f**) and prefrontal cortex (PFC) (**g**) brain regions from mice of the indicated genotype. Mitophagy events and percent damaged mitochondria in (**f**) and (**g**) were quantified and are shown in (**h**) to (**k**); % damaged mitochondria (**h**, **j**) and mitophagy (**i**, **k**) estimates are based on 50-200 mitochondria per group; n = 6 mice/group; approximately 20 images per/mouse. Scale bars = 1 µm. (**l**) Quantification of the indicated mRNA (n = 4 mice/group). Unless specified elsewhere, data are mean ± S.E.M. Statistical significance was determined using two-way ANOVA followed by Dunnett's multiple comparisons (**a**-**c**, **e**, **h**-**i**). n.s., not significant, $^{*}p < 0.05$, $^{**}p < 0.01$, $^{***}p < 0.001$.

https://doi.org/10.1038/s43587-026-01108-z

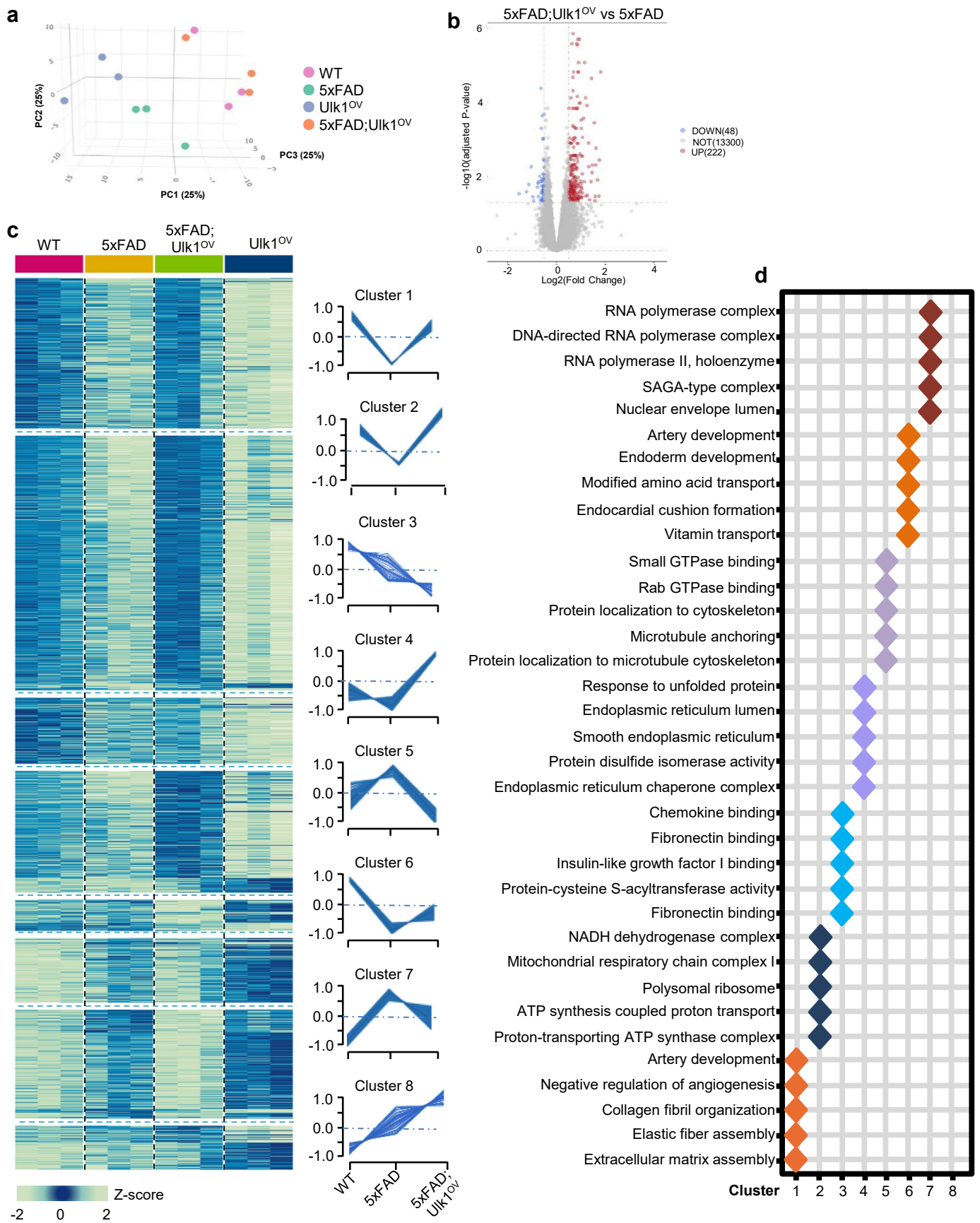

Extended Data Fig. 8 | See next page for caption.

https://doi.org/10.1038/s43587-026-01108-z

Extended Data Fig. 8 | Differential gene expression and gene ontology functional analysis in WT, 5xFAD, Ulk1^{ov}, and 5xFAD;Ulk1^{ov} mice. (**a**) Three-dimensional (3D) principal component analysis (PCA) of RNA-seq data using hippocampal brain tissue from WT, 5xFAD, Ulk1^{ov}, and 5xFAD;Ulk1^{ov} mice. Each point represents an individual mouse (n = 3 male mice/group). (**b**) Volcano plot analysis up- or down-regulated genes in 5xFAD;Ulk1^{ov} and 5xFAD mice. (**c**) Heatmap showing differentially up- or down-regulated genes in WT, 5xFAD, Ulk1^{ov}, and 5xFAD;Ulk1^{ov} mice. The color gradient from blue to white represents high to low gene expression. Hierarchical clustering identified eight gene clusters, and expression trends for each of the 8 clusters by mouse genotype are summarized to the right of the heat map. (**d**) Gene Ontology (GO) analysis of genes enriched in clusters 1-8. Different colors represent the pathways enriched in each gene cluster; some clusters show no significant enrichment.

https://doi.org/10.1038/s43587-026-01108-z

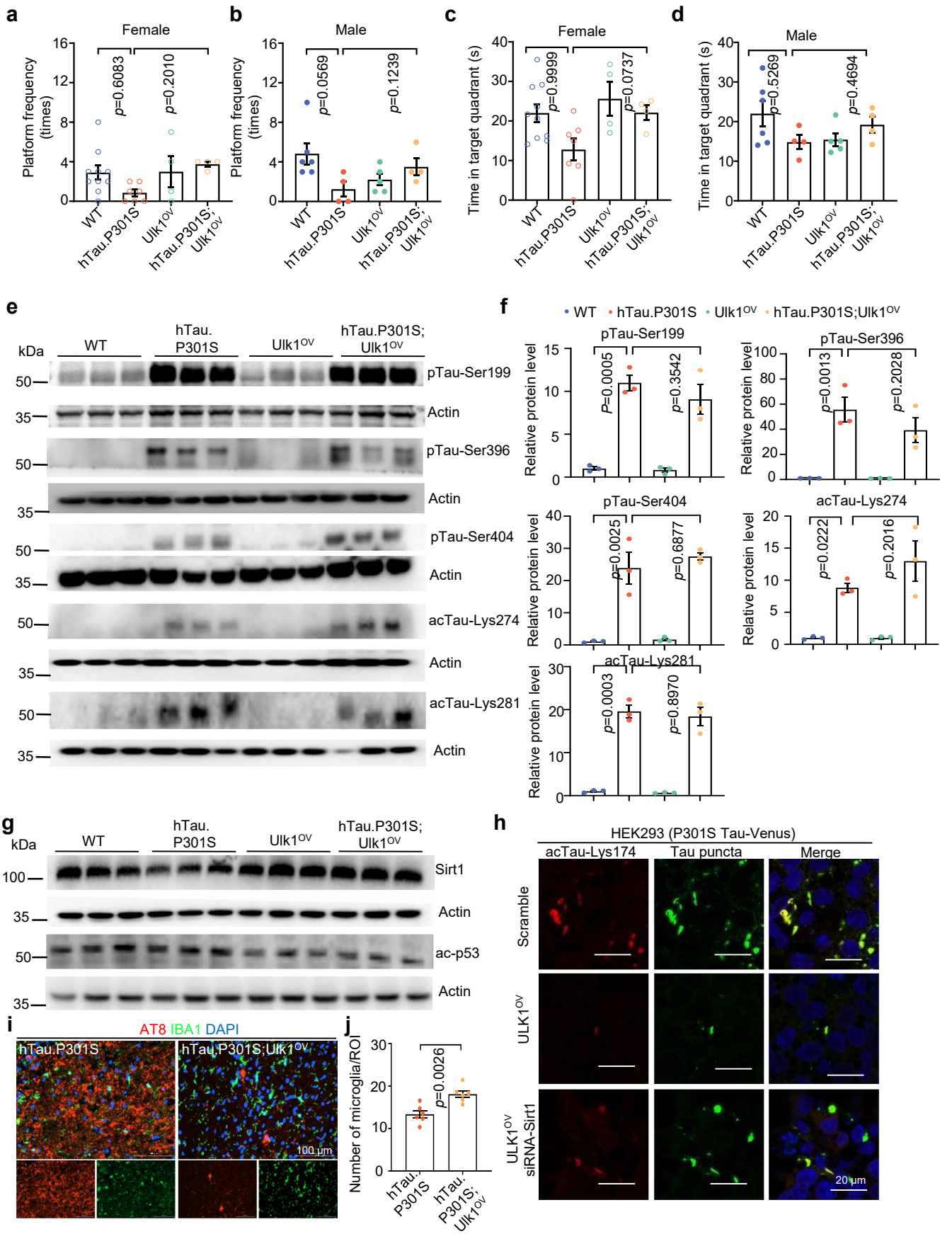

Extended Data Fig. 9 | See next page for caption.

https://doi.org/10.1038/s43587-026-01108-z

Extended Data Fig. 9 | Effect of ULK1 overexpression on learning and memory deficits and tauopathy in hTau.P301S mice. (**a, b**) Number of platform location crossings for female (**a**) and male (**b**) mice of different genotypes in the MWM test trial. Data were shown as mean ± S.E.M. (Female mice: n = 10, 7,4 and 4 mice for WT, hTau.P301S, $Ulk1^{OV}$ and hTau.P301S;$Ulk1^{OV}$, respectively. Male mice: n = 6, 4, 5 and 4 mice for WT, hTau.P301S, $Ulk1^{OV}$ and hTau.P301S;$Ulk1^{OV}$, respectively). (**c, d**) Time spent in the target quadrant for female (**c**) and male mice (**d**) from different genotypes in the MWM. Data are shown as mean ± S.E.M. (Female mice: n = 10, 7,4 and 4 mice for WT, hTau.P301S, $Ulk1^{OV}$ and hTau.P301S;$Ulk1^{OV}$, respectively. Male mice: n = 6, 4, 5 and 4 mice for WT, hTau.P301S, $Ulk1^{OV}$ and hTau.P301S;$Ulk1^{OV}$, respectively). (**e, f**) The levels of p-Tau and ac-Tau were measured by Western blot of hippocampal tissues of WT, hTau.P301S, $Ulk1^{OV}$ and hTau.P301S;$Ulk1^{OV}$ mice. A set of representative blots (**e**) accomplished with quantifications (**f**) are shown. n = 3 mice/group. (**g**) Western blot data showing the expression of Sirt1 and ac-p53 in hippocampal tissues from designated mouse groups. (n = 3 mice/group). (**h**) Representative images with immunofluorescent staining of acTau-Lys174 (red) and aggregated Tau puncta (green) in HEK293 Tau-Venus cells. (**I, j**) Representative images with immunofluorescent staining of AT8 (p-Tau Ser202 and Thr205) and IBA1(microglia) in hippocampi of hTau.P301S and hTau.P301S;$Ulk1^{OV}$ mice with quantification of the numbers of microglia presented (n = 6 mice/group). Unless specified elsewhere, data are mean ± S.E.M. Statistical significance was determined using two-way ANOVA followed by Dunnett's multiple comparisons (**a**-**d**, **f**); two-sided unpaired two-tailed Student's t-test (**g**).

https://doi.org/10.1038/s43587-026-01108-z

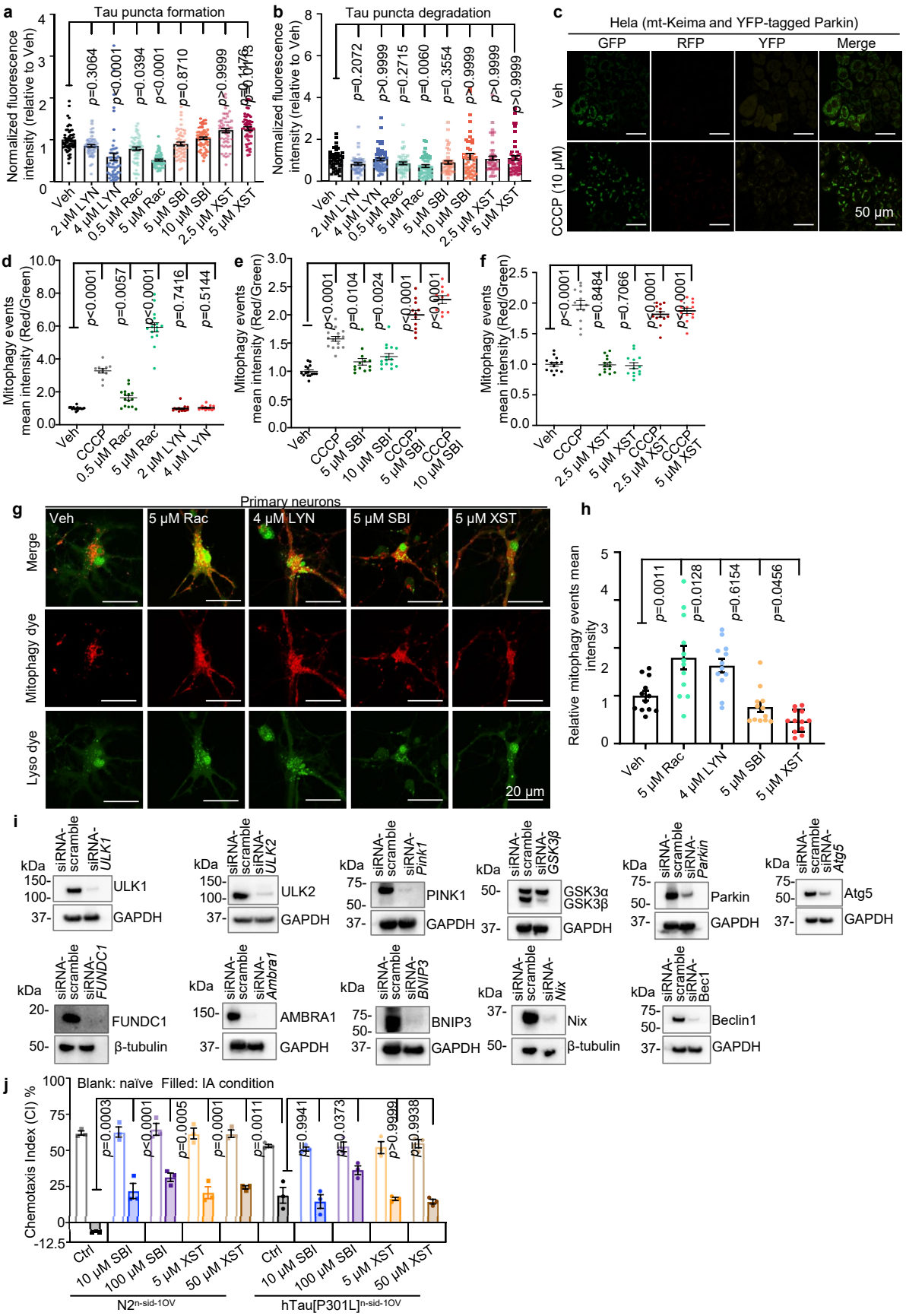

Extended Data Fig. 10 | See next page for caption.

https://doi.org/10.1038/s43587-026-01108-z

Extended Data Fig. 10 | Effect of pharmacologic activation of ULK1 on Tau pathology and memory deficit. (**a**) Effects of ULK1 activators (2, 4 μM of LYN-1604 dihydrochloride; 0.5, 5 μM of (Rac)-BL-918) and inhibitors (5, 10 μM of SBI-0206965; 2.5, 5 μM of XST-14) on Tau seed-induced formation of Tau puncta in HEK293 cells expressing 0N4R P301S Tau-Venus. Data are pooled from 3 biological replicates. **(b)** Effects of ULK1 activators (2, 4 μM of LYN-1604 dihydrochloride; 0.5, 5 μM of (Rac)-BL-918) and inhibitors (5, 10 μM of SBI-0206965; 2.5, 5 μM of XST-14) on degradation of preformed Tau puncta in the HEK293 cells expression 0N4R P301S Tau-Venus. Data are pooled from 3 biological replicates. (**c**) mt-Keima and YPH-Parkin expressing HeLa cells were used to evaluate the effects on mitophagy induction by treating a positive control CCCP. Representative images are shown. (**d-f**) Quantification of mitophagy events by treating ULK1 activators, Rac-BL-918 (0.5, 5 μM) and LYN-1604 (2, 4 μM), as well as ULK1 inhibitors SBI-0206965 (5, 10 μM) and XST-14 (2.5, 5 μM). One dot represents the average value of one image. Data were pooled from 3 biological replicates. (**g-h**) Representative images (**g**) and quantification (**h**) of mitophagy induction from primary cortical neurons by treating ULK1 activators, Rac-BL-918 (5 μM) and LYN-1604 (4 μM), as well as ULK1 inhibitors SBI-0206965 (5 μM) and XST-14 (5 μM). Mitophagy was detected using a mitophagy detection dye kit. Nuclei were stained with DAPI. Scale bar = 20 μm. (**i**) Representative blots of target proteins (ULK1, ULK2, PINK1, GSK3β, Parkin, Atg5, FUNDC1, AMBRA1, BNIP3, Nix, Beclin1) and loading control (GAPDH or β-tubulin) in HEK293 cells expressing 0N4R P301S Tau-Venus transfected with siRNAs (100 nM, 48 h) or scrambled siRNA. (**j**) Associative memory tests were administered to adult day 2 transgenic *C. elegans* expressing hTau[P301L]n-sid-1^{OV} in the presence of ULK1 inhibitors (10, 100 μM of SBI-0206965; 5, 50 μM of XST-14). Attraction to odorant is quantified as Chemotaxis Index (% CI), where lower score corresponds to greater response to odorant/better memory function. Unless specified elsewhere, data are mean ± S.E.M. Statistical analyses performed were one-way ANOVA followed by Dunnett's multiple comparisons test (**a**, **b**, **d-f**, **h**); two-way ANOVA followed by Tukey's multiple-comparisons test (**j**).

nature portfolio

Corresponding author(s): Guobing Chen
Evandro Fei Fang

Last updated by author(s): Mar 04, 2026

Reporting Summary

Nature Portfolio wishes to improve the reproducibility of the work that we publish. This form provides structure for consistency and transparency in reporting. For further information on Nature Portfolio policies, see our Editorial Policies and the Editorial Policy Checklist.

Statistics

For all statistical analyses, confirm that the following items are present in the figure legend, table legend, main text, or Methods section.

n/a	Confirmed
☐	☒ The exact sample size (*n*) for each experimental group/condition, given as a discrete number and unit of measurement
☐	☒ A statement on whether measurements were taken from distinct samples or whether the same sample was measured repeatedly
☐	☒ The statistical test(s) used AND whether they are one- or two-sided *Only common tests should be described solely by name; describe more complex techniques in the Methods section.*
☒	☐ A description of all covariates tested
☐	☒ A description of any assumptions or corrections, such as tests of normality and adjustment for multiple comparisons
☐	☒ A full description of the statistical parameters including central tendency (e.g. means) or other basic estimates (e.g. regression coefficient) AND variation (e.g. standard deviation) or associated estimates of uncertainty (e.g. confidence intervals)
☐	☒ For null hypothesis testing, the test statistic (e.g. *F*, *t*, *r*) with confidence intervals, effect sizes, degrees of freedom and *P* value noted *Give P values as exact values whenever suitable.*
☒	☐ For Bayesian analysis, information on the choice of priors and Markov chain Monte Carlo settings
☒	☐ For hierarchical and complex designs, identification of the appropriate level for tests and full reporting of outcomes
☒	☐ Estimates of effect sizes (e.g. Cohen's *d*, Pearson's *r*), indicating how they were calculated

Our web collection on statistics for biologists contains articles on many of the points above.

Software and code

Policy information about availability of computer code

Data collection	All Western blots were digitized, and protein intensities were quantified using ImageJ software (Version 1.8.0). Immunofluorescent and immunohistochemical images captured by the Zeiss LSM 780 confocal microscope were digitized and analyzed using ZEISS ZEN 3.6 (Blue edition) software or ImageJ software (Version 1.8.0). The Noldus EthoVision XT 3.0 video-tracking system and CleverSys Scan (CleverSys) system were used to record mouse activity in multiple behavioral tests, including NOR/NOL, Morris water maze, and Y-maze. Metabolic rates were evaluated using indirect calorimetry in open-circuit Oxymax chambers with CLAMS (Columbus Instruments), as described previously.
Data analysis	Behavioral tracking software was Noldus. Behavioral data were formatted in Microsoft Excel.Data were analyzed with GraphPad Prism version 9 and SPSS version 28.R package Seurat (v4.0.4), immunarch (v0.6.6), DESeq2 (v1.32.0), topGO (v2.44.0), pheatmap (v1.0.12) was used in RNA -seq data.Baseline statistical analyses were performed using IBM SPSS version 26 (IBM, Armonk, NY, USA). In the descriptive analyses, parametric tests were used. The Pearson's $\chi 2$ was applied for the categorical variables. Student's t-test was used for the continuous variables, except for the Mann-Whitney U analysis used for serum ULK1 as it was highly skewed. Spearman's rho was used for bivariate correlation analyses. The CSF core biomarkers were analysed in two different laboratories preventing us from using them as continuous variables in the analyses including both patients and CU controls. Progression analyses were performed using Stata/IC 17.0 (StataCorp LLC, College Station, USA). We applied a linear mixed-effects regression model to test the interaction of CSF ULK1 x time on CDR-SB scores. The dependent variable was thus CDR-SB. The fixed effects included CSF ULK1 x time + CSF Aβ1-42 x time + CSF p-Tau181 x time + CSF ULK1 + CSF Aβ1-42 + CSF p-Tau181 + clinical syndrome (MCI, or dementia) + age + sex + years of education. Random effects included time and intercept. The variable time was defined as the follow-up duration of the CDR-scorings in years. The interaction of CSF Aβ1-42 and p-Tau181 with time (CSF Aβ1-42 x time and CSF p-Tau181 x time) were included in addition to the simple main effects of these variable since we were interested in whether higher concentrations of CSF ULK1 relative to AD pathology is favourable. We further calculated plots of predictive margins using margins and marginsplot. For other data, GraphPad Prism 9 software was used for statistical analysis of experimental data and results are presented as mean ± S.E.M. unless otherwise specified. We performed a minimum of 3 independent biological trials for each wet-lab experiment. The

details of biological replicates are in the figure legends. Values of $p < 0.05$ were considered significant. All sample populations were first assessed for normality. Two-tailed unpaired Student's t-tests were used for comparisons bet.

For manuscripts utilizing custom algorithms or software that are central to the research but not yet described in published literature, software must be made available to editors and reviewers. We strongly encourage code deposition in a community repository (e.g. GitHub). See the Nature Portfolio guidelines for submitting code & software for further information.

Data

Policy information about availability of data

All manuscripts must include a data availability statement. This statement should provide the following information, where applicable:

- Accession codes, unique identifiers, or web links for publicly available datasets
- A description of any restrictions on data availability
- For clinical datasets or third party data, please ensure that the statement adheres to our policy

The single-nucleus RNA-Sequencing data is available at Synapse (https://www.synapse.org/#!Synapse:syn18485175). The sequencing data reported in this paper were deposited in the Gene Expression Omnibus with accessions numbers GSE263411.

Research involving human participants, their data, or biological material

Policy information about studies with human participants or human data. See also policy information about sex, gender (identity/presentation), and sexual orientation and race, ethnicity and racism.

Reporting on sex and gender	For the CSF, blood and postmortem human brain tissue used in this study, an equal mixture of self-reported sexes was included in this study.
Reporting on race, ethnicity, or other socially relevant groupings	Race, ethnicity, or other socially relevant groupings are not reported for the CSF, blood and postmortem human brain tissue in this study.
Population characteristics	Postmortem human brain tissue from males and females aged 61-103 years old at the time of death that were cognitively normal or clinically diagnosed with Alzheimer's disease were used in this study. The CSF and blood characteristics see table 1.
Recruitment	Subjects were not recruited specifically for this study. Postmortem human brain are derived from the tissue repository of London Neurodegenerative Diseases Brain Bank.The CSF and blood are derived from the repository of CogNorm.Unimpaired (CU) controls were recruited when referred to hospital for elective surgery for gynecological, orthopedic, or urological problems. These patients were assessed with the same cognitive tests as the memory clinic patients, and the majority were followed yearly up to five years. CSF was collected in conjunction with spinal anaesthesia at the surgery.
Ethics oversight	The human study was performed according to the principles of the Helsinki declaration and King's College London. All participants gave their written informed consent prior to participating in the study. The REC reference for CogNorm is 2011/2052. Refer to the section in methods where we explain the details. Copy paste from the manuscript "The regional Ethics Committee for medical research in the South-East of Norway (REK 2011/2052 and REK 2017/371) and the Data Protector Officer at our institution approved the study."

Note that full information on the approval of the study protocol must also be provided in the manuscript.

Field-specific reporting

Please select the one below that is the best fit for your research. If you are not sure, read the appropriate sections before making your selection.

☒ Life sciences ☐ Behavioural & social sciences ☐ Ecological, evolutionary & environmental sciences

For a reference copy of the document with all sections, see nature.com/documents/nr-reporting-summary-flat.pdf

Life sciences study design

All studies must disclose on these points even when the disclosure is negative.

Sample size	No explicit calculations were performed to determine sample size. Rather, The number of animals proposed per group was informed by power analyses performed on previously-collected data to generate group sizes that will ensure minimally sufficient statistical power (0.9) to detect statistically significant differences between groups (0.05), using mixed ANOVA and appropriate post-hoc tests adjusted for multiple comparisons.
Data exclusions	No data were excluded from the analyses.
Replication	Most experiments were repeated 3 times or more than 3 times independently with reproducible results, see figure legends for details of each experiment. All attempts at replication were successful.
Randomization	The participants were allocated into different experimental groups according to their age.

Blinding	To eliminate subjectivity, we have specified that both the investigators administering the treatment and those assessing the outcomes were blinded to the group allocation.

Reporting for specific materials, systems and methods

We require information from authors about some types of materials, experimental systems and methods used in many studies. Here, indicate whether each material, system or method listed is relevant to your study. If you are not sure if a list item applies to your research, read the appropriate section before selecting a response.

Materials & experimental systems

n/a	Involved in the study
☐	☒ Antibodies
☐	☒ Eukaryotic cell lines
☒	☐ Palaeontology and archaeology
☐	☒ Animals and other organisms
☒	☐ Clinical data
☒	☐ Dual use research of concern
☒	☐ Plants

Methods

n/a	Involved in the study
☒	☐ ChIP-seq
☒	☐ Flow cytometry
☒	☐ MRI-based neuroimaging

Antibodies

Antibodies used	Rabbit polyclonal anti-ULK1 antibody (1:1000, Sigma, Cat# A7481); Rabbit monoclonal anti-ULK1 antibody (1:1000, Cell Signaling Technology, Cat#6439); Rabbit monoclonal anti-TAU antibody (1:1000, Abcam, Cat#ab254256); Rabit monoclonal anti-LC3B antibody (1:1000, Cell Signaling Technology, Cat#43566); Mouse monoclonal anti-β-Amyloid antibody (1:500, Biolegend, Cat#803008); Rabit monoclonal anti-APP antibody (1:1000, Cell Signaling Technology, Cat#2452S); Rabit polyclonal anti-APP-CTFs antibody (1:500, Invitrogen, Cat#CT695); Rabit monoclonal anti-ambra1 antibody (1:1000, Cell Signaling Technology, Cat#24907); Rabit monoclonal anti-Pink1 antibody (1:1000, Cell Signaling Technology, Cat#6946T); Rabit monoclonal anti-Parkin antibody (1:1000, Cell Signaling Technology, Cat#4211S); Rabit monoclonal anti-Beclin antibody (1:1000, Cell Signaling Technology, Cat#3495); Rabit monoclonal anti-NIX antibody (1:1000, Cell Signaling Technology, Cat#12396S); Mouse monoclonal anti-SirT1 antibody (1:500, Cell Signaling Technology, Cat#8469); Rabit monoclonal anti-Cathepsin B antibody (1:500, Invitrogen, Cat#MAB30458); Rabit polyclonal phospho-Tau (Thr231) Antibody (1:1000, Cell Signaling Technology, Cat#71429); Rabit polyclonal phospho-Tau (Thr181) Antibody (1:1000, Cell Signaling Technology, Cat#12885S); Rabit polyclonal phospho-Tau (Thr217) antibody (1:1000, Invitrogen, Cat.# 44-744); Rabit monoclonal phospho-Tau (Ser396) Antibody (1:1000, Invitrogen, Cat.#MA5-41154); Rabit polyclonal phospho-Tau (Ser404) Antibody (1:1000, Cell Signaling Technology, Cat#70194S); Rabit polyclonal phospho-Tau (Ser199) Antibody (1:1000, Cell Signaling Technology, Cat#29957); Rabit monoclonal anti- Tau antibody (1:1000, Cell Signaling Technology, Cat#46687s); Mouse monoclonal anti-ac-tauK174 (1:250,Gan lab, Cornell, USA); Rabit monoclonal anti-ac-tauK274 (1:500, Gan lab, Cornell, USA); Rabit monoclonal anti-ac-tauK281 (1:500, Gan lab, Cornell, USA); Rabit monoclonal anti-actin antibody (1:2000, Cell Signaling Technology, Cat#3700); Rabit monoclonal anti-GSK3 antibody (1:1000, Cell Signaling Technology, Cat#5676); Rabit monoclonal anti-Atg5 antibody (1:1000, Cell Signaling Technology, Cat#12994); Rabit polyclonal anti-ULK2 Antibody (1:1000, abcam, Cat#ab97695); Rabit monoclonal anti-Fundc1 antibody (1:1000, Cell Signaling Technology, Cat#49240); Rabit monoclonal anti-BNIP3 antibody (1:1000, Cell Signaling Technology, Cat#44060S); Rabit monoclonal anti-gapdh antibody (1:1000, Cell Signaling Technology, Cat#5174); Rabit monoclonal anti-p-mTOR antibody (1:1000, Cell Signaling Technology, Cat#2971s); Rabit monoclonal anti-mTOR antibody (1:1000, abcam, Cat#ab109268); Rabit monoclonal anti-p-AMPK antibody (1:1000, Cell Signaling Technology, Cat#2535s); Rabit monoclonal anti-AMPK antibody (1:1000, Cell Signaling, Technology, Cat#5831s); Mouse monoclonal anti-COX2 antibody (1:500, Santa cruz, Cat4#sc-514489); Rabit polyclonal anti-ULK1 antibody (1:500, Sigma, Cat# A7481); Mouse monoclonal anti-Map2 (1.100, Sigma, Cat#MAB3418); Rabbit monoclonal anti-TAU antibody (1:200, Abcam, Cat#ab254256); Mouse monoclonal anti-β-Amyloid antibody (1:250, Biolegend, Cat#803008); Rabit polyclonal anti-IBA1 antibody (1:500, FUJIFILM Wako Pure, Cat#019-19741); Mouse monoclonal anti-COX2 antibody (1:250, Santa cruz, Cat4#sc-514489); Rabit monoclonal anti-Cathepsin B antibody (1:200, Invitrogen, Cat#MAB30458); Mouse monoclonal anti-AT8 antibody (1:500, Invitrogen, Cat#MN1020B); ac-Tau174 (1:250, Gan lab, Cornell N/A); Rabbit monoclonal anti-NeuN antibody (1:500, Abcam, Cat#ab177487); Rabbit polyclonal anti-GFAP antibody (1:500, abcam, Cat#ab116010). Secondary antibodies including anti-mouse immunoglobulin G (1:10000, Cell Signaling Technology, Cat#7060); anti-rabbit IgG (1:10000, Invitrogen, Cat#31460); Donkey Anti-Rabbit IgG H&L (Alexa Fluor® 488) (1:1000, Abcam, Cat#ab150073); Donkey Anti-Rabbit IgG H&L (Alexa Fluor® 594) (1:1000, Abcam, Cat#ab150076); Donkey Anti-Mouse IgG H&L (Alexa Fluor® 488) (1:1000, Abcam, Cat#ab150105); Donkey Anti-Mouse IgG H&L (Alexa Fluor® 594) (1:1000, Abcam, Cat#ab150108) Goat Anti-Mouse IgG H&L (Alexa Fluor® 488) (1:1000, Invitrogen, Cat#a-11001); Goat Anti-Rabbit IgG H&L (Alexa Fluor® 546) (1:1000, Invitrogen, Cat#A10040).
Validation	All the antibodies were obtained from commercial sources and the lots were validated on the manufacturer websites. Validated lots and corresponding applications in the published literature can be found on the company website.

Eukaryotic cell lines

Policy information about cell lines and Sex and Gender in Research

Cell line source(s)	HeLa cells expressing YFP-tagged Parkin and mtKeima (YPH-mtKeima) were a generous gift from Prof. Han-Ming Shen, National University of Singapore. HEK293 cells stably expressing P301S Tau-Venus were obtained from William A McEwan.

Authentication	According to the donor laboratory, the parental HeLa cell line was authenticated by short tandem repeat (STR) profiling, and the stable expression of YFP-Parkin and mtKeima was verified by fluorescence microscopy and Western blot analysis. We confirmed the expression of both fluorescent markers upon receipt of the cells. The expression of P301S Tau-Venus was confirmed by fluorescence microscopy.
Mycoplasma contamination	All cell lines tested negative for mycoplasma.
Commonly misidentified lines (See ICLAC register)	No cross-contaminated or misidentified cell lines were identified.

Animals and other research organisms

Policy information about studies involving animals; ARRIVE guidelines recommended for reporting animal research, and Sex and Gender in Research

Laboratory animals	All animal procedures were approved by the Jinan University Institutional Animal Care and Use Committee. All animals were maintained at the Jinan University Institutional Animal Care Facility under standard conditions. Breeding pairs of Ulk1OV mice (C57BL/6–Tg(CAG-Ulk1)1Cyagen) were generated by Cyagen Biosciences Inc. Transgenic (Tg) mice (C57BL6 background) expressing Ulk1 in Cre-loxP dependent manner, under the control of CAG promoter were generated utilizing a custom plasmid vector generated by Cyagen. 5xFAD mice, hTau.P301S mice, ULK1OV mice, C57BL/6J mice.
Wild animals	No wild animals were used in this study.
Reporting on sex	Both sexes were used in these studies. Sex information is provided in figure legends.
Field-collected samples	Field-collected samples were not included in this study.
Ethics oversight	All animals were maintained at the Jinan University Institutional Animal Care Facility (Guangdong, China) under standard conditions. All animal procedures were approved by the Jinan University Institutional Animal Care and Use Committee (IACUC-20181029-01).

Note that full information on the approval of the study protocol must also be provided in the manuscript.

Plants

Seed stocks	n/a
Novel plant genotypes	n/a
Authentication	n/a